Energetic Particle Precipitation in the Atmosphere: Northern Hemisphere Variability and Transport

by

Laura A. Holt

B.A., St. Cloud State University, 2005

B.S., St. Cloud State University, 2005

A thesis submitted to the

Faculty of the Graduate School of the

University of Colorado in partial fulfillment

of the requirements for the degree of

Doctor of Philosophy

Department of Atmospheric and Oceanic Science

2013

This thesis entitled:
Energetic Particle Precipitation in the Atmosphere: Northern Hemisphere Variability and Transport
written by Laura A. Holt
has been approved for the Department of Atmospheric and Oceanic Science

_____
Cora Randall

_____
V. Lynn Harvey

Date _____

The final copy of this thesis has been examined by the signatories, and we find that both the content and the form meet acceptable presentation standards of scholarly work in the above mentioned discipline.

Holt, Laura A. (Ph.D., Atmospheric & Oceanic Sciences)

Energetic Particle Precipitation in the Atmosphere:
Northern Hemisphere Variability and Transport

Thesis directed by Prof. Cora Randall

Abstract. It is well understood that chemical processes in the stratosphere lead to the destruction of ozone (O_3). Our interest in these processes is twofold: (1) stratospheric O_3 shields the Earth from biologically harmful radiation, and (2) O_3 is a radiatively active gas largely responsible for the temperature structure of the middle atmosphere. A subset of chemical processes that is particularly relevant to O_3 consists of catalytic cycles. Catalysts destroy O_3 without being depleted. The NO_x ($NO + NO_2$) catalytic cycle dominates in the middle stratosphere. One source of stratospheric NO_x is energetic particle precipitation (EPP), which contributes to the stratospheric odd nitrogen (NO_y) budget in the polar winter. Through interaction with O_3, NO_x created by EPP (EPP-NO_x) has the potential to affect not only the composition of the middle atmosphere but, since O_3 is a radiatively active gas, temperature and dynamics as well. This leads to the following science questions, which are the questions that motivated my dissertation:

(1) How much EPP-NO_x is transported to the stratosphere from year to year?

(2) What are the important transport processes involved?

The research described here focuses on answering the first question through quantification of the amount of EPP-NO_x reaching the northern hemisphere stratosphere using satellite data and the second question through state-of-the-art climate simulations designed to elucidate the important transport mechanisms.

To Jonathan for loving me

To my parents for nurturing me

And to my grandparents for inspiring me

Acknowledgements

Certainly this thesis was only possible because of the dedication and guidance of my advisor, Cora Randall, an exemplary scientist and inspiring person. Thank you for your encouragement and patience and for sharing your time, ideas, and wisdom with me. To Lynn Harvey, I appreciate your advice, honesty, and sense of humor; you have been like a big sister to me. Thanks to Ethan Peck for providing WACCM data. Thanks to Bernd Funke and Gabriele Stiller for providing MIPAS data and valuable feedback. I thank NCAR for having me as a visitor, and I thank the WACCM group for help with the model and letting me tag along to lunch. In particular, I am grateful to Anne Smith for being a fantastic mentor and for being very generous with time and insights. I thank Dan Marsh for sharing ideas and providing an algorithm for detecting sudden stratospheric warmings. I am indebted to Chuck Bardeen for thoughtful feedback on this thesis. Thank you to Rolando Garcia, Mike Mills, Dan Marsh, and Doug Kinnison for many delightful espresso breaks that almost always resulted in learning something new and interesting. And to Matthias Brakebusch and Susanne Benze, my companions through this adventure, thank you for many coffee breaks, helping me with German, sharing ideas, and just being there. Bis zum nächsten Mal!

Finally, I gratefully acknowledge the support provided by the NSF CEDAR program, grant AGS 0940124, and by the NASA Living With a Star program, grants NNX10AQ54G and NNXO6AC05G. I thank the National Geophysical Data Center for the A_p index and the Space Environment Center for SPE data.

Contents

Chapter

Tables

Table

Figures

Figure

Chapter 1

Energetic Particle Precipitation in the Atmosphere

1.1 Introduction

Energetic particle precipitation (EPP) refers to energetic protons, electrons, neutrons, or ions that are accelerated into the Earth's atmosphere through various heliophysical processes. The energetic particles collide with atmospheric constituents, resulting in the ionization, dissociation, and excitation of atoms and molecules. The beautiful dancing lights known as the aurorae are examples of the effects of EPP on the atmosphere. A more specific consequence of EPP, at the heart of this scientific investigation, is the formation of NO_x ($NO + NO_2$), the main catalytic destroyer of ozone (O_3) between ~25 and 45 km. The source, energy, momentum, and flux of the incoming particles dictate where and how much NO_x is produced by EPP (referred to as EPP-NO_x). Through energy deposition and impact on radiatively active gases, EPP can also theoretically influence temperatures, winds, and perhaps even climate.

The fundamental process of interest here is the Indirect Effect of EPP (EPP IE). The EPP IE refers to the production of NO_x by EPP in the mesosphere and lower thermosphere (MLT), followed by transport of the EPP-NO_x to the stratosphere where it interferes with O_3 catalytic cycles. EPP-NO_x created in the MLT can only be transported to the stratosphere in the polar night since it is photochemically destroyed in a matter of days in the sunlit mesosphere. While we know that the EPP IE depends on both EPP input and transport variables, the full vertical distribution of EPP-NO_x and the exact mechanisms controlling

the transport remain uncertain. Therefore, a full understanding of the EPP IE requires knowledge of the variability in EPP input and the polar winter dynamics controlling the transport from the MLT to the stratosphere.

This thesis presents four main results. The first answers a long-standing puzzle: why was there a gap in direct observations of the EPP IE between when it was first observed in the NH winter of 1978–1979 and 1991? The second result is the quantification of the variability in the EPP IE in the northern hemisphere (NH) in the current satellite record. The first two results are the subject of Chapter 2. The third result, presented in Chapter 3, shows the sensitivity of the EPP IE to the gravity wave (GW) parameterization in the Whole Atmosphere Community Climate Model (WACCM). And the fourth result, presented in Chapter 4, quantifies the effect of major sudden stratospheric warming (SSW) and elevated stratopause (ES) events on the EPP IE using WACCM.

1.2 Historical Background

Chapman [1930] put forth the first theory to explain the balance of O_3 in the stratosphere. His theory proposed that the production of O_3 through photodissociation of molecular oxygen was balanced through loss by photochemical destruction and reaction with atomic oxygen, and it was generally accepted for the subsequent three decades. Starting in the early 1960s, it became increasingly apparent that these reactions alone were not sufficient to explain newly observed values of O_3 in the stratosphere [e.g., *Crutzen*, 1969; *Hunt*, 1966]. Catalytic cycles, which destroy O_3 without depleting the catalyst, were investigated as candidates for the missing reactions in the stratosphere:

$$\mathrm{XO} + \mathrm{O} \rightarrow \mathrm{X} + \mathrm{O_2} \tag{1.1a}$$

$$\underline{\mathrm{X} + \mathrm{O_3} \rightarrow \mathrm{XO} + \mathrm{O_2}} \tag{1.1b}$$

$$\textbf{Net: } \boxed{\mathrm{O} + \mathrm{O_3} \rightarrow 2\mathrm{O_2}}$$

where X represents the catalyst. The first proposed catalytic cycle involved hydrogen radicals

(X = OH) [*Hampson*, 1965]. However, the HO_x ($OH + HO_2$) catalytic cycle could not explain the O_3 distribution from 30 to 35 km [*Crutzen*, 1969]. *Crutzen* [1970] suggested that the NO_x catalytic cycle might play an important role in stratospheric O_3 chemistry:

$$NO + O_3 \rightarrow NO_2 + O_2$$

$$NO_2 + O \rightarrow NO + O_2.$$

Further interest in the role of the NO_x catalytic cycle in the stratosphere was bolstered by concern over supersonic jet exhaust containing NO_x [*Crutzen*, 1971, 1972; *Johnston*, 1971]. It was subsequently established that the key catalytic cycle responsible for O_3 loss in the stratosphere between ∼25 and 45 km is the NO_x catalytic cycle [e.g., *Crutzen*, 1979; *Johnston*, 1972; *McElroy et al.*, 1974; *Nicolet*, 1972; *Wofsy and McElroy*, 1974].

As the importance of the role of the NO_x catalytic cycle in the stratosphere became accepted, an enormous effort began to classify stratospheric sources of NO_x and quantify the magnitude of each source. *Johnston et al.* [1973] considered the addition of NO to the stratosphere as a result of nuclear bomb detonations. Other studies looked at NO produced from the oxidation of N_2O created in the troposphere and transported to the stratosphere [*Bates and Hays*, 1967; *Crutzen*, 1974; *McElroy and McConnell*, 1971; *McElroy et al.*, 1976; *Nicolet*, 1971]:

$$N_2O + O(^1D) \rightarrow 2NO \tag{1.2}$$

Tropospheric N_2O has manmade sources, such as combustion and fertilizer use, and natural sources, such as microbial processes in the soil and lightning. Interest in EPP as another source of stratospheric NO_x was motivated by a rocket study that measured O_3 from 51 to 80 km at the beginning of a solar proton event (SPE) and again two days later [*Weeks et al.*, 1972]. O_3 was significantly less during the initial phase of the SPE compared to quieter conditions two days later. *Crutzen et al.* [1975] showed that SPEs can produce NO_x in the stratosphere directly, and subsequent studies confirmed the impact of SPEs on stratospheric NO_x and O_3 [e.g., *Bauer*, 1979; *Frederick*, 1976; *Heath et al.*, 1977; *Reagan et al.*, 1981; *Rusch*

et al., 1981; *Solomon and Crutzen*, 1981]. Galactic cosmic rays (GCRs) were also shown to contribute to the stratospheric NO_x budget [*Nicolet*, 1975; *Warneck*, 1972]. By the end of the 1970s, a great deal had been discovered about the various sources of stratospheric NO_x. *Crutzen* [1979] reviewed the then-current knowledge about stratospheric NO_x sources: $\sim 85\%$ from N_2O oxidation, $\sim 10\%$ from SPEs, $\sim 3\%$ from GCRs, and $\sim 2\%$ from nuclear bombs.

Still, little was known about another potential EPP-related source of stratospheric NO_x: the EPP IE. It was already known that NO is produced at higher altitudes ($\sim$100 km) by auroral particle precipitation and extreme ultra violet radiation [e.g., *Gylvan Meira*, 1971; *Narcisi et al.*, 1972; *Gérard and Barth*, 1977], and it was hypothesized that some of this NO could be transported to the stratosphere [*Nicolet*, 1970]. However, *Strobel et al.* [1970] and *Strobel* [1971] predicted, using a one-dimensional (1-D) model, that the contribution of upper atmospheric NO_x to the stratosphere was insignificant compared to the other sources discussed above. In his review, *Crutzen* [1979] pointed out that 1-D models may not be sufficient to study the transport of NO_x produced in the MLT to the stratosphere because they did not include latitudinal variation or meridional transport, and NO_x has the highest probability of being transported to the stratosphere during polar night. And, in fact, when *Frederick and Orsini* [1982] incorporated latitudinal and seasonal variations into a 1-D model, they obtained pronounced differences between the winter and summer poles, and the model showed transport of NO_x from the MLT to the stratosphere in the winter. When the problem was revisited using two-dimensional (2-D) models, the models predicted that significant amounts of NO_x could be transported by the residual circulation to the stratosphere in the polar night [*Solomon et al.*, 1982; *Solomon and Garcia*, 1983]. A short time later, *Russell et al.* [1984] showed the first experimental evidence of NO_x descending to the stratosphere from the Limb Infrared Monitor of the Stratosphere (LIMS), which measured NO_2 during the NH winter of 1978–1979.

In the intervening decades, we have learned a great deal about the NO_x that is produced

by EPP in the MLT and is subsequently transported to the stratosphere during the polar winter. Several satellite instruments have captured the signature of what we now call the EPP IE, along with evidence for the destruction of O_3 by EPP-NO_x [e.g., *Callis et al.*, 1998a; *Callis and Lambeth*, 1998; *Funke et al.*, 2005a; *López-Puertas et al.*, 2005a; *Orsolini et al.*, 2005; *Randall et al.*, 1998, 2001, 2005, 2006, 2007, 2009; *Rinsland et al.*, 1996, 1999, 2005; *Seppälä et al.*, 2007a; *Siskind and Russell*, 1996; *Siskind et al.*, 2000; *Stiller et al.*, 2005]. Current estimates put the maximum yearly contribution of the EPP IE at ∼10% of the stratospheric odd nitrogen resulting from reaction (1.2) in each hemisphere [*Funke et al.*, 2005a; *Holt et al.*, 2012; *Randall et al.*, 2007]; however, studies have also shown a high level of year-to-year variability in both hemispheres as well as pronounced differences between the two hemispheres. The mechanisms controlling the interannual and interhemispheric variability in the EPP IE are the topic of current research, and understanding these mechanisms has provided the motivation for my dissertation.

While the initial fervor over stratospheric NO_x was motivated by the somewhat far-fetched idea that supersonic jets might literally destroy all of the O_3 [*Norton and Shuckburgh*, 2000], fears that have since abated, there are still compelling reasons to study the EPP IE. The middle atmosphere is not a static and separate region of the atmosphere that has little impact on the world below, as once thought, but a dynamic region full of both turbulence and dramatic large-scale motions that couples the troposphere to the upper atmosphere, ionosphere, magnetosphere and ultimately the sun. Evidence suggests that changes in O_3 affect temperatures and circulation [*Gabriel et al.*, 2007], and temperature changes in the middle atmosphere can influence tropospheric weather and climate [*Baldwin et al.*, 2007; *Haynes*, 2005]. Furthermore, it is uncertain how various nonlinear feedbacks associated with the EPP IE might change as the climate changes.

Even though we have made much progress toward understanding the EPP IE in the thirty years since it was first predicted by *Solomon et al.* [1982], we are still far from a complete understanding of the mechanisms controlling it. In fact, the most challenging aspects

of studying the EPP IE initially remain so today. *Solomon et al.* [1982] commented that the largest uncertainties in our assessment of the effects of EPP on the middle atmosphere lie in the transport processes and in the branching ratio of ground and excited state nitrogen in the lower thermosphere. In a recent review of EPP effects on the atmosphere, *Sinnhuber et al.* [2012] conclude that these remain the two most significant uncertainties.

1.3 Energetic Particle Precipitation

Most energetic particles that enter the Earth's atmosphere ultimately originate from the Sun. Galactic cosmic rays are an example of energetic particles that originate outside of the solar system. The Sun is a constant source of energetic particles that stream out from the corona and fill interplanetary space. This constant stream of particles is known as the solar wind. Several particle populations associated with various space weather phenomena can impact the atmosphere. Space weather refers to events in near-Earth space, such as coronal mass ejections (CMEs), solar flares, and high-speed streams, that affect the Earth. These events modulate the solar wind that permeates near-Earth space and its interaction with the Earth's magnetic field, causing increased geomagnetic activity and geomagnetic storms. In fact, geomagnetic activity is primarily driven by interaction between the solar wind and the Earth's magnetic field; namely, it is driven by magnetic reconnection between the interplanetary magnetic field and the terrestrial magnetic field [*Pulkkinen*, 2007].

Even relatively mild geomagnetic disturbances increase the flux into the atmosphere of the relatively low-energy electrons that are associated with the aurora (energies 1–10 keV), while large geomagnetic storms can produce relativistic electron precipitation (REP) with energies up to several MeV [*Turunen et al.*, 2009]. Although EPP occurs at all times during the 11-year solar magnetic activity cycle, the flux of energetic particles into the atmosphere is not constant. Different space weather events drive geomagnetic activity during different phases of the solar cycle. Violent eruptions associated with CMEs dominate during solar maximum, while the high-speed streams that emanate from coronal holes are the most

prominent feature in the declining phase of the solar cycle [e.g. *Richardson et al.*, 2000]. If the coronal holes persist for more than 27 days (solar rotation period) then the high-speed streams appear with each solar rotation, or "corotate" with the Sun [*Tsurutani et al.*, 2006]. Occasionally higher-speed streams overtake slower-speed streams ahead of them to form what are known as corotating interaction regions (CIRs) [*Balogh et al.*, 1999]. CIRs drive geomagnetic storms that lead to continuous auroral zone activity for anywhere from a few to 27 days [*Tsurutani and Gonzalez*, 1987]. cosmic rays. Figure 1.1 gives an overview of the particle populations that are capable of producing NO_x in the atmosphere as a result of various space weather events.

Solar energetic particles (SEPs), which include protons, neutrons, electrons, alpha particles, and heavier ions, derive their energy from the solar magnetic field [*Ryan et al.*, 2000]. (The term SPE introduced above refers to the proton portion of SEPs.) SEPs were first discovered in the 1940s when, during solar flares, increased ionization was observed in ionization chambers located on the surface of the Earth [*Forbush et al.*, 1950]. We have since discovered that shock waves driven by CMEs and solar flares accelerate SEPs at the sun to energies of 1–1000 MeV [*Reames*, 1999]. CMEs can initiate moderate to intense geomagnetic storms that last for ∼1–2 days and cause the auroral oval to expand to subauroral latitudes. These events happen sporadically and occur most frequently during the maximum of the 11-year solar cycle [*Jackman et al.*, 1990]. At high geomagnetic latitudes, the geomagnetic field lines are directly connected to the solar wind during magnetic reconnection events. Therefore the polar regions are highly susceptible to SEPs, and they deposit their energy in the polar caps (geomagnetic latitudes $> 60°$) from 20–100 km altitude. During particularly strong geomagnetic storms, the polar cap region expands to lower latitudes.

Other particles that enter the atmosphere, but not via the solar wind directly, are those incorporated into the Earth's magnetosphere. These include radiation belt electrons, discrete and diffuse auroral particles, and ring current protons. Energetic particles enter the Earth's magnetosphere during magnetic reconnection and through turbulent interactions

	Solar Energetic Particles (SEP)	Auroral Particles		Ring Current	Radiation Belts	High Energy Polar Rain
		Discrete	Diffuse			
type	Mostly H^+, infrequent e^-	e^-, H^+/H	e-, H^+/H	Mostly H^+; significant O^+ during strong storms	Mostly e-; fewer H^+	e^-
source	sun	magneto-tail	magneto-tail	Inner magne-tosphere	Inner & outer belts	solar wind
energy range	10-1000 MeV	1-10 keV	10-300 keV	1-300 keV	$\geq$ 100 keV	0.4-10 keV
deposition altitudes	20-100 km	$\geq$ 100 km	20-150 km 2nd peak <50 km (due to Brems-strahlung)	$\geq$ 100 km	30-80 km; 2nd peak < 50 km (due to Brems-strahlung)	$\geq$ 100 km
location	polar cap	auroral oval	auroral oval	subauroral	subauroral	polar cap
duration	~1 hr rise time, several days duration	substorm: 1-3 hrs, multiple times per day	essentially permanent feature	Maximum during - 1 day storm main phase	1 day (flux drop-out events) to 10 day (bursty events)	hrs to days within solar wind voids

Figure 1.1: Characteristics of EPP that can produce NO_x in the atmosphere. e^- refers to electrons, and H^+ refers to protons.

along the boundary [*Dungey*, 1961; *Axford and Hines*, 1961]. From the magnetosphere they are accelerated through various magnetospheric processes into the atmosphere.

The outer radiation belt is populated by electrons during geomagnetic storms that result from CMEs or high-speed streams. In the aftermath of geomagnetic storms, high fluxes of relativistic electrons are accelerated to energies greater than 100 keV from the outer radiation belt into the atmosphere. They deposit their energy from ∼30–80 km in the subauroral regions ($\sim 55-65^\circ$ geomagnetic latitude). Bremsstrahlung X-rays from collisions between energetic particles and neutral gas particles can penetrate below 50 km, which leads to a secondary ionization rate maximum in the stratosphere [*Brasseur and Solomon*, 2005]. Energetic electron precipitation from the radiation belts occurs on different timescales with different energy ranges and is driven by a wide variety of mechanisms, and there are still significant gaps in our understanding of the processes involved [*Turunen et al.*, 2009].

The particle populations that are most relevant to the EPP IE are lower energy electrons and protons from auroral and ring current processes that deposit their energy above ∼90 km. Auroral particle precipitation is virtually continuous throughout the solar cycle. Auroral particles come in two different forms: diffuse and discrete. The diffuse aurora is primarily caused by electrons that have energies from ∼0.1–30 keV and come from the solar wind through the plasmasheet [*Eather and Mende*, 1971]. *Thorne et al.* [2010] showed that chorus waves, a type of magnetospheric plasma wave, are responsible for the electron scattering that leads to diffuse auroral precipitation in the atmosphere. Diffuse auroral electrons precipitate in the auroral oval ($\sim 60-75^\circ$ geomagnetic latitude) on a continual basis and are an essentially permanent feature. The majority of the total auroral energy flux into the atmosphere is attributed to the diffuse aurora [*Newell et al.*, 2009]. Discrete auroral electrons, like diffuse auroral electrons, come from the plasmasheet and precipitate in the auroral oval. They have energies ranging from 1–10 keV and penetrate to the lower thermosphere (above ∼100 km). Ring current protons come from the inner magnetosphere and precipitate in the subauroral regions. They occur during substorms, and they range in energy from 1 to 300

keV.

EPP has many significant impacts. First, precipitation of radiation belt particles constitutes a major loss process for the radiation belts. Second, it provides the largest energy input to the polar atmosphere in the absence of solar radiation, i.e., in the polar night. EPP causes changes in chemical composition from the stratosphere though the thermosphere, including changes to radiatively active species. As such, EPP is a coupling agent that transmits and redistributes solar energy throughout the atmosphere. Lastly, in addition to the effects of space weather events and EPP on the atmosphere, space weather effects cause harm to humans in space and to orbiting satellites, and they can disrupt communications and electrical power networks [*Baker*, 2002]. Thus there are many compelling reasons to study EPP and its effects on the atmosphere.

1.4 EPP-NO_x Production

When precipitating particles enter the atmosphere, they travel with helical trajectories along the geomagnetic field lines until colliding with an atmospheric constituent [*Thorne*, 1980]. The collisions result in the ionization or dissociative ionization of molecular nitrogen (N_2) and molecular oxygen (O_2), which leads to the formation of the ions N_2^+, O_2^+, N^+, and O^+ and subsequent ion reactions that produce NO^+ [e.g., *Marsh et al.*, 2007]. NO^+ and O_2^+ are the dominant ion species throughout the MLT [*Roble*, 1995]. Ionization or dissociative ionization reactions from impact of energetic electrons on O_2 and N_2 include [*Rusch et al.*, 1981; *Brasseur and Solomon*, 2005]:

$$O_2 + e^* \rightarrow O_2^+ + 2e \tag{1.3}$$

$$O_2 + e^* \rightarrow O + O^+ + 2e \tag{1.4}$$

$$N_2 + e^* \rightarrow N_2^+ + 2e \tag{1.5}$$

$$N_2 + e^* \rightarrow N(^4S,^2D) + N^+ + 2e \tag{1.6}$$

$$N_2 + e^* \rightarrow 2N(^4S,^2D) + 2e \quad (1.7)$$

where e^* represents energetic electrons. Reactions between the ions create excited nitrogen atoms, which combine with O_2 to form NO. These reactions are discussed in detail below. Higher energy particles also produce a substantial flux of secondary electrons with energies between ∼10 and 100 keV that transfer considerable amounts of energy to the atmosphere and also participate in the formation of ions [*Brasseur and Solomon*, 2005]. Figure 1.2 shows the ionization rate as a function of altitude for the particle populations most relevant to the production of EPP-NO_x (auroral electrons, medium and high energy electrons, and SPEs). The peak ionization rate is at ∼100 km for auroral electrons, ∼80 km for medium and high energy electrons, and ∼40 km for SPEs.

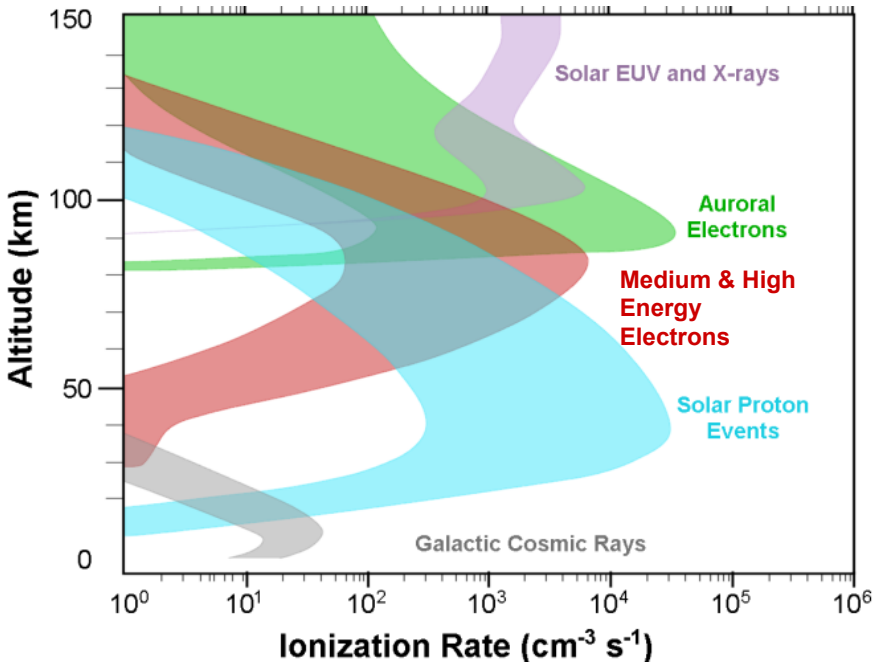

Figure 1.2: Ionization rate as a function of altitude for different particle populations.

As Figure 1.2 shows, the ionization rate and therefore the production of EPP-NO_x in the atmosphere varies depending on the source, energy, momentum, and flux of the incoming particles [e.g., *Crutzen et al.*, 1975; *Gylvan Meira*, 1971; *Narcisi et al.*, 1972; *Rusch et al.*,

1981]. Figure 1.3 shows the penetration depth of electrons and protons that are vertically incident at the top of the atmosphere as a function of the particle energy.

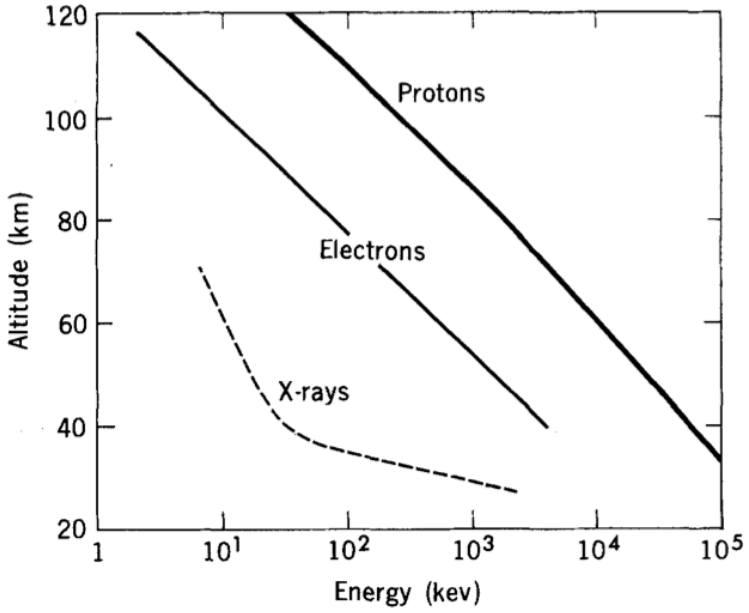

Figure 1.3: The nominal penetration depth of electrons and protons vertically incident at the top of the atmosphere as a function of particle energy. From *Thorne* [1980].

EPP-NO_x is produced in the stratosphere by SEPs such as high-energy electrons (E > 300 keV) and protons (E > 30 MeV), but this happens sporadically during periods of strong geomagnetic activity as discussed in the previous section. The influence of SEPs on the stratosphere falls under the umbrella of what is known as the EPP Direct Effect (EPP DE) because the particles deposit their energy and create EPP-NO_x directly in the stratosphere. *Vitt and Jackman* [1996], for example, estimated that up to ∼10% of the annual stratospheric odd nitrogen (NO_y = N + NO + NO_2 + NO_3 + $2N_2O_5$ + HNO_3 + HO_2NO_2 + $ClONO_2$ + $BrONO_2$) source is from the EPP DE. The impact of SPEs on stratospheric O_3 from 1963–2005 is discussed by *Jackman and Fleming* [2008]. Electrons from the radiation belt also contribute to the EPP DE through a wide variety of mechanisms that are poorly understood [*Turunen et al.*, 2009]. Not only are the mechanisms controlling the precipitation elusive, a clear understanding of the impacts also remains elusive because the spatial and temporal

distributions are poorly known [*Horne et al.*, 2009].

Precipitating particles with much lower energies lead to EPP-NO_x production in the MLT region. EPP-NO_x produced above ∼90 km is primarily due to ionization resulting from routine precipitation of low energy electrons (energy < 30 keV) and protons (energy < 1 MeV). For example, observations from the Student Nitric Oxide Explorer (SNOE) show that NO in the high-latitude thermosphere is the result of the precipitation of auroral electrons with energies of ∼1–10 keV into the auroral oval (60°–70° geomagnetic latitude) [*Barth et al.*, 2003; *Solomon et al.*, 1999]. EPP produces excited $N(^2D)$, which combines with O_2 to form NO [*Thorne*, 1980]:

$$N(^2D) + O_2 \rightarrow NO + O. \tag{1.8}$$

NO can also form from the reaction of O_2 with $N(^4S)$, but this reaction is slow compared to (1.8) [*Rusch et al.*, 1981]. In the thermosphere, $N(^2D)$ is formed through the following recombination and ion-neutral reactions [*Brasseur and Solomon*, 2005]:

$$e + NO^+ \rightarrow 2N(^4S,^2D) + O \tag{1.9}$$

$$e + N_2^+ \rightarrow N(^4S,^2D) + O \tag{1.10}$$

$$O + N_2^+ \rightarrow NO^+ + N(^4S,^2D) \tag{1.11}$$

$$O_2 + N^+ \rightarrow N(^4S,^2D) + O_2^+ \tag{1.12}$$

where NO^+ is formed by

$$O_2 + N^+ \rightarrow NO^+ + O$$

$$N_2 + O^+ \rightarrow NO^+ + N.$$

NO is destroyed through cannibalistic reaction with $N(^4S)$:

$$N(^4S) + NO \rightarrow N_2 + O. \tag{1.13}$$

so there can only be a net production of NO if the branching ratio of $N(^4S)$ to $N(^2D)$ is less than 50% in reactions (1.6), (1.7), and (1.9)–(1.12) [e.g., *Garcia*, 1992]. Deviations

from a 50%-50% branching ratio can have large effects on lower thermospheric NO densities, making the branching ratio an extremely important parameter in NO_x chemistry [*Brasseur and Solomon*, 2005]. However, current estimates of the partitioning between ground and excited state N atoms, both theoretical and empirical, vary widely [*Sinnhuber et al.*, 2012].

In the sunlit mesosphere and thermosphere, NO has a lifetime of only a few days due to rapid photodissociation in the δ-bands (189.394-191.663 nm and 181.571-183.570 nm) [*Frederick et al.*, 1983]:

$$NO + h\nu \rightarrow N(^4S) + O \tag{1.14}$$

and subsequent combination of $N(^4S)$ and NO in reaction (1.13). However, in the absence of sunlight in the polar night region (1.14) is absent, and the loss rate from (1.13) is small so that NO can be transported to the stratosphere via a combination of diffusion and the descending mean meridional circulation at the winter pole. The lifetime of NO increases from days to weeks or months in the polar night, and vertical winds on the order of a few cm/s can effectively transport NO to the mesosphere [*Siskind and Russell*, 1996; *Marsh and Roble*, 2002]. As NO descends to the lower mesosphere it reacts with O_3 to produce NO_2 [e.g., *Cohen and Murphy*, 2003]. The process whereby NO_x created in the MLT is transported to the stratosphere was named the EPP IE by *Randall et al.* [2006]. There are still large uncertainties about the exact altitude at which the EPP-NO_x that contributes to the EPP IE is created and, therefore, which particle populations contribute most to the EPP IE. It is generally thought that the source of EPP for the EPP IE is low-energy auroral and ring-current electrons that precipitate on a regular basis. This is supported indirectly by the high correlation between auroral input and the amount of EPP-NO_x entering the SH stratosphere [*Randall et al.*, 2007].

The EPP IE was theoretically predicted by *Solomon et al.* [1982] and *Garcia and Solomon* [1983] using a 2-D model. *Solomon and Garcia* [1984] confirmed the theoretical prediction indirectly by comparing the predicted changes in O_3 due to the transport of NO

for varying levels of solar activity to observed O_3. Direct satellite evidence of the EPP IE was first obtained from LIMS during the northern hemisphere (NH) winter of 1978-1979 [*Russell et al.*, 1984]. The EPP IE has since been observed a number of times, along with evidence for the destruction of O_3 by EPP-NO_x. For example, *Randall et al.* [2007] estimated that the EPP IE contributes up to 10% of the global annual NO_y source in the stratosphere and up to 40% of the polar NO_y source. An overview of the observational evidence for the EPP IE is given in Section 1.7.

One of the more challenging aspects of studying the EPP IE is that chemical and dynamical lifetimes are often comparable in the MLT, which means that a full understanding requires knowledge of the contribution of both chemistry and dynamics [*Marsh*, 2011]. These topics are discussed in detail in the following sections.

1.5 Stratospheric NO_x Chemistry

As NO descends to the stratosphere in the polar region, some of the NO is converted to NO_2 as O_3 increases via

$$NO + O_3 \rightarrow NO_2 + O_2.$$

NO and NO_2 are in photochemical equilibrium throughout the sunlit stratosphere, where the ratio is approximately 1 below 40 km and favors NO with increasing altitude because of higher atomic oxygen mixing ratios [*Brasseur and Solomon*, 2005]. During the day, NO_2 is rapidly converted back to NO by either:

$$NO_2 + O \rightarrow NO + O_2$$

or

$$NO_2 + h\nu \rightarrow NO + O(^3P).$$

In the night, NO is quickly converted into NO_2 up to altitudes of about 60 km, which makes NO_2 a decent proxy for NO_x in the polar night. NO_2 can be converted to NO_3 by reaction

with O_3. NO_3 then combines with NO_2 to form N_2O_5:

$$NO_2 + O_3 \rightarrow NO_3 + O_2$$

$$NO_2 + NO_3 + M \rightarrow N_2O_5 + M.$$

Both N_2O_5 and NO_3 are quickly photolyzed in the day to return NO_x. Therefore the distribution of NO_x in the stratosphere has a large diurnal variation. N_2O_5 provides an important reservoir for nitrogen compounds in the polar winter. N_2O_5 can be further converted to HNO_3 by heterogeneous reaction:

$$N_2O_5(g) + H_2O(l, s) + M \rightarrow 2HNO_3.$$

on the surface of sulfate aerosols, ice particles, water droplets, nitric acid ice, and ternary solution particles [*Brasseur and Solomon*, 2005]. If the temperature is sufficiently low, this reaction also takes place on the surface of polar stratospheric clouds. Gravitational sedimentation of HNO_3-containing particles provides a mechanism to denitrify the lower polar stratosphere.

1.6 Dynamics and Transport

In the absence of sunlight, NO created in the thermosphere is transported by diffusion to ∼95 km in a few hours to a few days [*Banks and Kockarts*, 1973; *Siskind et al.*, 1989; *Cleary*, 1985; *Siskind*, 1994; *Yonker and Bailey*, 2008; *Richards*, 2004]. The net mean motion of parcels in the middle atmosphere can be approximated by the diabatic circulation. The diabatic circulation in the middle atmosphere at solstice is characterized by rising motion in the stratosphere and mesosphere at the summer pole, cross-equatorial flow from the summer pole to the winter pole, and sinking motion in the stratosphere and mesosphere at the winter pole. Figure 1.4 shows a schematic of the diabatic circulation at solstice. Descent rates in the polar mesosphere are ∼1–2 km/day [*Greenblatt et al.*, 2002, and references therein]. *Siskind et al.* [1997, 2000] showed that NO can be transported to lower latitudes by horizontal

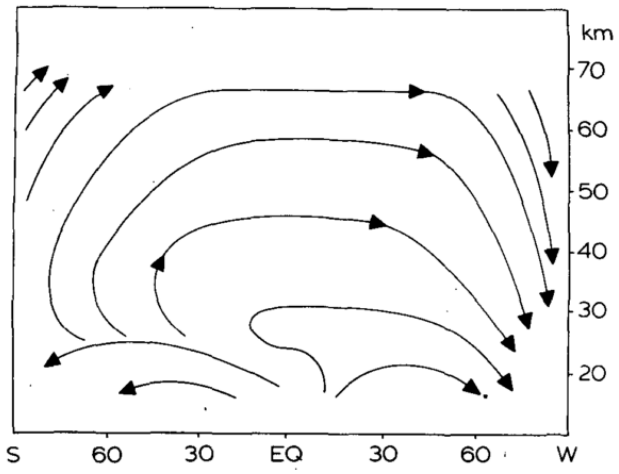

Figure 1.4: Schematic of diabatic circulation in the middle atmosphere during solstice. From *Dunkerton* [1978].

winds and waves, and if NO is transported to sunlit latitudes in the mesosphere it will be photochemically destroyed in a matter of days (see Section 1.4). As air descends in the polar winter, it eventually meets the polar vortex. The polar vortex acts as a transport barrier to lower latitudes, and air in the polar vortex can be transported to the lower stratosphere by the end of winter [e.g. *Manney et al.*, 1994]. Once in the stratosphere, NO_x is rapidly converted to other NO_y constituents. The photochemical lifetime of stratospheric NO_y is months to years, which determines the timescale over which it can influence catalytic O_3 cycles.

The most meaningful way to represent the net transport from the zonal mean circulation is the transformed Eulerian mean (TEM) framework [*Andrews and McIntyre*, 1976]. As its name implies, a transformation, $* : (\overline{v}, \overline{w}) \mapsto (\overline{v}^*, \overline{w}^*)$, is defined such that when $(\overline{v}^*, \overline{w}^*)$ is utilized in the zonal mean equations the problem of large cancellation between the eddy heat flux and adiabatic cooling terms in the Eulerian mean thermodynamic equation is avoided. For a derivation of the TEM see, e.g., *Andrews and McIntyre* [1976]; *Brasseur and Solomon* [2005]; *Holton* [2004]. The TEM formulation provides a better representation of the actual motion of air parcels in the latitude-height plane than the conventional Eulerian mean. The impact of the TEM circulation on the transport of species such as NO, CO, and H_2O is evident in satellite data as large meridional gradients in mixing ratios, and the mixing ratio patterns are also reproduced in general circulation models [*Marsh*, 2011, and references therein].

The TEM is a wave-driven flow. In the stratosphere the wave forcing is thought to be from stationary planetary waves. According to the Charney-Drazin criterion, vertical planetary wave propagation requires that the zonal wind be westerly. Planetary waves can therefore only propagate in the stratosphere in the winter hemisphere [*Charney and Drazin*, 1961]. The momentum imparted to the zonal mean flow by planetary waves maintains the polar winter stratosphere above radiative equilibrium, which produces a net radiative cooling in that region and corresponding sinking vertical motion. While zonal forcing in the strato-

sphere is the result of planetary wave breaking, the zonal forcing in the mesosphere results from GWs. Vertically propagating GWs are generated by a variety of highly temporally variable sources including flow over mountains, shear instabilities, convection, and geostrophic adjustment in regions of baroclinic instability [e.g., *Richter et al.*, 2010]. They can have a phase speed that is westward or eastward relative to the mean flow, but their phase speed must be greater than the mean flow if their phase speed is in the same direction as the mean flow. They are filtered by the mean flow such that GWs with eastward phase speeds reach the mesosphere in the summer, and GWs with westward phase speeds reach the mesosphere in the winter. Figure 1.5 shows a schematic of near-solstice zonal winds and GW filtering by the mean flow. GWs deposit a net westerly momentum in the summer mesosphere and a net easterly momentum in the winter mesosphere. This produces rising motion at the summer pole and sinking at the winter pole. Both types of wave forcing produce descent at the winter pole. This subsidence is an important factor controlling the variability of the EPP IE since it controls the amount of EPP-NO_x that is transported to the stratosphere from higher altitudes.

Under undisturbed winter conditions, the meridional temperature gradient gives rise to a strong westerly polar vortex that increases in speed with height and reaches a maximum around 60 km, and the maximum zonal winds tilt equatorward with height. The polar vortex acts as a barrier of horizontal transport, as is evidenced by the existence of strong meridional gradients in potential vorticity and tracer species [*Holton*, 2004]. If the EPP-NO_x is sequestered by the polar vortex, it is more efficiently transported to the stratosphere where it interferes with catalytic cycles of O_3. Therefore the size and strength of the polar vortex are important factors in determining the extent to which EPP-NO_x can influence the stratosphere and O_3 distributions.

In about one out of every two years, the influence of vertically propagating planetary waves produces a dramatic deceleration of the mean flow. This occurs when the amplitude of the planetary waves rapidly increases with time. The deceleration of the westerly jet allows

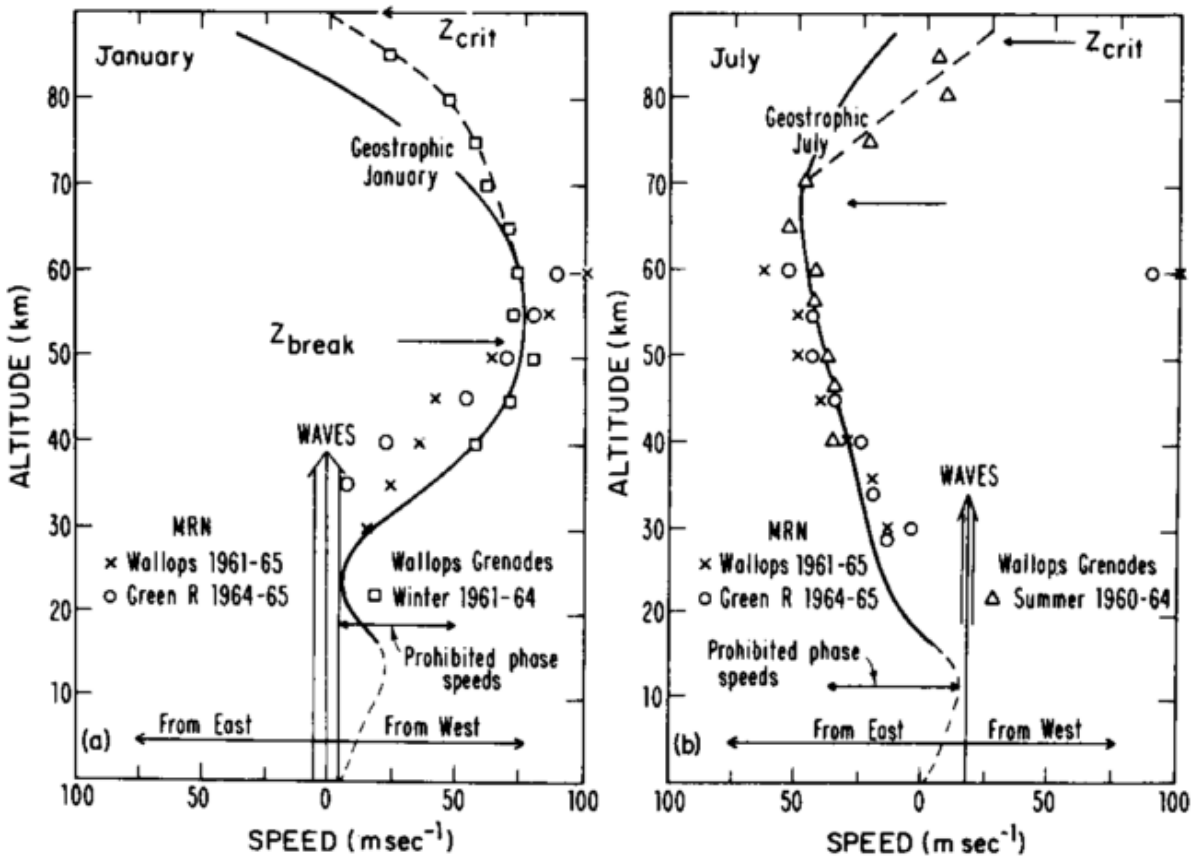

Figure 1.5: Zonal wind as a function of altitude at mid-latitudes for (a) January and (b) July. Also shown are prohibited wave phase speeds for mesospheric GWs of tropospheric origin. From *Lindzen* [1981].

more waves to propagate into the stratosphere, which further decelerate the flow. The rapid deceleration of the jet causes a sudden warming in the polar region, with a reversal of the equator-to-pole temperature gradient. Because of the reversal of the temperature gradient, the thermal wind balance then requires an easterly zonal flow. This can cause the polar vortex to become highly contorted and either pushed off center or split into two. Depending on the time of the warming, the westerly circulation can be reestablished. The easterly flow acts as a barrier to further vertical propagation of planetary waves, and the westerly jet reforms as radiative processes restore the winter circulation.

Stratospheric warming events are usually divided into four categories as described in *Labitzke and Naujokat* [2000]. The four categories are defined (somewhat arbitrarily) as follows: (1) Major Warming–reversal of the westerly winds and temperature gradient at the 10 hPa level; (2) Minor Warming–reversal of the temperature gradient, but not the winds; (3) Canadian Warming–reversal of the temperature gradient in early winter with some disruption in wind direction; (4) Final Warming–the transition between winter and summer circulation patterns. The criteria for a major SSW event are widely used and often cited as the World Meteorological Organization's criteria. Numerous observational studies of major SSW events have shown that enhanced propagation of planetary waves from the troposphere, primarily zonal wave numbers 1 and 2, is essential for the development of the warming events [*Labitzke*, 1981]. Major SSW events have occurred in the NH about once every other year on average since they were first discovered over Berlin in 1952 by *Scherhag* [1952]. First dubbed the "Berlin phenomenon," the discovery of major SSW events led to increased interest in the stratosphere and copious new measurements thereof [*Labitzke and van Loon*, 1999].

During a major SSW event, the stratopause descends in altitude and the stratosphere becomes virtually isothermal for a few days before the stratopause reforms. A recent discovery is that after some major SSW events, the stratopause reforms as high as ∼80 km, an altitude characteristic of the mesosphere. This is referred to as an elevated stratopause (ES)

event and has been studied intensely in the most recent decade [e.g., *Manney et al.*, 2008, 2009a,b; *Siskind et al.*, 2010]. The ES is caused by changes in GW filtering after the major SSW event. The changes in GW filtering result in a net easterly GW drag in the mesosphere and lead to a large increase in $\overline{w}^*$. The enhanced descent causes adiabatic heating around 80 km and forms the new stratopause. ES events occurred in the NH winters of 2003–2004, 2005–2006 and 2008–2009 and had a pronounced impact on the descent of polar NO_x [e.g., *Hauchecorne et al.*, 2007; *López-Puertas et al.*, 2005a; *Randall et al.*, 2005, 2006, 2009; *Siskind et al.*, 2007]. It is particularly of note that the level of EPP was relatively low in 2005–2006 and 2008–2009, yet observed NO_x mixing ratios reaching the upper stratosphere were just as high or higher than years with a higher level of EPP [e.g., *Holt et al.*, 2012; *Randall et al.*, 2006, 2009; *Seppälä et al.*, 2007a], highlighting the importance of dynamics in the NH.

In the SH major SSW events happen much less frequently; in fact, there has been only one major SSW event on record, which occurred in 2002 [*Baldwin et al.*, 2003; *Krüger et al.*, 2005; *Varotsos*, 2002]. The dichotomy between the SH and NH is attributed to the greater planetary wave activity in the NH resulting from topography. This dichotomy in major SSW events is also mirrored in the EPP-NO_x that is transported to the stratosphere. In the SH, the variability of EPP-NO_x correlates well with the variability of the level of EPP, whereas in the NH it does not. It is not surprising then that major SSW events are thought to have a direct relationship with the amount of EPP-NO_x that can be transported to the stratosphere through their influence on the meteorological conditions. The ability of general circulation models to reproduce the frequency and variability of major SSW events is pivotal to our ability to correctly model the EPP IE. Chapters 3 and 4 explore some of the important transport mechanisms for the EPP IE using WACCM.

1.7 Satellite Observations of the EPP Indirect Effect

Several satellite instruments have observed the EPP IE since the beginning of the satellite era. However, none of the satellite instruments has been ideally suited to study the

EPP IE. What we need is an instrument that continuously measures NO and NO_2 throughout the polar winter from the stratosphere to the lower thermosphere. As it stands, we only have polar night measurements of NO_x in the stratosphere and lower mesosphere, and, therefore, we have no direct observational evidence of EPP-NO_x descending from the altitude at which it was created to the stratosphere. Current studies infer that NO_x came from higher altitudes by looking at its descent or use tracer correlations to attribute NO_x to EPP. Another complication is that most of the satellite evidence for the EPP IE has come from solar occultation instruments, and quantification of the EPP IE based on solar occultation instruments is difficult because of the limited geographical coverage and complete lack of data where it is really needed: the polar night. Therefore estimates of the EPP IE based on solar occultation data are best considered as lower bounds. Figure 1.6 gives an overview of the current observational evidence of the EPP IE. In the polar night, NO_x above ~70 km

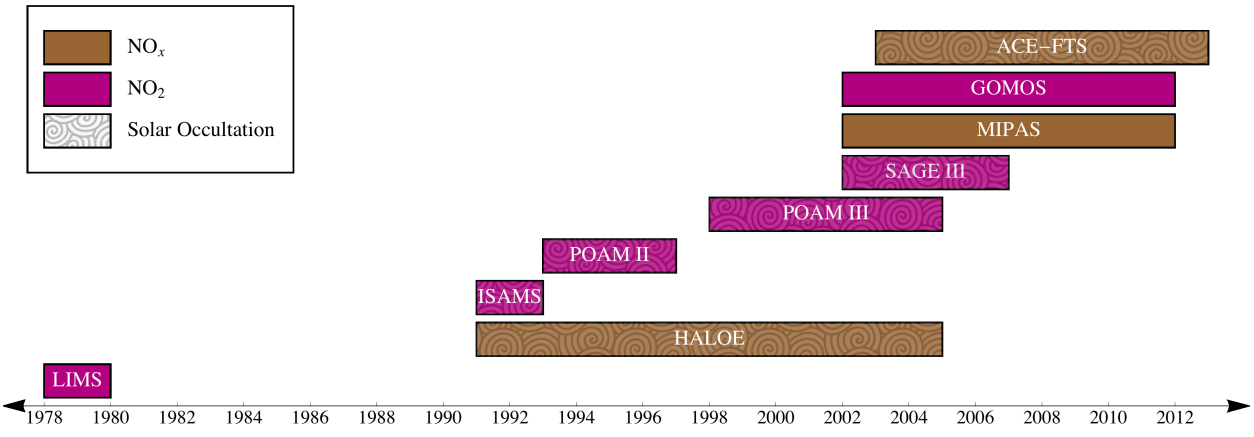

Figure 1.6: Satellite observations of the EPP IE.

is mainly in the form of NO and NO_x below ~70 km is mainly in the form of NO_2. Thus nighttime NO_2 below 70 km is an acceptable proxy for NO_x. There are only three instruments that have measured both NO and NO_2 below 70 km (the Halogen Occultation Experiment (HALOE), the Atmospheric Chemistry Experiment (ACE), and the Michelson Interferometer

for Passive Atmospheric Sounding (MIPAS)) and only one instrument that measured both NO and NO_2 in the polar night (MIPAS). The only remaining satellite instrument capable of measuring NO_x is ACE-FTS. Two instruments measured NO_2 in the polar night but with limited temporal coverage. LIMS provided nighttime NO_2 measurements for only one winter NH winter, and the Global Ozone Monitoring By Occultation of Stars (GOMOS) had no late winter coverage when the EPP IE is most relevant.

As mentioned above, the LIMS satellite instrument provided the first experimental evidence for the EPP IE. As its name implies LIMS was a limb scanning instrument capable of measuring in the polar night. *Russell et al.* [1984] used a special radiance averaging technique to obtain profiles of NO_x with an improved signal-to-noise ratio. They showed that over the course of the 1978–1979 NH winter, thermospheric NO_x was transported to the stratosphere in the polar night. Poleward of 70 N, peak NO_2 mixing ratios measured by LIMS approached 175 ppbv at ∼70 km. Figure 1.7 shows LIMS nighttime NO_2 mixing ratios poleward of 70 N.

In the decade following the LIMS mission, almost no observational studies reported on the EPP IE. One exception in the intervening years is *Callis et al.* [1998a]. They showed that simulations including the effects of energetic electron precipitation (EEP) agreed better with Stratospheric Aerosol and Gas Experiment II (SAGE II) NO_2 measurements than simulations without EEP effects in the altitude range 25 to 40 km between 24 October 1984 and 31 December 1987. The simulated fluctuations in stratospheric NO_2 and NO_y were mostly due to varying rates of formation of NO_y in the mesosphere with subsequent transport into the stratosphere. That the simulations with EEP agree better with the observations indicates that the EPP IE was evident in SAGE II NO_2; however, it should be emphasized that these conclusions are not based directly on observational evidence. That is, since the descent of NO_2 to the stratosphere was not directly observed, they required a model to attribute SAGE II NO_2 to the EPP IE.

Using nighttime NO_2 observations from the Improved Stratospheric and Mesospheric

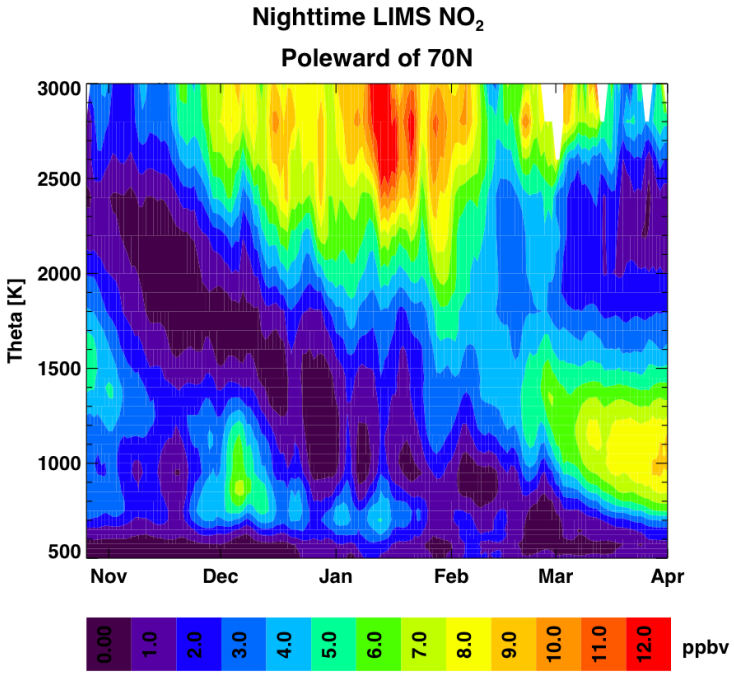

Figure 1.7: Nighttime LIMS NO_2 mixing ratios averaged poleward of 70 N.

Sounder (ISAMS) on the Upper Atmosphere Research Satellite (UARS) together with precipitating electron data from the National Oceanic and Atmospheric Administration (NOAA) 12 satellite, *Callis and Lambeth* [1998] showed evidence for the EPP IE. They calculated significant increases in NO_y formation rates in the lower mesosphere (near 65 km) in November 1991 and May 1992 due to energetic electron precipitation (4 keV $\leq$ E $\leq$1 MeV) and showed that the descent of nighttime NO_2 observed by ISAMS into the stratosphere in the NH in November 1991 and the SH in May 1992 was attributable to this mesospheric production of NO_y and subsequent descent into the stratosphere.

Rinsland et al. [1996] showed that NO_y mixing ratios measured by the Atmospheric Trace Molecule Spectroscopy (ATMOS) instrument inside the SH vortex around 700 K ($\sim$27 km) in November 1994 were higher than those derived from a fit to NO_y versus N_2O mixing ratios measured outside the vortex. They showed that the elevated NO_y inside the vortex also corresponded with low N_2O mixing ratios, indicating that the NO_y came from the upper atmosphere. They attributed the elevated stratospheric NO_y to downward transport of NO_y produced in the thermosphere and mesosphere.

Randall et al. [1998] used measurements from the Polar Ozone and Aerosol Measurement (POAM II) from October 1993 through mid-November 1996 to study stratospheric NO_2 in the polar regions in both hemispheres between $\sim$20 and 40 km. In agreement with *Rinsland et al.* [1996], they reported anomalously high NO_2 mixing ratios measured in the SH late winter/early spring of 1994, and they also concluded that the high NO_2 mixing ratios in 1994 resulted from downward transport of EPP-NO_x from the mesosphere or thermosphere inside the polar vortex. A smaller enhancement was seen in the 1995 SH winter but not in the 1996 NH winter, and none of the NH winters showed an increase in NO_2 at the altitudes presented. They also used measurements of polar NO_2 and O_3 throughout the winter and spring, which had not yet been done, to show that localized reductions in O_3 of up to 40% corresponded to the increases in NO_2 in the SH in 1994 and 1995. Furthermore, even though the analysis only included three years, it supported the idea that the amount

of NO_x transported to the stratosphere has high interannual variability and correlates with the level of EPP in the SH: the A_p index was highest in 1994 and declined through 1996 toward solar minimum.

Siskind and Russell [1996] used NO, NO_2, and CH_4 from the Halogen Occultation Experiment (HALOE) on UARS to investigate the EPP IE in both hemispheres. HALOE is a solar occultation instrument and only observed as far north as 55°N during the polar winter. Nevertheless *Siskind and Russell* [1996] still showed evidence of EPP-NO_x being transported to the stratosphere. The SH enhancements were larger than those in the NH, which they suggested could be attributed to either stronger descent in the SH or greater horizontal mixing in the SH that transported the EPP-NO_x to lower latitudes where HALOE could observe it. However, because of the limited latitudinal coverage of HALOE, large EPP-NO_x enhancements in the NH could not be ruled out. They also pointed out that the NO_x enhancements observed by HALOE did not last as long into spring compared to modeling studies, which suggested that the models were overestimating the contribution of EPP-NO_x to O_3 depletion.

Siskind et al. [2000] used data from HALOE to assess the EPP IE in the SH from 1991–1996. They show a strong correlation between the A_p index and the average column NO_x in the vortex core for each of the SH winters, which corroborated the results of *Randall et al.* [1998]. They quantified the amount of EPP-NO_x, using the relationship between NO_x and the tracer CH_4, and found that in the years with the largest EPP IE, EPP-NO_x contributes ∼3–5% of the N_2O oxidation source to the yearly SH NO_y budget (0.8–1.3 Gmol EPP-NO_x compared to 26–29 Gmol NO_y from N_2O oxidation).

Randall et al. [2001] reported large NO_x enhancements observed by HALOE and POAM in September through October 2000 and accompanying O_3 losses of up to 45% near 33 km. Examination of the tracer H_2O suggested that the altitude of the source region for the SH stratospheric NO_x enhancements was in the mesosphere. They concluded that in every year since the launch of UARS in 1991, NO_x enhancements in the SH polar vortex resulted from

NO_x produced by EPP in the mesosphere.

Based largely on UARS data, *Randall et al.* [2007] showed that EPP-NO_x enhancements were observed in most years in the SH from 1992–2005. With HALOE NO_x and CH_4, they quantified the EPP IE as the amount of EPP-NO_x entering the stratosphere each year and found that the EPP IE varied from 0.1 to 2.6 Gmol per year. They calculated that this represents up to 10% of the SH NO_y budget and up to 40% of the polar NO_y budget. They also found a strong relationship between the amount of EPP-NO_x entering the stratosphere each winter and the seasonally-averaged A_p index. Figure 1.8 (top) shows the EPP IE for each of the SH winters from 1992–2006 and the A_p and f10.7 indices. The EPP IE correlates very highly with the A_p index, showing that variations in the amount of EPP-NO_x transported to the SH from year to year are primarily a function of the EPP-NO_x source. In stark contrast to the EPP IE in the SH, the EPP IE for the NH winters from 1992–1993 to 2006–2007 (bottom) does not correlate at all with the A_p index.

The Environmental Satellite was launched in March 2002 and included the MIPAS and GOMOS instruments, the first satellite instruments since LIMS capable of measuring NO_x or NO_2 in the polar night. Figure 1.9 shows the temporal evolution of MIPAS NO_x for the 2002–2003 and 2003–2004 NH and 2003 SH winters. The three winters show enormous variation in the EPP IE and illustrate the interannual and interhemispheric variability in the EPP IE. In the 2003 SH winter, MIPAS measured peak NO_x mixing ratios of $\sim$200 ppbv in the polar night region between 2500 and 3000 K, representing the highest values ever recorded in the SH and exceeding those measured by LIMS in 1978–1979 [*Funke et al.*, 2005a]. Vortex-average mixing ratios were $\sim$60 ppbv.

Seppälä et al. [2007a] looked at nighttime NO_2 and O_3 from GOMOS in both Arctic and Antarctic winters from 2002–2006. In each winter, GOMOS shows nighttime NO_2 descending to the stratosphere over time. They found that NH stratospheric EPP-NO_x enhancements from 46 to 56 km correlated well with the A_p index for all eight winters included in the study, but these calculations included only the months of October through January. Since

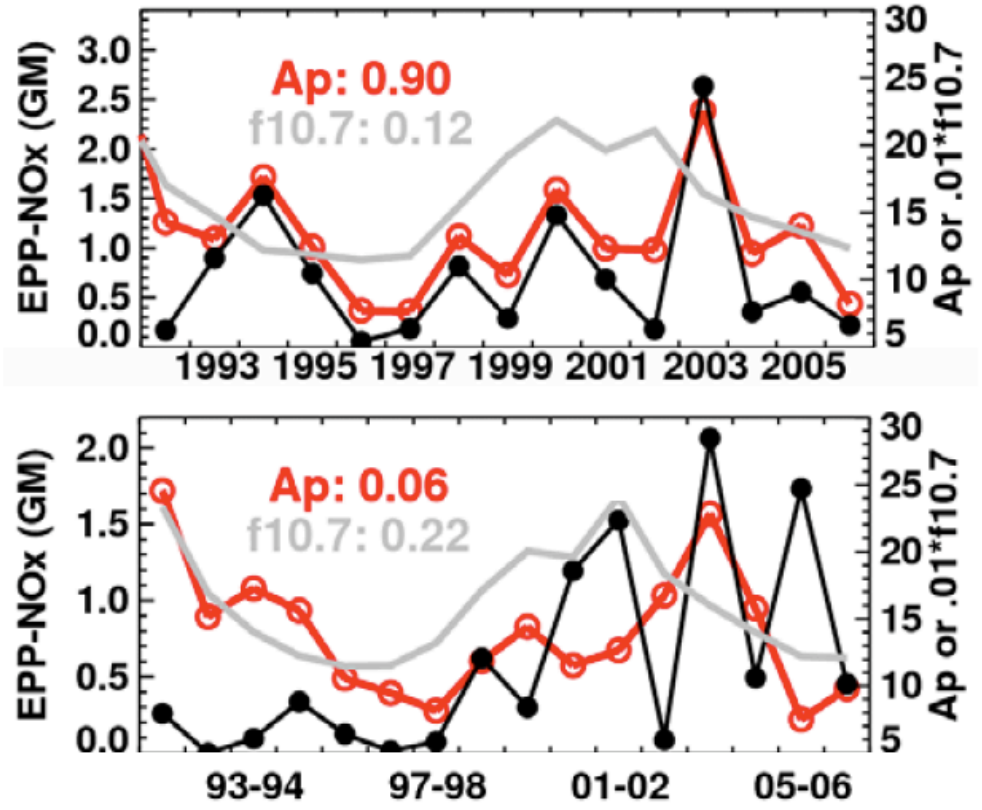

Figure 1.8: EPP-NO_x for (top) 1992–2005 SH winters (black), the A_p index (red), and the f10.7 index (grey). EPP-NO_x for (bottom) 1991–1992 through 2006–2007 NH winters. Adapted from Figure 10 in *Randall et al.* [2007].

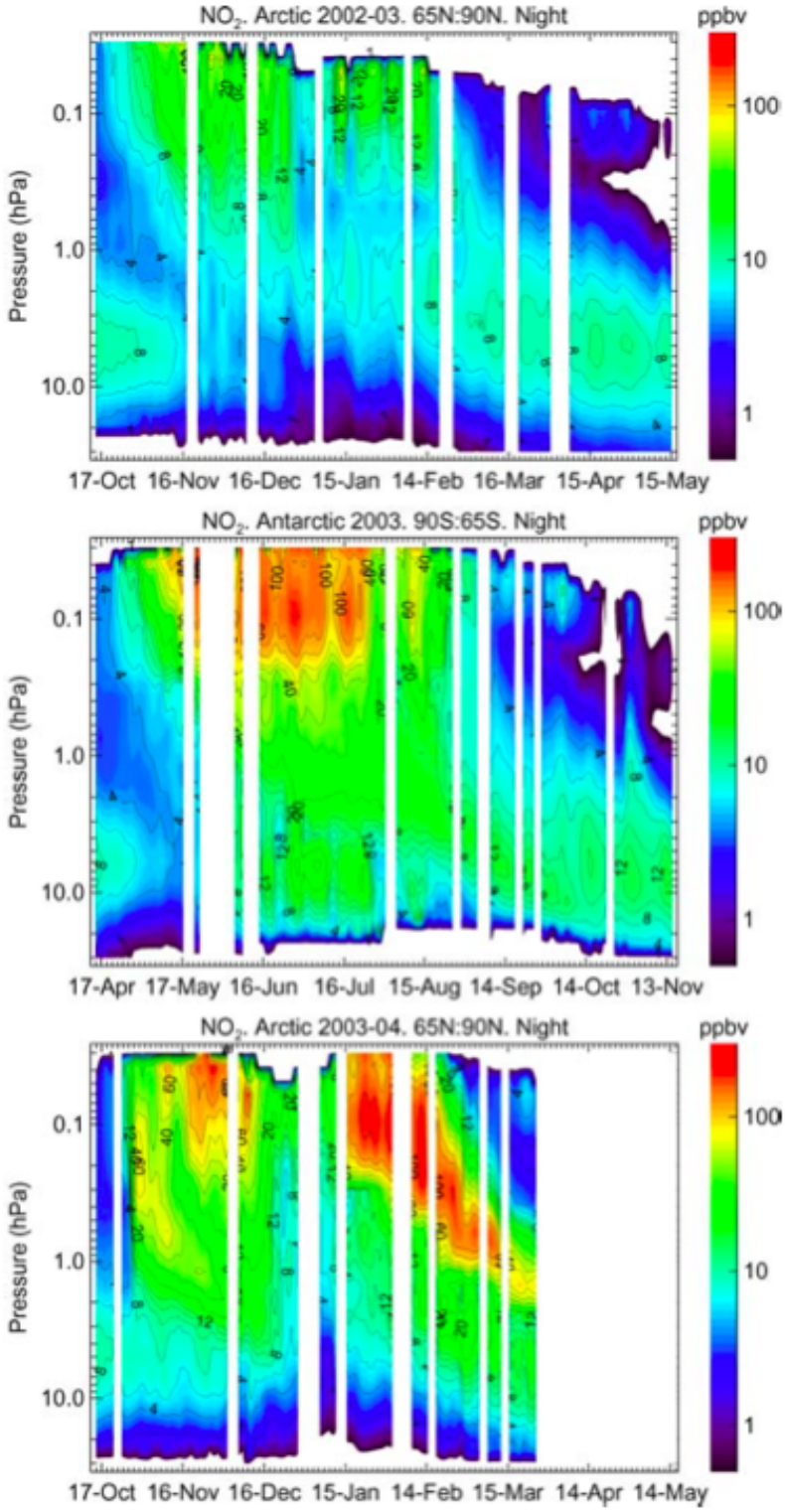

Figure 1.9: Temporal evolution of MIPAS nighttime NO_2 from 65–90°N for (top) the 2002–2003 NH winter, (middle) the 2003 SH winter, and (bottom) the 2003–2004 NH winter. White bands are missing data and other white regions are outside of the scale used. Figure 1 from [*López-Puertas et al.*, 2006].

previous studies have shown that the EPP IE has the largest effect at stratospheric altitudes starting in late January, and GOMOS does not make NH measurements past February, the correlation is most likely not representative of the entire season. Figure 1.10 shows GOMOS nighttime NO_2 and O_3 mixing ratios.

The NH winter of 2003–2004 was a fascinating and unprecedented, in the observational record, NH winter, and interest in the EPP IE skyrocketed as a result of the events of that winter. It began with a period of intense solar activity at the end of October that lasted into November and led to high geomagnetic activity and elevated EPP [e.g., *Gopalswamy et al.*, 2005; *Mewaldt et al.*, 2005]. The so-called Halloween Storms of late October and November 2003 resulted in substantially elevated NO_x and HO_x, and led to depleted O_3 in the upper stratosphere and mesosphere in November [*Degenstein et al.*, 2005; *Jackman et al.*, 2005; *López-Puertas et al.*, 2005a,b; *Orsolini et al.*, 2005; *Rohen et al.*, 2005; *Seppälä et al.*, 2004; *Verronen et al.*, 2005; *von Clarmann et al.*, 2005]. In addition to the high level of EPP, the NH winter of 2003–2004 was also the most dynamically active NH winter on record. A major SSW event in early January was exceptional in both the length of vortex disruption and strength of recovery in the upper stratosphere [*Manney et al.*, 2005]. Following the major SSW event, temperature measurements from the Sounding of the Atmosphere using Broadband Emission Radiometry (SABER) showed that the stratopause reformed at an altitude normally associated with the mesosphere (∼80 km) [*Hauchecorne et al.*, 2007].

Starting in January, following the dramatic major SSW event, NO_x-rich air descended over time in the polar region. This led to unprecedented NH NO_x enhancements and O_3 reductions in the upper stratospheric vortex from March–May 2004. *Natarajan et al.* [2004] reported that HALOE observed NO_x mixing ratios as high as 99.1 ppbv at 68 N at 2 hPa, the largest that had ever been measured in the stratosphere. They used a photochemical model to show that the corresponding reductions in O_3 could be attributed to the large NO_x enhancements. *Rinsland et al.* [2005] reported that the Atmospheric Chemistry Experiment Fourier Transform Spectrometer (ACE-FTS) measured maximum NO_x mixing ratios ∼1361

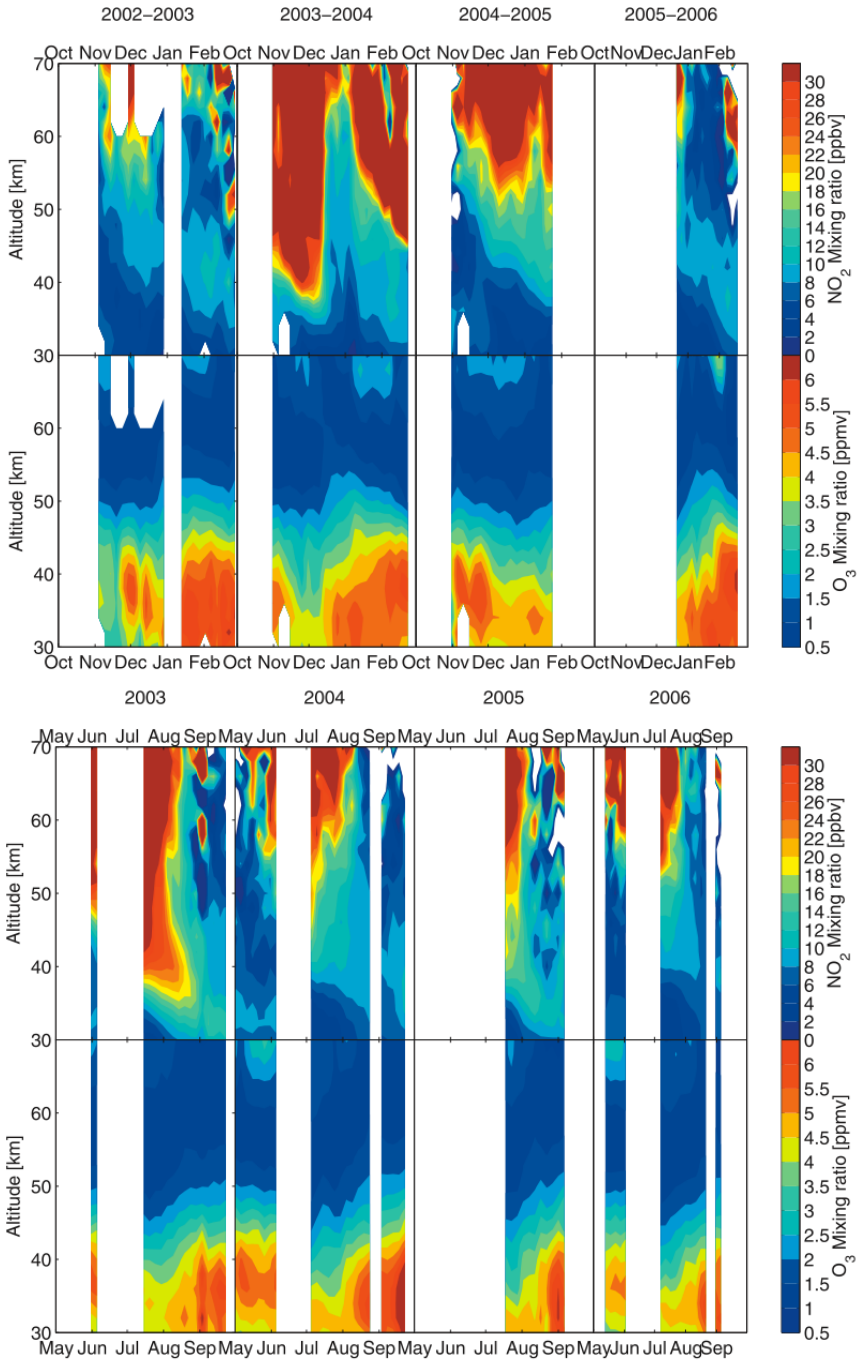

Figure 1.10: GOMOS polar winter NO_2 and O_3 for (top) the NH winters of 2002–2003 through 2005–2006 and (bottom) the SH winters of 2003 through 2006. White areas are missing data or flagged measurements. Figures 2 and 3 from [*Seppälä et al.*, 2007a].

ppbv on February 18 at 0.173 hPa (∼54 km). ACE-FTS made measurements from mid-February through March 2004, and they estimated that maximum NO_x mixing ratios had decreased to ∼159 ppbv by March 23. From mid-January until the end of March 2004, MIPAS observed extraordinary high values of NO_2 in the upper stratosphere of the northern polar region with mean in-vortex values up to 350 ppbv at ∼54 km *López-Puertas et al.* [2005a]. MIPAS also observed to significant in-vortex reductions in O_3 in the mid-February to late March period above the 1750 K potential temperature level.

Randall et al. [2005] used data from multiple satellite instruments (HALOE, SAGE II & III, POAM II & III, MIPAS, and the Optical Spectrograph and InfraRed Imaging System (OSIRIS)) to study the EPP IE in the NH winter of 2003–2004 and compare the 2003–2004 NH winter to other NH winters dating back to 1984. Figure 1.11 is from *Randall et al.* [2005], which compares the temporal evolution of NO_x and O_3 for several of the instruments spanning 1984–2004 and shows that the 2003–2004 NH winter clearly stands out. Compared to other NH winters, Figure 1.11 shows NO_x increases of up to 400% and O_3 reductions of up to 60% in the upper stratospheric vortex from March–May 2004. *Randall et al.* [2005] also found that the increases in NO_x of up to 50% were still detected in July.

In the intervening years, the source of the stratospheric NO_x enhancements following the January 2004 major SSW and ES event has motivated many studies: was it higher particle activity associated with the Halloween Storms, or was the unusually strong descent in the vortex that brought down EPP-NO_x created by routine precipitation of auroral particles? The arguments rely on indirect evidence because no direct evidence of NO_x production and transport mechanisms from the stratosphere to the thermosphere is available for the 2003–2004 NH winter. *Clilverd et al.* [2006] made the case for the latter source by showing that subionospheric radio wave propagation data from Ny Ålesund, Svalbard, Norway was more consistent with the descent of high altitude thermospheric NO_x, generated at ∼120 km by auroral EPP, into the mesosphere than with in situ mesospheric production by higher energy EPP. They also found that the NO_x produced by the Halloween storms had dissipated by

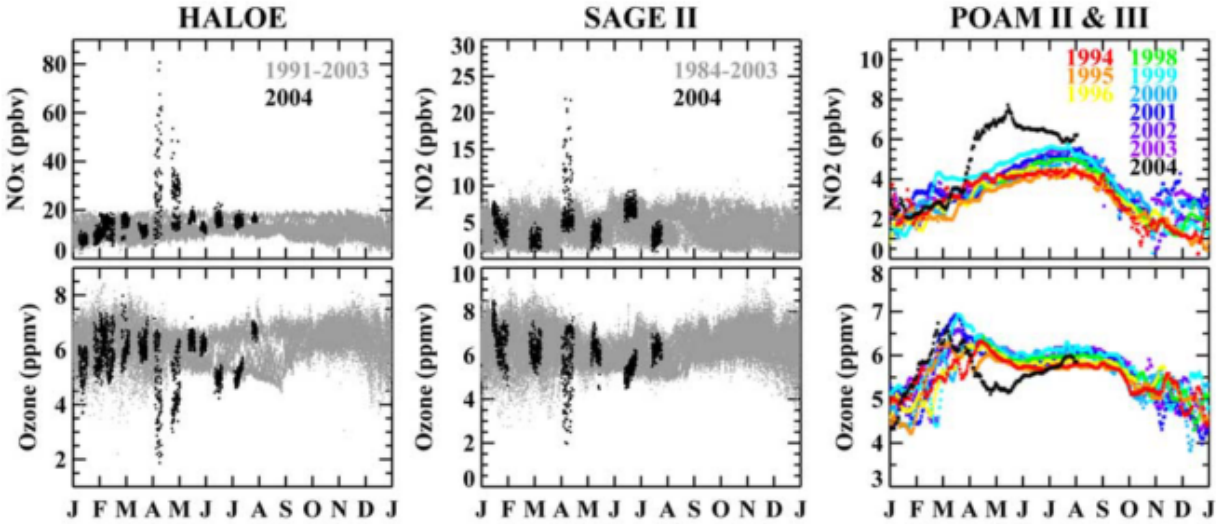

Figure 1.11: Mixing ratios at 40 km for (top left) HALOE NO_x, (top middle) SAGE II NO_2, (top right) POAM NO_2 and (bottom) O_3 for the respective instruments. POAM III NO_2 has been scaled as described by *Randall et al.* [2001]. Tick marks on the horizontal axis denote the first day of each month. Figure 1 from *Randall et al.* [2005].

mid-December 2003 and that the solar conditions in late December 2003 and early January 2004 were characteristic of typical NH winter conditions. They argued that the Halloween Storms were not, in fact, required for the NO_x enhancements observed in the late winter of 2003–2004.

Seppälä et al. [2007b] combined NO_x observations from the GOMOS and POAM III instruments with a radio wave ionization index to provide an assessment of the generation and descent of polar NO_x into the upper stratosphere during the Northern Hemisphere winter of 2003–2004. They looked at the relative contributions of ionization due to SPEs, EEP, and low-energy (1–10 keV) electron precipitation on NO_x production and its subsequent downward transport to the upper stratosphere. They concluded that NO_x generated from the large solar proton storm in October/November 2003 was transported into the upper stratosphere in agreement with model calculations, but that aurorally generated NO_x also descended later in the winter. Both periods were highly significant and produced large long-lived decreases in stratospheric O_3. The observations made by GOMOS in the polar night vortex provided the opportunity to differentiate the stratospheric effects of these two events.

Reporting on the NH winter of 2005–2006, *Randall et al.* [2006] showed that interannual variations in transport are at least as important in controlling the EPP IE in the NH as the level of EPP. Measurements from ACE-FTS showed striking downward motion of NO_x over time beginning in February, and NO_x mixing ratios in February and March 2006 were 3–6 times higher than observed before in either hemisphere, other than in the exceptional winter of 2003–2004. The 2005–2006 NH winter was similar to the 2003–2004 NH winter in terms of dynamics but not in terms of the level of EPP. As in 2003–2004, a major SSW event occurred in January and an exceptionally strong vortex reformed after the warming. SABER and Microwave Limb Sounder (MLS) temperatures showed that the stratopause was elevated to ∼75–78 km as the vortex reformed in the upper stratosphere [*Manney et al.*, 2008; *Siskind et al.*, 2007]. Using tracer correlations, *Randall et al.* [2006] attributed the NO_x transported to the stratosphere in the 2005–2006 NH winter to production of NO_x by

EPP at higher altitudes.

A similar scenario occurred in the 2008–2009 NH winter: *Randall et al.* [2009] reported that ACE-FTS measured NO_x mixing ratios in early 2009 that were up to ∼50% larger than other recent years, excluding 2004 and 2006, even though the level of EPP was low. Once again, a major SSW event occurred in January, and a strong recovery in the upper stratosphere and ES event followed the warming [*Manney et al.*, 2009a]. Figure 1.12 shows ACE-FTS NO_x mixing ratios for the 2003–2004 through 2008–2009 NH winters. The descending NO_x can be seen in February and March of 2004, 2006, and 2009. Again, *Randall et al.* [2009] used tracer correlations to attribute the elevated NO_x to EPP. In addition, they showed that the onset of the ACE-FTS NO_x enhancements coincided with the formation of the ES.

This section has shown that there are numerous satellite instruments that have observed the EPP IE since the beginning of the satellite era. However, as pointed out at the beginning of the section, none of the satellite instruments has measured NO_x continuously in the polar night, throughout the stratosphere and MLT. A further limitation is that our current understanding of the EPP IE is based largely on solar occultation instruments that, by the nature of the measurement technique, do not measure in the polar night. The situation is even more grim considering there is only one satellite instrument currently operating that measures NO_x in the polar regions: ACE-FTS, a solar occultation instrument.

Despite the tools at our disposal being less than ideal, we have made much progress in our understanding of the EPP IE. Some of the most notable discoveries made possible by the available observations are that the EPP IE is highly correlated with auroral activity in the SH but not in the NH, and that even in years of low geomagnetic activity the EPP IE can be substantial in the NH if dynamical conditions are right. These discoveries inspire further interesting questions, such as: is EPP input or dynamics more important in the NH? Another lingering question highlighted by this section is: why did LIMS see the EPP IE so clearly and yet there was a large gap from 1980–1991? These questions are explored in more

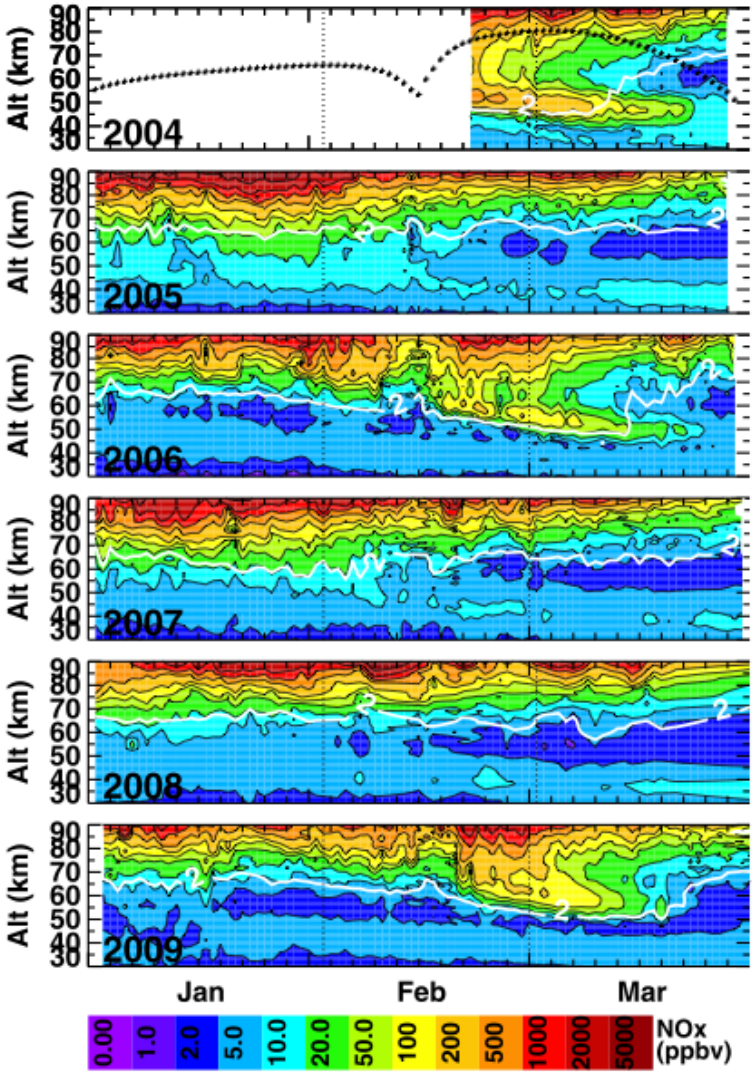

Figure 1.12: Zonal average ACE-FTS NO_x (color) in the NH from 1 January through 31 March of 2004–2009. The white contour denotes CO = 2.0 ppmv; CO increases with increasing altitude. Measurement latitudes (black dots) are shown in the top panel. White regions indicate missing data; vertical black dotted lines denote 1 February and 1 March. ACE-FTS data are unavailable prior to 21 February 2004. Figure 1 from [*Randall et al.*, 2009].

detail in later chapters.

1.8 Modeling Studies of the EPP Indirect Effect

The previous section showed that we have plentiful observational evidence of the EPP IE, but the fact remains that there are no observations of the entire process from beginning to end: transport of EPP-NO_x from its source region to the stratosphere. Therefore modeling studies of the EPP IE are needed to complete the picture. In addition, the impact of EPP-NO_x on O_3 is difficult to quantify with observations. The EPP-NO_x that descends to the stratosphere during winter is redistributed vertically and horizontally and mixed with low-latitude air as the polar vortex breaks down at the end of the winter. Therefore quantifying the impact of EPP-NO_x on O_3 and understanding the contribution of EPP-NO_x to O_3 trends and climate requires global, 3-D models to separate dynamical and chemical effects [*Randall et al.*, 2007]. Models are also indispensable tools for carrying out atmospheric experiments that are fundamentally impossible to carry out in the real atmosphere. For example, we cannot hold the level of EPP constant in the real atmosphere in order to isolate the effects of dynamics on the EPP IE, whereas this experiment it is entirely possible with a model.

Several modeling studies of the EPP IE have been conducted since the EPP IE was first predicted by *Solomon et al.* [1982]. Following *Solomon et al.* [1982] other 2-D modeling studies of the EPP IE were performed [e.g., *Callis et al.*, 1991; *Garcia and Solomon*, 1994; *Siskind et al.*, 1997]. For example, *Siskind et al.* [1997] compared a 2-D chemical transport model with HALOE NO_x observations to study the EPP IE. They found the auroral regions to be the dominant source of downward transported NO. The model also produced larger NO_x enhancements in the SH compared to the NH because of greater descent in the SH. One discrepancy they discussed was that the model overestimated the springtime NO_x enhancements compared to observations. The discrepancy was caused by the later breakup of the polar vortex in the model compared to observations. Unfortunately, this is a problem that persists today in our 3-D general circulation models and is referred to as the cold pole

problem.

In the most recent decade, modeling studies of the EPP IE with state-of-the-art chemistry-climate models have been carried out. 3-D models used in more recent studies include: the Whole Atmosphere Community Climate Model (WACCM), the Chemical Lagrangian Model of the Stratosphere (CLaMS), the KArlsruhe SImulation Model of the middle Atmosphere (KASIMA), the 5th generation European Centre Hamburg general circulation model (ECHAM5) and the Modular Earth Submodel System (MESSy) (ECHAM/MESSy), the Canadian Middle Atmosphere Model (CMAM), and SOlar Climate Ozone Links (SOCOL).

Rozanov et al. [2005] simulated the EPP IE during 1987 with the University of Illinois at Urbana-Champaign chemistry-climate model. The NO_y formation rate used in the simulations, as a function of altitude in each hemisphere, was calculated daily from electron fluxes observed by the Space Environment Monitor aboard the TIROS satellite [*Callis*, 1997] and extended up to 120 km. The additional source of reactive nitrogen was located over the auroral and sub-auroral regions; the source intensity reached its maximum in the lower thermosphere and extended into the mesosphere and upper stratosphere. The simulated NO_y increases exceeded 100 ppbv in the upper mesosphere and 30 ppbv in the lower mesosphere. The simulations also showed intense downward transport during the winter that resulted in NO_y mixing ratios in the polar stratosphere of up to 10 ppbv. In the SH the elevated NO_y mixing ratios were more pronounced and clearly visible even in the lower stratosphere, which was attributed to a higher source function in the SH. They concluded that EPP produces a substantial amount of NO_y in all seasons and leads to O_3 reductions and cooling throughout most of the stratosphere. They also reported stronger polar vortices and small perturbations to the surface air temperature, a result that will be discussed in more detail below.

Vogel et al. [2008] studied the impact of NO_x transported from the mesosphere to the stratosphere in the 2003–2004 NH winter with CLaMS. CLaMS extends to $\sim$50 km in altitude, and the flux of enhanced NO_x is derived from MIPAS observations. Simulations

with and without enhanced NO_x mixing ratios were compared. They found a significant impact on stratospheric O_3 through the spring of 2004: O_3 reductions of up to ∼0.7 ppmv (17%) at ∼1500 K in March 2004 in the run with enhanced NO_x compared to the run without enhanced NO_x. They attributed a column O_3 loss of ∼3% to mesospheric NO_x intrusions into the stratosphere.

Baumgaertner et al. [2009] used ECHAM/MESSy with a parameterization of auroral EPP to study the downward transport of upper atmospheric NO_x produced by low-energy electrons. Because the model top is at 0.01 hPa, the EPP processes that are responsible for NO_x production in the upper atmosphere are not explicitly included in the model. Instead EPP-NO_x is parameterized as a function of the A_p index, based on the correlation between the A_p index and HALOE EPP-NO_x found by *Randall et al.* [2007]. *Baumgaertner et al.* [2009] compared simulations with and without the auroral parameterization for the SH winter of 2003. They found O_3 local reductions of up to 40% following the descent of NO_x to the stratosphere in the simulations including the auroral parameterization. Total column reductions were ∼10%.

Reddmann et al. [2010] compared KASIMA simulations with and without NO_x enhancements and estimated the amount of excess NO_y in the stratosphere from July 2002 to March 2004. KASIMA only reaches up to the upper mesosphere, so EPP effects were included by using MIPAS NO and NO_2 data as an upper boundary condition. They estimated the excess NO_y deposited below 55 km for the 2003 SH winter to be 1.4 Gmol. Their estimate of excess NO_y for the 2002–2003 Arctic winter was 0.4 Gmol, while their estimate for the 2003–2004 Arctic winter was 2.0 Gmol. SH O_3 losses peaked at ∼1.5 ppmv at ∼ 38 km in October 2003, and NH O_3 losses peaked at ∼3 ppmv at ∼40 km in April 2004. The magnitude of O_3 loss is lower in the 2003 SH winter than in the 2003–2004 NH winter, although the SH losses reach lower in altitude.

Semeniuk et al. [2011] investigated the impact of NO_x and HO_x produced by medium- and high-energy auroral electrons, SPEs, and GCRs on the middle atmosphere. CMAM

extends to ∼95 km and does not include NO_x production by low-energy auroral electrons. Ionization rates were derived from observed proton and electron fluxes. They attributed polar stratospheric O_3 reductions of ∼3–10% to the addition of EPP to the model.

Randall et al. [2013, submitted] compared WACCM simulations with high and low auroral EPP. Figure 1.13 shows that substantially more NO_y was produced in the lower thermosphere and descended into the stratosphere during polar winter in both hemispheres in the run with high auroral EPP. NO_y mixing ratios are up to 75% higher in the SH and up to 50% higher in the NH in the high aurora run. Statistically significant decreases in O_3 of up to 12% were seen in the SH from July through December. The effects of the auroral EPP lasted well into the SH spring and even the beginning of summer, which has implications for polar mesospheric clouds. *Randall et al.* [2013] suggest the following coupling mechanism of the EPP IE: as EPP-NO_x descends below 25 km, the excess NO_2 mitigates chlorine-induced O_3 loss in the lower stratosphere by tying up chlorine in $ClONO_2$. This induces a warming of the lower stratosphere of ∼2–4 K near 80°S in December. The warming leads to changes in the zonal-mean wind and filtering of vertically propagating GWs, which leads to a cooling of nearly 10 K in the polar mesosphere in late November and early December. These changes are expected to have a large impact on polar mesospheric clouds. As a caveat, *Randall et al.* [2013] point out that the prolonged SH vortex in WACCM most likely enhances the geoeffectiveness of auroral EPP.

Some studies look at solar cycle variations, that is, the combined EPP and irradiance effects, but not explicitly the EPP effects. *Langematz et al.* [2005] simulated the effects of the 11-year solar cycle by comparing solar min and solar max runs with the Freie Universität Berlin Climate Middle Atmosphere Model with online chemistry. They included the effects of REP by adjusting the NO_x source from 74–84 km by a factor of 2 compared to mean conditions to represent NO_x during solar min and by a factor of 0.5 to represent NO_x during solar max. In the NH winter at 1 hPa (∼60 km), NO_x mixing ratios were ∼ 100 ppbv during solar min and ∼ 20 ppbv during solar max. The percent difference in O_3 poleward of 60 N

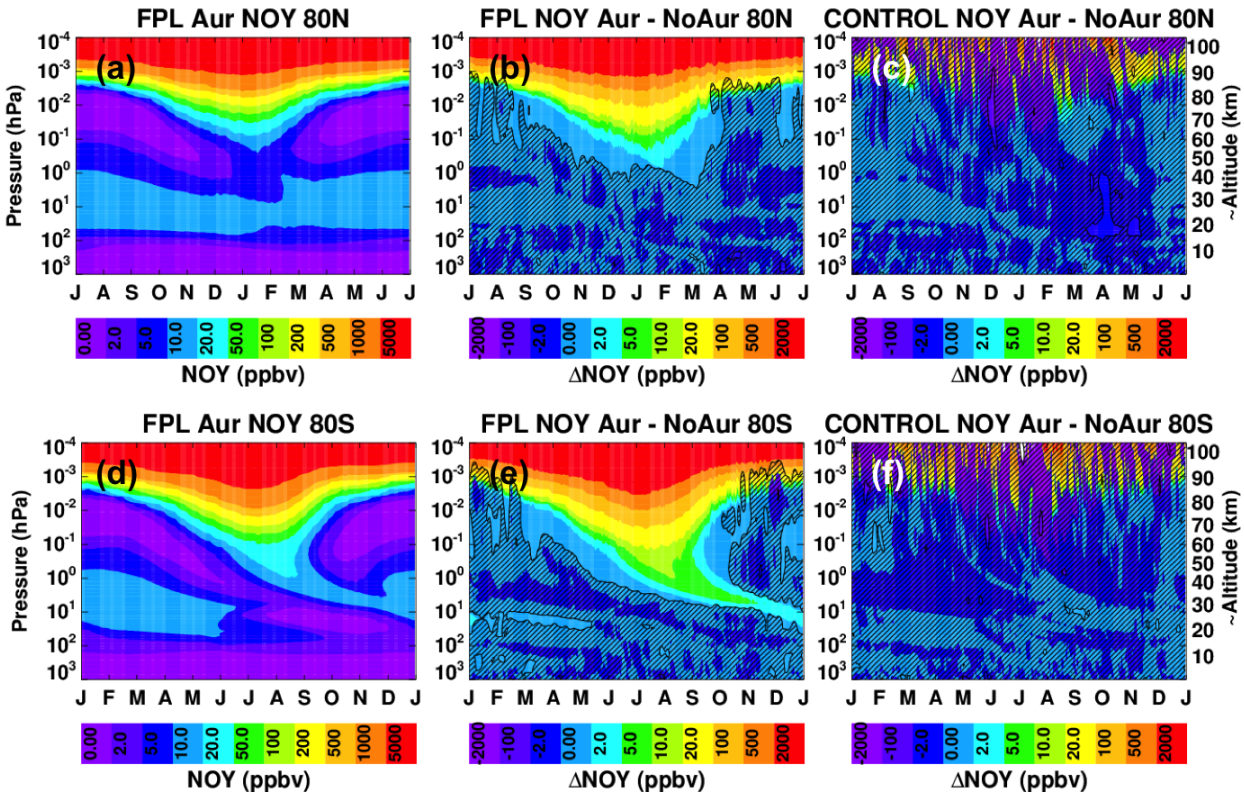

Figure 1.13: Annual evolution of WACCM4 NO_y at 80°N latitude from a high aurora run (a), the difference (ΔNO_y) between this and a low aurora run (b), and ΔNO_y for the control (c). Panels (d)-(f) are the same as (a)-(c), but for 80°S and shifted by 6 months to center the winter season. Unshaded regions bounded by the black contour are statistically significant at the 95% confidence level. Figure 3 from [*Randall et al.*, 2013, submitted].

between solar min and solar max was ∼20%. It should be emphasized that the effects of the EPP IE were not explicitly separated from other solar cycle effects. *Marsh et al.* [2007] used WACCM to model the response of the whole atmosphere up to ∼130 km to variations in radiative and geomagnetic forcing typically seen over the 11-year solar sunspot cycle. They included, for the first time in a general circulation model extending to the surface, a parameterization of auroral processes. They found that EPP IE effects on O_3 were apparent in the polar middle and upper stratosphere. The effects on O_3 and temperature were up to ∼10 times lower than those predicted by *Rozanov et al.* [2005] and *Langematz et al.* [2005]. However, the factor of 2 *Langematz et al.* [2005] used to represent solar max NO_x was most likely an overestimate. Since *Marsh et al.* [2007] studied the effects of the 11-year solar cycle as a whole, they did not explicitly separate the effects of the EPP IE from other solar cycle effects.

Rozanov et al. [2012] compared simulations from 1960–2005 with and without additional NO_x and HO_x sources from GCRs, SPEs, and EEP. They found substantial increases in NO_x and OH in the polar regions accompanied by O_3 depletion and cooling that led to an intensification of the NH polar vortex and warming over Europe. O_3 in the middle stratosphere was up to 8% lower in the climatological mean with EPP. Their results support the idea that EPP affects chemical composition, dynamics, and ultimately climate.

It has recently been suggested that changes in mesospheric–stratospheric NO_x and O_3 concentrations could modulate polar surface air temperatures by affecting the radiative budget and therefore atmospheric circulation patterns [*Seppälä et al.*, 2009; *Baumgaertner et al.*, 2011]. *Seppälä et al.* [2009] looked at how ECMWF and ERA-40 polar surface air temperatures from 1957 to 2006 varied for years with high geomagnetic activity compared to years with low geomagnetic activity. The response was similar to the modeled response reported by *Rozanov et al.* [2005]. Figure 1.14 shows the difference in surface temperatures between years with a high A_p index and years with a low A_p index. However, the patterns are also similar to the Northern Annular Mode (NAM), imparting a high level of uncertainty to

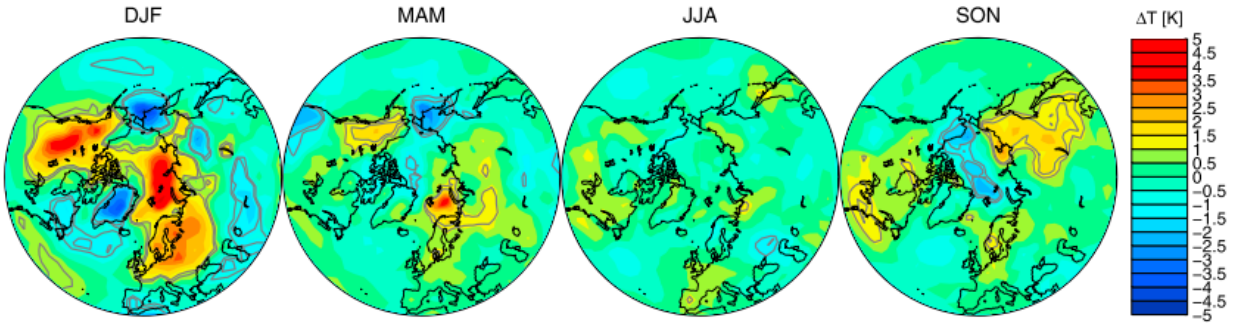

Figure 1.14: NH seasonal differences in surface temperature (ΔT = high A_p - low A_p). Years with major SSW events are not included. Figure 5 from [*Seppälä et al.*, 2009].

the cause of the surface temperature changes. To study the possible surface effects of the EPP IE in a model, *Baumgaertner et al.* [2011] simulated the same years that *Seppälä et al.* [2009] analyzed with ECHAM/MESSy. Their results supported the findings of *Seppälä et al.* [2009]. To control for the effects of the EPP IE, *Baumgaertner et al.* [2011] compared two additional nine-year simulations with identical boundary conditions other than geomagnetic activity. Similar patters were observed in the nine-year simulations. They found that the EPP IE led to changes in O_3 and the radiative budget in the stratosphere. These changes cooled the lower stratosphere and strengthened the polar vortex. They speculated that enhanced geomagnetic activity triggers positive NAM phases at the surface. Opposing results were found by *Lu et al.* [2008]. They performed statistical analyses of satellite observations and meteorological reanalysis data and found that spring A_p signals were inconsistent with a simple local cooling effect from EPP-NO_x. In any case, the hypothesis that the EPP IE affects surface temperatures remains highly controversial.

Chapter 2

Atmospheric Effects of Energetic Particle Precipitation in the Arctic winter 1978–1979 Revisited

This chapter includes *Holt et al.* [2012][1] and some extended results with MIPAS data that has become available since. *Holt et al.* [2012] compared recently reprocessed LIMS data to more recent measurements from MIPAS and ACE-FTS to place the LIMS measurements in the context of current observations. LIMS measured polar stratospheric enhancements of NO_2 mixing ratios due to EPP in the Arctic winter of 1978–1979. Additionally, *Holt et al.* [2012] presents a method to quantify the EPP IE when no tracer measurements are available. With this method they quantified the amount of EPP-NO_x entering the stratosphere for the 1978–1979 and 2002–2003 through 2008–2009 Arctic winters.

The main findings of *Holt et al.* [2012] are: (1) the NO_2 enhancements in the LIMS data are similar to those in MIPAS and ACE-FTS data in the Arctic winters of 2002–2003, 2004–2005, 2006–2007, and 2007–2008; (2) the largest enhancement by far is in 2003–2004 ($\sim$2.2 Gmol at 1500 K), which is attributed to a combination of elevated EPP and unusual dynamics that led to strong descent in the upper stratosphere/lower mesosphere in late winter; (3) the enhancements in 2005–2006 and 2008–2009, during which large stratospheric NO_x enhancements were caused by a dynamical situation similar to that in 2003–2004, are larger than in all the other years (except 2003–2004) at 3000 K. However, by 2000 K the enhancements in 2005–2006 and 2008–2009 are on the same order of magnitude as or smaller

[1] Reproduced with permission from the American Geophysical Union

than all other years. These results highlight the importance of the timing of the descent in determining the potential of EPP-NO_x for reaching the middle stratosphere.

2.1 Introduction

The key catalytic cycle responsible for ozone loss in the stratosphere between about 25 and 40 km is the NO_x (NO + NO_2) catalytic cycle [e.g., *Crutzen*, 1970; *Garcia and Solomon*, 1994; *Watson et al.*, 1986]. The primary source of NO_x in the stratosphere is NO produced from the oxidation of N_2O of tropospheric origin [e.g., *Bates and Hays*, 1967; *Crutzen*, 1971; *McElroy and McConnell*, 1971; *Nicolet*, 1971]. Another source of stratospheric NO_x is NO produced by energetic particle precipitation (EPP). EPP ionizes the atmosphere, resulting in formation of NO at an altitude dependent upon the energy of the precipitating particles [e.g., *Crutzen et al.*, 1975; *Gylvan Meira*, 1971; *Narcisi et al.*, 1972; *Rusch et al.*, 1981]. The NO_x so produced is referred to as EPP-NO_x.

NO in the polar winter thermosphere above 100 km is produced mainly from routine precipitation of low-energy (auroral) electrons (energy $<$ 30 keV) and protons (energy $<$ 1 MeV) and subsequent reaction of excited N(^{2}D) and O_2 [*Thorne*, 1980]. Regular precipitation of medium energy electrons (30–300 keV) results in NO production at mesospheric altitudes [*Codrescu et al.*, 1997]. NO is rapidly photodissociated in the sunlit mesosphere and thermosphere, but in the polar night region can be transported to the stratosphere. Once NO reaches the lower mesosphere, where O3 concentrations become significant, it can react with O3 to produce NO_2 [e.g., *Cohen and Murphy*, 2003]. The process by which NO_x created in the upper atmosphere is transported to the stratosphere is called the EPP indirect effect (EPP IE), and was predicted by *Solomon et al.* [1982] using a 2-D model. Satellite evidence of this phenomenon was first obtained from the Limb Infrared Monitor of the Stratosphere (LIMS) during the Northern Hemisphere (NH) winter of 1978–1979 [*Russell et al.*, 1984]. It has since been observed a number of times, along with evidence for the destruction of O_3 by EPP-NO_x [e.g., *Callis et al.*, 1996, 1998a,b; *Callis and Lambeth*, 1998; *Funke et al.*, 2005a;

López-Puertas et al., 2005a; *Randall et al.*, 1998, 2001, 2005, 2007, 2009; *Rinsland et al.*, 1996, 1999; *Seppälä et al.*, 2007a]. NO is also produced in situ when high-energy electrons (E > 300 keV) and protons (E > 30 MeV) deposit their energy in the stratosphere, but this happens sporadically during periods of strong geomagnetic activity.

Measurements of SH NO_x and tracers show that variations in the amount of EPP-NO_x descending to the SH stratosphere depend mainly on the level of geomagnetic activity. That is, the interannual variability of SH stratospheric NO_x correlates well with the A_p index and auroral and medium energy electron hemispheric power. For example, *Randall et al.* [2007] documented this correlation using data from solar occultation instruments, and showed that in years with high geomagnetic activity the SH EPP IE contributed up to 40% of the annual source of polar stratospheric NO_x. That the correlation was so strong was attributed in part to the fact that variability in SH dynamics is small, and thus has little effect on interannual variations in the amount of EPP-NO_x transported downward to the stratosphere. However, the same correlation between the A_p index or energetic particle hemispheric power and the EPP IE is not found in the NH. This hemispherical discrepancy has been substantiated by NO_x measurements from the Halogen Occultation Experiment (HALOE) and attributed to dynamical variability in the NH through a 2-D chemical transport model [*Siskind et al.*, 1997]. Using data from the Global Ozone Monitoring by Occultation of Stars (GOMOS) instrument, *Seppälä et al.* [2007a] found that NH stratospheric EPP-NO_x enhancements from 46 to 56 km correlated well with the A_p index from 2002 to 2003 through 2005–2006, but these calculations included only the months of October through January.

A salient discovery in recent years is that even in periods of minimal geomagnetic activity enhancements in stratospheric NO_x mixing ratios due to the EPP IE can be as large as in years with high geomagnetic activity. This was first illustrated in the NH winter of 2005–2006. Although geomagnetic activity was low, observations showed large enhancements of EPP-NO_x in the stratosphere [*Randall et al.*, 2006; *Siskind et al.*, 2007]. A similar scenario was observed again in 2009 when EPP-NO_x enhancements in the uppermost stratosphere

were up to 50 times higher than average in spite of low geomagnetic activity [*Randall et al.*, 2009]. These enhancements were attributed to unusual dynamical conditions caused by a remarkable recovery from a major sudden stratospheric warming (SSW). This recovery resulted in strong descent in the mesosphere and upper stratosphere, as indicated by an elevated stratopause, and a strong upper stratospheric vortex that sequestered air in the polar region. The precise phenomena that trigger these unusual conditions are not yet understood. Once initiated, however, the reversal of the zonal winds during the SSW prevents the upward propagation of planetary waves, which allows the vortex to reform with strong westerly winds that favor the propagation of gravity waves. Gravity waves then act to decelerate the westerly flow, which creates a poleward meridional flow leading to enhanced downward motion at the winter pole [e.g., *Hauchecorne et al.*, 2007].

Following the LIMS measurements in 1978–1979 until the launch of the Upper Atmosphere Research Satellite (UARS) in 1991, there were few reports of stratospheric EPP-NO_x enhancements; it is not known, however, if this is due to the fact that such enhancements did not occur, or to the lack of appropriate data in the polar winter. This raises the question of why the EPP-NO_x enhancements were seen so clearly in the LIMS data: Were they observed because enhanced EPP or unusual meteorology led to higher-than-normal stratospheric NO_x mixing ratio enhancements, as in 2004, 2006, and 2009? Or were the mixing ratio enhancements typical for NH winters, but easily observed because of the capability of LIMS to view the polar night? In this study, we compare the EPP-NO_x enhancements in the LIMS data to more recent satellite data from the Michelson Interferometer for Passive Atmospheric Sounding (MIPAS) and Atmospheric Chemistry Experiment Fourier transform spectrometer (ACE-FTS) to determine whether the LIMS enhancements are unusual in the context of current observations. We quantify the amount of EPP-NO_x entering the stratosphere in the 1978–1979 Arctic winter and in the winters observed by MIPAS and ACE-FTS.

This chapter is structured as follows. Section 2.2 gives a review of the satellite observations that we use. In section 2.3 we compare the temporal evolution of NO_x between the

different instruments. We then discuss the dynamics and geomagnetic activity for each of the years. In section 2.4 we quantify the amount of EPP-NO_x descending past the 1500 K, 2000 K, and 3000 K isentropic surfaces. Section 2.5 includes the summary and conclusions.

2.2 Data

2.2.1 LIMS

LIMS was a thermal infrared limb scanning radiometer with six channels between 6.2 and 15.0 microns [*Gille and Russell*, 1984]. It measured vertical radiance profiles from which temperature, water vapor (H_2O), O_3, NO_2 and nitric acid (HNO_3) were retrieved. LIMS was launched on the NIMBUS 7 spacecraft into a near polar, Sun-synchronous orbit with an inclination of 99.1° and an altitude of 955 km on 24 October 1978, and operated until 28 May 1979. It collected data day and night with near global coverage from 64°S to 84°N every 6 days, returning more than 7000 radiance profiles each day. The current study utilizes level 2 of the reprocessed or Version 6 (V6) LIMS data set [*Remsberg et al.*, 2004, 2010]. The vertical resolution of the V6 NO_2 is aproximately 3.7 km and the nighttime NO_2 mixing ratios extend from approximately 50 hPa to the lower mesosphere, at least in the polar night. The precision of the updated V6 NO_2 is approximately 3% from 3 to 10 hPa, 7% at 30 hPa and 14% (30%) at 1 hPa, and the accuracy is approximately 18% from 3 to 10 hPa, 30% at 30 hPa and 30% at 1 hPa [*Remsberg et al.*, 2010]. The accuracy of LIMS V6 NO_2 in the upper stratosphere is better than the previous versions because of improved spectral line parameters for the NO_2 forward radiance model.

2.2.2 MIPAS

The Michelson Interferometer for Passive Atmospheric Coupling (MIPAS) measured NO_2 and NO in the polar night stratosphere, and is thus well suited for comparing to the LIMS measurements. MIPAS is a high-resolution Fourier transform spectrometer operating

in the midinfrared (685–2410 cm^{-1}) aboard the Environmental Satellite (ENVISAT), which was launched into a Sun-synchronous orbit with an inclination of 98.55° and an altitude of 800 km on 1 March 2002 [*Fischer et al.*, 2008]. It is a limb emission instrument that collects data day and night with global coverage, and returns up to 72 scans in each of its daily 14.3 orbits. MIPAS has a vertical resolution of 3 km in the altitude range of 6–68 km. Reprocessed version 4.61/4.62 of the operational European Space Agency (ESA) NO_2 data was used here for comparison to LIMS. *Wetzel et al.* [2007] reported an overall accuracy of approximately 10%–20% and a precision of around 5%–15% for version 4.61 MIPAS NO_2 below about 45 km. They compared MIPAS NO_2 to observations from balloons, satellites, and ground-based measurements. In addition to NO_2, we used ESA CH_4 [e.g., *Raspollini et al.*, 2006] as a tracer of vertical motion. We have also used a special scientific version of the MIPAS data from the Institute for Meteorology and Climate Research/Instituto de Astrofísica de Andalucía (IMK/IAA) (MIPAS-IMK/IAA) [*Funke et al.*, 2005b; *von Clarmann et al.*, 2003]. MIPAS-IMK/IAA has both NO and NO_2. MIPAS-IMK/IAA NO_2 and NO data were compared to ACE-FTS data [*Kerzenmacher et al.*, 2008], resulting in typical differences for NO of 20% in the range 42–60 km, 10% in the range 15–42 km, and 20% for NO_2 in the range 28–44 km.

Results from the MIPAS instrument have been detailed in several papers to date, many of which include studies of the EPP IE. A handful of the most relevant are outlined here. *López-Puertas et al.* [2005a] looked at MIPAS data to study the stratospheric NO_x enhancements and subsequent O_3 depletion in the polar regions resulting from solar proton events (SPEs) during the solar storms in October and November of 2003. *Funke et al.* [2005a] used MIPAS data to quantify the amount of EPP-NO_x transported to the polar stratosphere in the 2003 Antarctic winter. In their study they used CH_4 and CO as dynamical tracers to determine the origin of the NO_x-enhanced air. *Stiller et al.* [2005] looked at vertical profiles of stratospheric HNO_3 from MIPAS. They reported a second maximum in HNO_3 at approximately 34 km, which they attributed to ion cluster chemistry and/or heterogeneous chemistry made possible by N_2O_5 produced by a large EPP IE between May and August

2003. *López-Puertas et al.* [2006] investigated stratospheric and mesospheric NO_y in the polar winters of both hemispheres from 2002 to 2004. They found very high interannual as well as interhemispheric variability, which they examined in terms of dynamics and solar activity.

2.2.3 ACE-FTS

ACE-FTS is a 0.02 cm^{-1} resolution Fourier transform spectrometer operating in the midinfrared (750–4400 cm^{-1}) aboard SCISAT-1, which was launched into a circular low Earth orbit with an inclination of 74° and an altitude of 650 km on 12 August 2003 [*Bernath et al.*, 2005]. Using solar occultation it measures over 20 atmospheric constituents, including NO, NO_2 and CH_4, in two latitude circles (at satellite sunrise and sunset) between 85°S and 85°N each day. Since it is a solar occultation instrument, it does not take measurements in the polar night. Version 2.2 of the ACE-FTS data was used in this study [*Boone et al.*, 2005].

Initial validation of ACE-FTS NO_x by *McHugh et al.* [2005] showed agreement of ACE-FTS NO_x with the Halogen Occultation Experiment (HALOE) to within 20% between 22 and 55 km. They also showed that ACE-FTS CH_4 was about 10% higher than HALOE throughout the stratosphere. *Kar et al.* [2007] showed that ACE-FTS NO_2 agrees with the Measurements of Aerosol Extinction in the Stratosphere and Troposphere Retrieved by Occultation (MAESTRO) instrument, also aboard SCISAT-1, to within approximately 10%-15% from 15 to 40 km for sunrise measurements and from 22 to 35 km for sunset measurements. *Kerzenmacher et al.* [2008] compared ACE-FTS version 2.2 NO and NO_2 to several satellite, balloon-borne, and ground-based measurements. They found agreement of ACE-FTS NO_2 with other satellite data sets to within about 20% between 25 and 40 km. ACE-FTS NO agreed with HALOE mixing ratios to within 8% from 22 to 64 km. *de Mazière et al.* [2008] compared ACE-FTS CH_4 to correlative satellite, balloon-borne, and ground-based Fourier transform infrared remote sensing data and concluded that the

accuracy of ACE-FTS CH_4 is within 25% throughout the stratosphere.

2.3 NO_x Evolution in LIMS, MIPAS and ACE

Figure 2.1 shows LIMS NO_2 from the 1978–1979 Arctic winter compared to MIPAS NO_2 from the 2002–2003 and 2003–2004 Arctic winters. Each image shows nighttime (solar zenith angle $> 90°$) NO_2 mixing ratios averaged inside the vortex from 1 November to 31 March. To determine the extent of the polar vortex, we used the method described by *Harvey et al.* [2002]; meteorological parameters were taken from the 40 year ECMWF reanalysis (ERA-40) data set [*Uppala et al.*, 2005] and the Met Office (MetO) Unified Model [*Swinbank and O'Neill*, 1994]. Using this method, we were only able to determine the vortex edge up to approximately 2000 K. Above 2000 K, we have assumed that the vortex edge is the value at 2000 K. The data is smoothed in time with a 3 day running average. NO at LIMS measurement altitudes is quickly converted to NO_2 after sunset. During the night NO_2 begins to decrease, however, as it reacts with O_3 to form NO_3, which then reacts with another NO_2 molecule to form N_2O_5 [e.g., *Brasseur and Solomon*, 2005]. We use nighttime NO_2 as a reasonable approximation for NO_x with the caveat that it is most likely an underestimate since some of the NO_2 will have been converted to N_2O_5 during the night. LIMS measurements (Figure 2.1a) clearly show NO_2 descending with time in the polar stratosphere. The temporal behavior of NO_2 is emphasized with the black contour line, which shows the 8 ppbv mixing ratio contour descending with time. Since the only source of NO_x in the mesosphere during the polar winter is EPP, these high NO_2 mixing ratios are unambiguously identified as being caused by EPP. NO_2 mixing ratios reached a maximum of 18 ppbv in the upper stratosphere near 2600 K ($\sim$52 km) at the end of January. Upper atmosphere EPP-NO_x had already descended to 3000 K by at least mid-November and reached 1500 K by the beginning of February. According to *Dunkerton* [1991], a pair of minor warmings took place on 26 January and 8 February; this might explain the rapid decrease in NO_2 mixing ratios above 1500 K near 1 February and again about a week later.

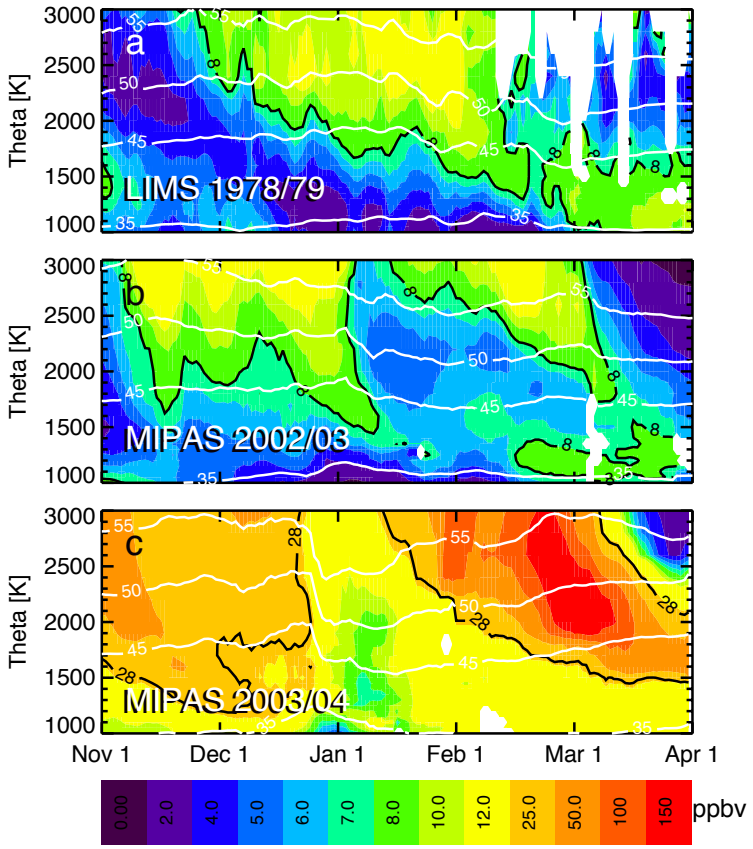

Figure 2.1: Nighttime NO_2 averaged in the vortex for (a) LIMS in 1978–1979, (b) MIPAS in 2002–2003, and (c) MIPAS in 2003–2004. White regions indicate missing data. White lines indicate altitude in kilometers. Black contour lines at 8 and 28 ppbv are shown to highlight the descent of NO_2 over time.

Because of missing data, it is difficult to say what happened to the NO_2 above 2000 K after 8 February, but there is little indication of further descent or substantially enhanced NO_x at these altitudes. A major SSW occurred around 23 February; it was caused by the propagation of a planetary wave 2 of exceptional strength from the troposphere into the stratosphere, which occurred two weeks after the amplification of wave 1 [*Labitzke*, 1981]. At this time mixing with extra-vortex polar air caused NO_2 mixing ratios near 1500 K to decrease slightly. After the vortex recovered, however, NO_2 descent continues into March, reaching below 1000 K by the end of March. Some of the increase in NO_2 mixing ratios in March below 1500 K can be attributed to the conversion of reservoir species back into NO_2 as sunlight returns to the polar region.

The MIPAS data in the Artic winter of 2002–2003 (Figure 2.1b) also shows the downward transport of NO_2 into the stratosphere, and has been discussed in detail by *Funke et al.* [2005a]. Again the temporal evolution is emphasized by the black contour line. Elevated NO_2 mixing ratios appeared below 3000 K by 1 November and reached the 1500 K level at the end of December; descent from above was abruptly cut short by a major SSW at the beginning of January. Mixing ratios reached a maximum of 26 ppbv on 18 November in the upper stratosphere (3000 K). Note that the occurrence of this midwinter SSW is a major difference between the winters of 2002–2003 and 1978–1979, but is not unusual for NH winters. Using CH_4 as a tracer, *Funke et al.* [2005a] showed that the increase in NO_2 around 1500 K after 1 February was due to mixing of extra-vortex mid-latitude air. Downward transport of NO_2 continued again after the major SSW, but *Funke et al.* [2005a] point out that it was confined to the upper stratosphere since the vortex below 2000 K did not regain strength following the warming. Overall, meteorology during the 2002–2003 Arctic winter was typical of NH winters prior to 2004, and EPP levels were near average.

In the 2003–2004 Arctic winter, the MIPAS NO_2 (Figure 2.1c) shows two distinct enhancements in stratospheric NO_2. The first took place in November and December, and has been attributed to in situ production from the exceptional SPEs that occurred in October and

November as well as downward transport following the events [*López-Puertas et al.*, 2005a]. The high NO_2 mixing ratios were affected by a major SSW in late December. At this time, the downward transport was interrupted, and the NO_2-rich air in the vortex was diluted by mixing with air from lower latitudes; this explains the low mixing ratios that separate the two periods of enhanced NO_2. Following the major SSW, the vortex rapidly recovered in the upper stratosphere to become the strongest on record in February and March [*Manney et al.*, 2005]. The second enhancement was first observed by MIPAS in early January, and descended to 1500 K by mid-March; maximum NO_2 mixing ratios exceeded those observed by LIMS in 1978–1979 and MIPAS in 2002–2003 by a factor of 20 and 14, respectively, in the upper stratosphere. Because of operational problems, MIPAS data are not available in 2004 after late March. Analyses of other data sets, however, show that the EPP-NO_x enhancements observed in March–April 2004 exceeded 600 ppbv at 48 km [*Randall et al.*, 2006], and were the largest on record for both hemispheres [*Randall et al.*, 2005; *Rinsland et al.*, 2005]. Moderately elevated EPP levels as well as peculiar dynamical conditions played a large role in the enhancements seen in 2004 [*Clilverd et al.*, 2006; *Hauchecorne et al.*, 2007; *Jin et al.*, 2005; *Natarajan et al.*, 2004; *Randall et al.*, 2005; *Rinsland et al.*, 2005].

The stratospheric NO_2 enhancements in the LIMS data are similar in magnitude to those in the MIPAS data during the Arctic winter of 2002–2003, but much smaller than in MIPAS during 2003–2004. The primary differences between LIMS and MIPAS in 2002–2003 can largely be attributed to the different timing of the NO_2 descent in each winter. On the other hand, the differences between LIMS and MIPAS in 2003–2004, which indicate that MIPAS NO_2 was up to 50 times larger than LIMS NO_2, arise because of the unusually high levels of particle activity and extraordinary meteorology of the 2003–2004 winter. Neither exceptional EPP levels nor exceptional meteorological conditions were present in 1978–1979, as described more below.

2.3.1 LIMS Nighttime NO_2 versus ACE-FTS NO_x

Figure 2.2 compares the nighttime LIMS NO_2 mixing ratios in the vortex to NO_x mixing ratios from ACE-FTS. Panel (b) is the average of 2006 and 2009 ACE-FTS NO_x mixing ratios for January through March. Panel (c) is the average of 2005, 2007 and 2008 ACE-FTS NO_x mixing ratios for January through March. The average of 2006 and 2009 represents those years in which extraordinary EPP-NO_x enhancements have been observed under conditions of low EPP [*Randall et al.*, 2006, 2009]. We chose to exclude ACE-FTS NO_x in 2004 from the average since there is no data for January and part of February 2004. The measurement latitudes of ACE-FTS are shown under the three panels. ACE-FTS NO_x mixing ratios in 2006 and 2009 exceed 150 ppbv in the upper stratosphere in February and March. Mixing ratios reach maxima of 30 ppbv, 20 ppbv, and 14 ppbv in 2005, 2007, and 2008, respectively, around 2500–3000 K (∼55–60 km) in January. The average of the maximum mixing ratios for these three years is about 21.3 ppbv, which is similar to the maximum LIMS mixing ratios for 1979 of 18 ppbv. In 2006 and 2009, unusual dynamics were observed; however, the level of geomagnetic activity was low in these years. The LIMS NO_2 much more closely resembles ACE-FTS NO_x in 2005, 2007 and 2008, and MIPAS data for 2002–2003. Interestingly, the primary EPP-induced NO_x enhancements in both 2006 and 2009 occurred in February-March, significantly later than the primary NO_x enhancements in 2005, 2007, and 2008 or in 1979. Since ACE-FTS samples latitudes equatorward of 65 N during January to mid February, the observed differences in this period between the years 2006 and 2009 and years 2005, 2007, and 2008 might be related to different vortex extensions and do not necessarily imply stronger mesospheric mid-winter NO_x intrusions during the latter years. In support of this speculation, MIPAS averages poleward of 60 N do not show such pronounced mid-winter differences in NO_x.

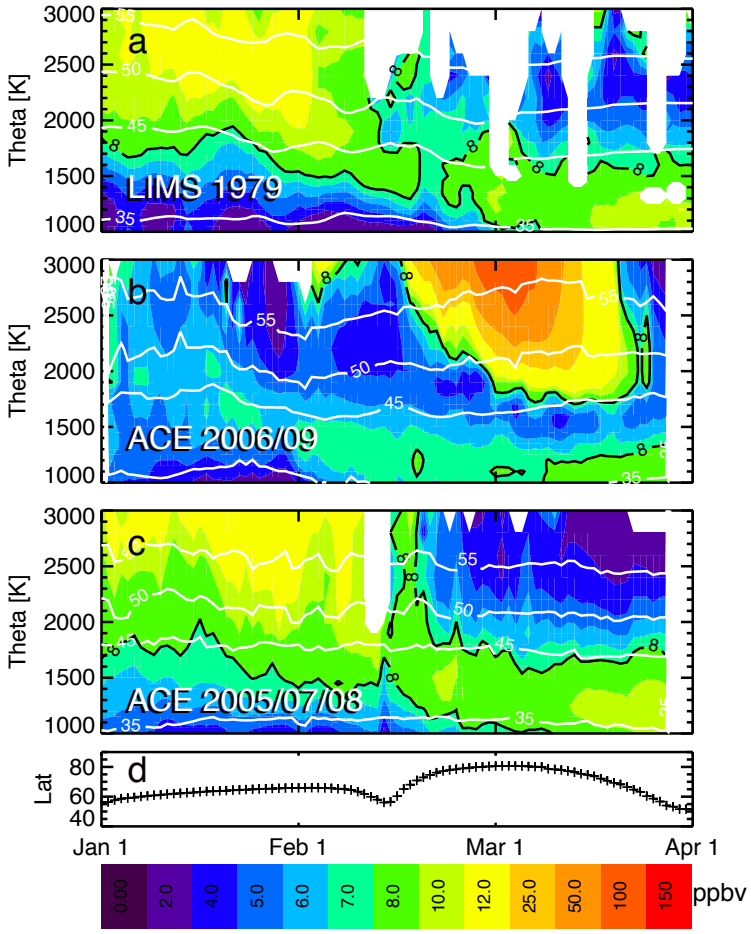

Figure 2.2: (a) Nighttime LIMS NO_2 in the vortex in 1979. (b) The average of ACE-FTS NO_x in 2006 and 2009. (c) The average of ACE-FTS NO_x in 2005, 2007, and 2008. (d) ACE-FTS measurement latitudes. White regions indicate missing data. Black contour lines at 8 ppbv are shown to highlight the descent of NO_2 over time.

2.3.2 LIMS Temperature versus SABER Temperature

One of the signatures of the unusual meteorology that led to the large NO_x enhancements in 2004, 2006 and 2009 is a strongly elevated stratopause height, which is indicative of enhanced adiabatic descent causing warming at altitudes that are normally in the mesosphere [*Hauchecorne et al.*, 2007; *Siskind et al.*, 2007]. *Manney et al.* [2008] pointed out that during the vortex break-up in early 2004 the stratopause was virtually isothermal; and upon recovery of the vortex a cool stratopause reformed above 75 km, which is much higher than the typical winter stratopause height of 50 km. They also found that in 2006 both the evolution of the SSW and the vortex recovery were very similar to those in 2004. An exceptionally strong and protracted SSW took place in January 2006, followed by the rapid recovery in early February of the upper stratospheric vortex and formation of an elevated stratopause around 80 km. In 2009, the strongest and most prolonged SSW on record took place in January [*Manney et al.*, 2009a]. As in 2004 and 2006, a strong upper stratospheric vortex reformed following the warming and the stratopause reformed around 80 km.

Figure 2.3 shows that an elevated stratopause was not present in 1979. The stratopause heights are derived from LIMS (1979) and the Sounding of the Atmosphere using Broadband Radiometry (SABER) instrument (2003–2009) zonal mean temperature averaged from 75–80 N from 10 January to 12 March. The stratopause reforms at an altitude of 80 km after major SSW events in 2004, 2006 and 2009 (in 2004 the SSW itself was not observed by SABER because it was viewing in the opposite hemisphere at that time). The temperature of the 80-km stratopause is between 230 and 240 K in these three years, which is much cooler than typical winter stratopause temperatures. In contrast, in 1979, 2005, 2007 and 2008 the stratopause height remains around 50 km throughout most of the season, with temperatures between 250 and 260 K; occasional dips of the stratopause height are caused by major or minor warmings in these years, but an elevated stratopause is never present. The other dynamical feature of note, a strong vortex that reformed after the major SSWs

in 2004, 2006, and 2009, was also absent in 1979. Although the conditions for a major SSW were met on 23 February 1979 [*Labitzke*, 1981], a strong vortex did not reform in the upper stratosphere.

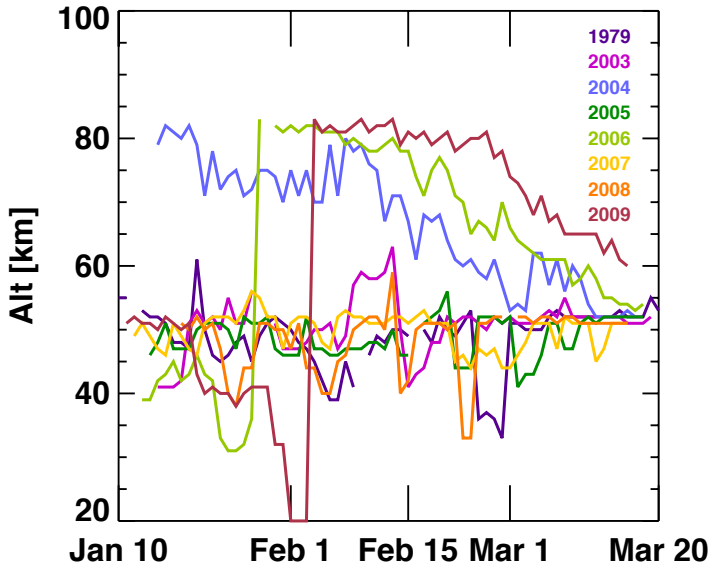

Figure 2.3: Zonal mean LIMS and SABER stratopause heights from 10 January to 20 March, averaged from 75°N to 80°N. Breaks in the lines indicate missing data.

2.3.3 Geomagnetic Activity During LIMS Observing Period

Figure 2.4 shows the geomagnetic A_p index from 1 November 1978 through 31 March 1979. The level of geomagnetic activity was not unusual during the 1978–1979 Arctic winter. The average of the A_p index for this time period was 15.8, whereas the average of the entire record from 1932-2009 was 14.3. There were also no significant solar proton events during the Arctic winter of 1978–1979. Using a two-dimensional model, *Jackman and Meade* [1988] investigated a solar proton event (SPE) that occurred in September 1978 to determine whether the SPE could have accounted for the elevated NO_2 mixing ratios in the LIMS NO_2. They found that an increase in excess of 20 ppbv of NO_2 above 1 mbar following the SPE diminished to only a few ppbv by 1 December 1978. They concluded that the SPE did not

significantly contribute to the LIMS NO_2 measurements in the polar night. In addition, they reported that no significant SPEs took place during the time that LIMS operated. That the geomagnetic A_p index was average during the 1979 Arctic winter indicates that the LIMS EPP-NO_x enhancements cannot be attributed to unusually high EPP levels.

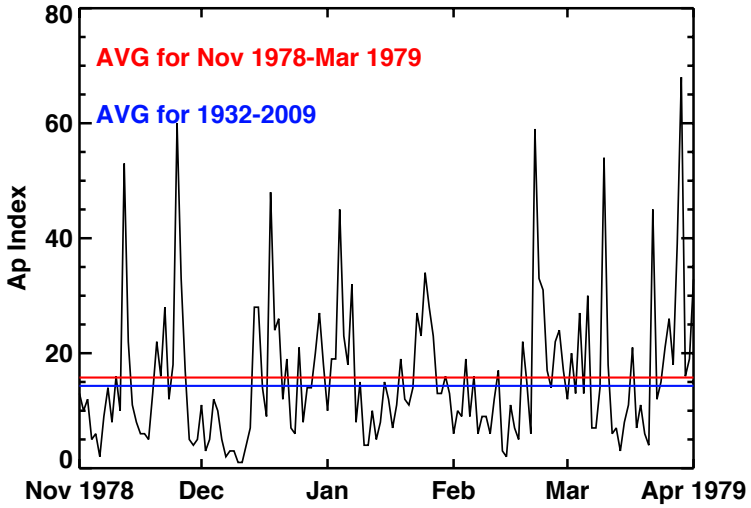

Figure 2.4: Geomagnetic A_p index from 1 November 1978 through 31 March 1979. The average of the A_p index from 1 November 1978 through 31 March 1979 is 15.8 (red line), whereas the average of the A_p index for the entire record from 1932 to 2009 is 14.3 (blue line).

2.4 Quantification of EPP-NO_x in LIMS, MIPAS and ACE-FTS

2.4.1 LIMS and MIPAS EPP-NO_x

In this section we describe the method used to quantify the absolute amount of EPP-NO_x in the LIMS data, and compare this estimate with values for other years. Due to the absence of a tracer species in the LIMS data, we were unable to directly correlate the high NO_2 mixing ratios with the descent of air from above as in previous studies [e.g., *Funke et al.*, 2005a; *Randall et al.*, 2007; *Siskind and Russell*, 1996; *Siskind et al.*, 1997]. Nevertheless, with observations in the polar night throughout the winter, we can directly infer the amount

of descending EPP-NO_x. This requires the assumption, however, that the increase in NO_2 in the polar stratospheric vortex is entirely due to the EPP IE.

We estimated the amount of EPP-NO_x that crossed the 1500 K, 2000 K and 3000 K potential temperature surfaces over the entire season. This is consistent with the method used by *Randall et al.* [2007] to estimate the amount of EPP-NO_x entering the SH stratosphere from 1992 to 2005. Whereas *Randall et al.* [2007] used only the 2000 K surface, we performed the calculation at additional levels because, unlike the SH, the NH is highly variable and the 2000 K surface does not necessarily provide a comprehensive picture. Note that the subtraction method is not valid below 1500 K because of difficulties tracing excess NO_x to upper atmospheric origin. As above, we have used nighttime NO_2 as a proxy for NO_x. Our method assumes that NO_2 has not yet been converted to reservoir gases nor has it been lost by photochemical destruction. Also, we include only data inside the vortex in our calculations. These assumptions lead to an underestimate in the results reported below, although this might be at least partially balanced by the assumption that all increases in vortex NO_2 are due to the EPP IE. For each day on each isentropic surface the average NO_2 density inside the vortex minus the amount in the vortex before the enhancement was multiplied by the area enclosed by the vortex. This calculation produces the excess number of NO_2 molecules on each isentropic surface, which was multiplied by the descent rate to arrive at the number of molecules crossing the isentropic surface per day as a function of time. The flux of molecules across each isentropic surface as a function of time was summed over the entire winter to obtain the total number of molecules crossing each level. Henceforth, we will refer to this method as the subtraction method; results are presented below in units of gigamoles (Gmol). We tested our method by applying it at 2000 K to MIPAS data for the 2002–2003 Arctic winter, the 2003 Antarctic winter and the 2003–2004 Arctic winter and comparing our results to the results obtained using CH_4 as a tracer and to previous studies.

Figure 2.5 shows scatter plots of MIPAS nighttime NO_2 versus CH_4 at 2000 K for each of the three winters. Measurements at all latitudes for the pertinent winter hemisphere

are included in each panel. In the winter upper stratosphere NO_x and CH_4 are generally positively correlated, with the lowest values of CH_4 indicating transport of air from above; in the absence of EPP-induced enhancements this air is depleted in NO_x. Because the only source of NO_x in the polar winter mesosphere is EPP, increasing values of NO_x with decreasing CH_4 indicate the presence of EPP-induced enhancements in the air transported from above [*Siskind et al.*, 1997]. We search for anti-correlations between CH_4 and NO_2 using $CH_4 < 0.27$ ppmv as the requirement to indicate descent from above the stratosphere; this is consistent with *Randall et al.* [2007]. When such anti-correlations are present, we quantify the deviation from the positive correlation using the method described in *Randall et al.* [2007], labeling the deviations as excess NO_2. One modification to *Randall et al.* [2007] is that the excess NO_2 was calculated in weekly instead of two-week time periods because MIPAS has daily global coverage, and thus significantly more data than HALOE, which sampled only a single latitude in each hemisphere on any given day. The excess NO_2 densities are mainly seen in November, December, January and March for the 2002–2003 NH winter, June to August in the 2003 SH winter and February and March for the 2003–2004 NH winter. The largest excess is seen in the 2003–2004 NH winter, with densities peaking at over 100×10^8 cm^{-3}. Peak densities are near 30×10^8 cm^{-3} in the 2003 SH winter and 5×10^8 cm^{-3} in the 2002–2003 NH winter. Figure 2.6 compares the subtraction and CH_4 methods applied to the MIPAS data. The top panels in Figure 2.6 show the quantification of excess nighttime NO_2 densities in the vortex at the 2000 K level as a function of time for the 2002–2003 Arctic winter, the 2003 Antarctic winter and the 2003–2004 Arctic winter. The solid, black lines show the amount of EPP-produced NO_2 inferred from the subtraction method. The diamond symbols with the dashed lines show the amount of excess NO_2 using CH_4 as a tracer as described in the previous paragraph. Each diamond represents an average of all of the points deemed to be excess NO_2 for each respective one-week time period. Also shown in gray is the 1-σ standard deviation excess NO_2 with the CH_4 method, where 1-σ refers to one standard deviation above or below the mean value of excess NO_2. In general

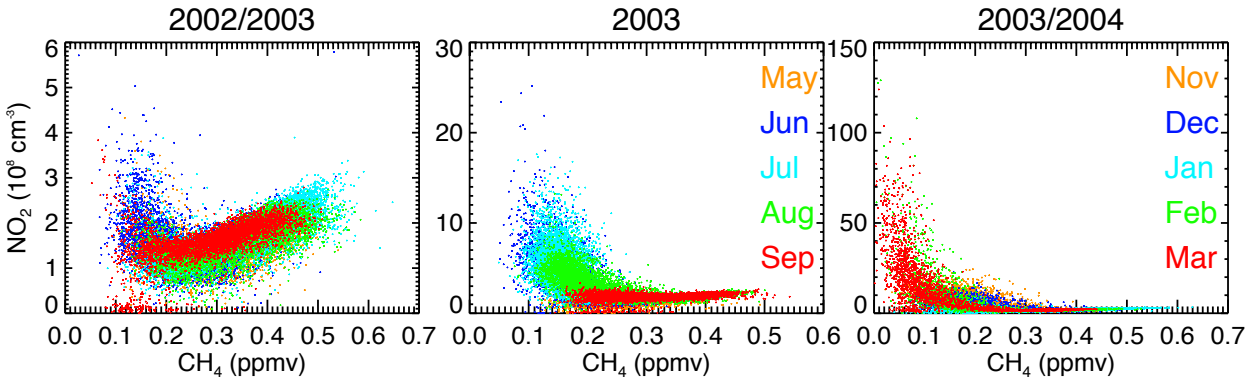

Figure 2.5: MIPAS nighttime NO_2 versus CH_4 at 2000 K for the (left) 2002–2003 Northern Hemisphere (NH), (middle) 2003 Southern Hemisphere (SH), and (right) 2003–2004 NH winters. The months are colored as shown in the middle plot for the SH and the right plot for the NH. Note the different vertical scales in each plot.

there is very good agreement between the subtraction method of approximating excess NO_2 and the CH_4 method. The bottom panels in Figure 2.6 show the number of Gmol/day crossing 2000 K as a function of time for the same time periods as in the top panels with the subtraction (solid line) and CH_4 (diamonds with dashed lines) methods. We approximated the descent rates by the vertical component of the residual circulation, which we calculated using the method of *Solomon et al.* [1986]. Diabatic heating rates and temperatures required for this calculation were obtained from the Modern Era Retrospective-Analysis for Research and Applications (MERRA) [*Rienecker et al.*, 2011].

Figure 2.7 shows the vertical component of the residual circulation ($\overline{w}^*$) for the 1978–1979 and 2002–2003 through 2008–2009 Arctic winters. The residual circulation is by definition a zonal mean quantity, so obtaining a vortex average is not possible. Instead we have averaged the residual circulation poleward of the equivalent latitude of the vortex. This assumption is most appropriate when the vortex is pole-centered and circular, but will introduce some error when the vortex is distorted and/or offset from the pole. In all winters descent increases monotonically with increasing altitude early in the season. Later in the season this pattern changes, so that maximum descent rates might occur anywhere from about 1000–2000 K, but with substantial inter-seasonal variability in the timing and magnitude of the maximum. One obvious feature of note in Figure 2.7 is the interruption of downwelling by major SSW events in the winters of 2003–2004, 2005–2006 and 2008–2009 followed by strong descent into late winter in the lower mesosphere. However, this strong late winter descent might be underestimated with MERRA because the temperature structure in the upper stratosphere is not captured well by MERRA during these events. Measuring vertical velocities in the upper stratosphere remains a difficult problem, but based on the overall agreement of our approximation with published estimates of -400 to -500 m/day in the upper stratosphere [*Funke et al.*, 2005a; *López-Puertas et al.*, 2005a], and the fact that the results are in agreement with our understanding of the basic physics, we believe that using the vertical component of the calculated residual circulation is a reasonable approach.

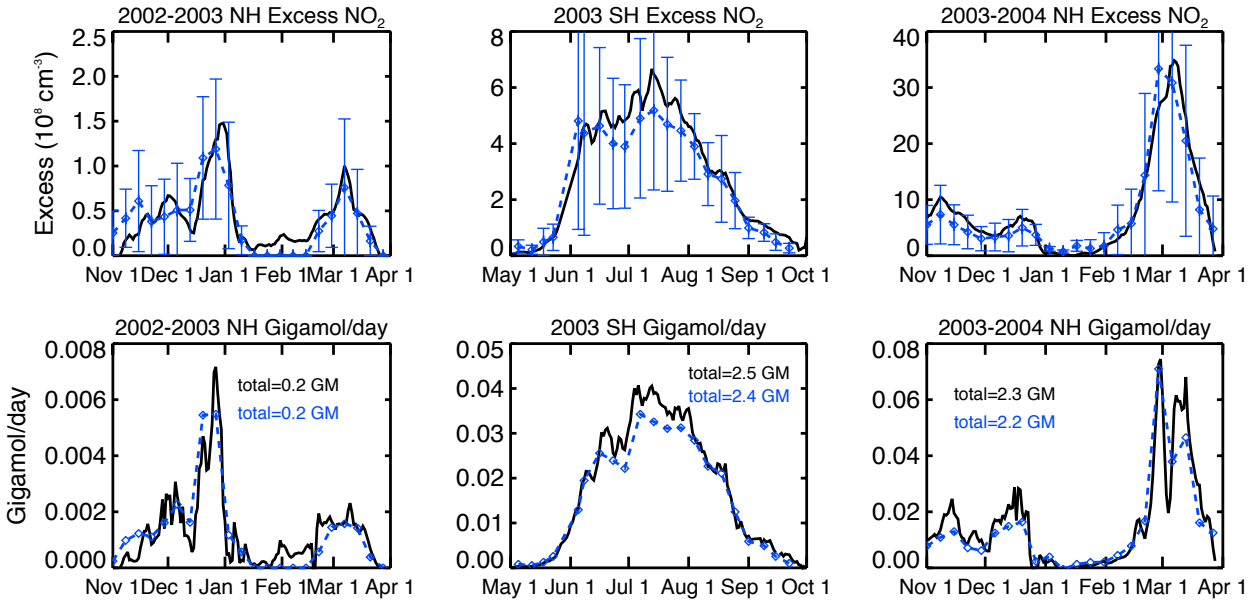

Figure 2.6: (top) Excess nighttime NO_2 densities in the vortex at 2000 K as a function of time for the 2002–2003 Arctic winter, the 2003 Antarctic winter, and the 2003–2004 Arctic winter. (bottom) The number of gigamoles crossing 2000 K per day as a function of time. In the top and bottom graphs, blue diamonds with dashed blue lines represent the CH_4 method, and the black lines represent the subtraction method. Error bars on the CH_4 method indicate 1-sigma standard deviations in the calculated excess NO_2. The total number of gigamoles integrated over each time period is given in Figure 6 (bottom): blue for the CH_4 method and black for the subtraction method.

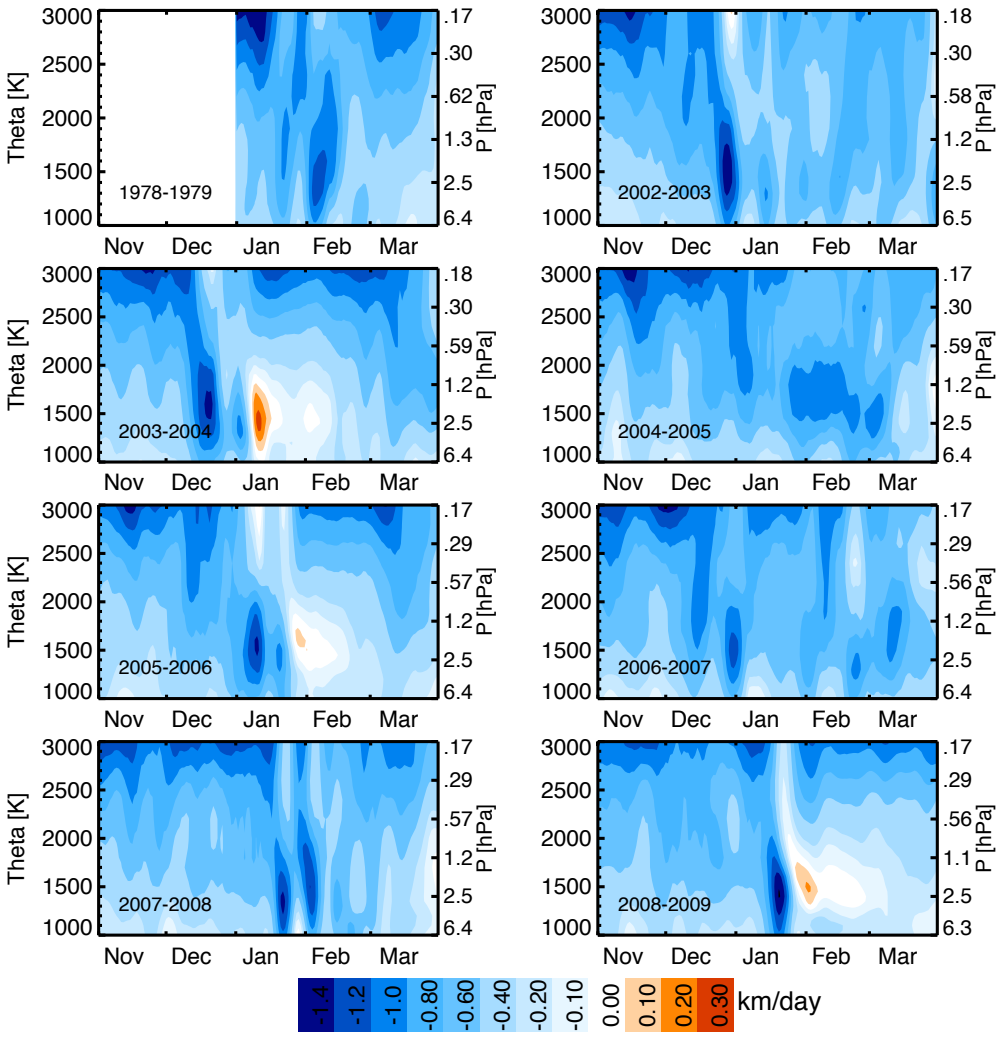

Figure 2.7: Vertical descent rates for the 1978–1979 and 2002–2003 through 2008–2009 NH winters. The descent rates are derived using diabatic heating rates and temperature from Modern Era Retrospective-Analysis for Research and Applications (MERRA) data. For reference, global mean pressure is shown on the right axis.

The total number of Gmol integrated over each time period is noted in the bottom panels of Figure 2.6 for both the subtraction (black) and CH_4 (gray) methods. The total amount of EPP-NO_x crossing the 2000 K level was found to be 0.2 Gmol for the 2002–2003 Arctic winter, 2.5 Gmol for the 2003 Antarctic winter and 2.3 Gmol for the 2003–2004 Arctic winter with the subtraction method, whereas the total amount of EPP-NO_x crossing the 2000 K level was 0.2 Gmol for the 2002–2003 Arctic winter, 2.4 Gmol for the 2003 Antarctic winter and 2.2 Gmol for the 2003–2004 Arctic winter with the CH_4 method. Clearly the results from the subtraction method compare well with the results from the CH_4 method, supporting the validity of applying the subtraction method to satellite measurements of nighttime NO_2. Our results from the subtraction method also compare reasonably well with previous estimates based on measurements of NO+NO_2 and NO_y. *Funke et al.* [2005a] calculated the net deposition of NO_y below 3000 K to be 2.4 Gmol for the 2003 Antarctic winter using MIPAS data, which agrees very well with our estimate of 2.5 Gmol. We note that the ratio of NO_x to NO_y is above 0.9 in the upper stratosphere, so it is reasonable to use these results for comparison to our results with the caveat that NO_x will be a slight underestimate. Our estimate also falls within the range of 1.1–2.6 Gmol that *Randall et al.* [2007] estimated was deposited below 2000 K in the 2003 Antarctic winter using solar occultation data. Using a 3-D model together with MIPAS data, *Reddmann et al.* [2010] estimated the amount of excess NO_y in the stratosphere from July 2002 to March 2004. They estimated the excess NO_y deposited below 55 km for the 2003 Antarctic winter to be 1.4 Gmol. Their estimate of excess NO_y for the 2002–2003 Arctic winter is 0.4 Gmol, while their estimate for the 2003–2004 Arctic winter is 2.0 Gmol. This is in fairly good agreement with our estimates of 0.2 Gmol and 2.3 Gmol for the 2002–2003 and 2003–2004 Arctic winters, respectively. Based on the overall agreement of our subtraction method with previous studies and with the CH_4 method, we conclude that our approach is valid and is reasonable to apply to LIMS data.

Figure 2.8 shows the excess nighttime NO_2 densities at 2000 K in the vortex for the Arctic winter of 1978–1979 (top panel), the vortex area and descent rate at 2000 K (middle

panel) and the number of Gmol/day crossing 2000 K (bottom panel) as a function of time. The descent rates for the 1978–1979 Arctic winter were also estimated by the vertical component of the residual circulation, as described above. MERRA data is only available after January 1979, so we were unable to calculate the descent rates before that time. The total amount of EPP-NO_x crossing the 2000 K level from January–March of 1979 was found to be 0.1 Gmol. Figure 2.7 shows that the descent rates earlier in the winter were generally less than about 400 m/day. Using 400 m/day as an upper estimate, we calculate the total amount of EPP-NO_x crossing the 2000 K level in November–December of 1978 to be 0.1 Gmol. Thus the total amount of EPP-NO_x entering the stratosphere as seen in the LIMS data ranges from about 0.1 to 0.2 Gmol. This is in better agreement, quantitatively, with the amount of EPP-NO_x entering the stratosphere in the 2002–2003 Arctic winter than with the 2003–2004 Arctic winter, as was shown qualitatively in the previous section.

2.4.2 ACE-FTS EPP-NO_x

Scatter plots of ACE-FTS NO_x versus CH_4 for the 2003–2004 through 2008–2009 NH winters are shown in Figure 2.9. Excess NO_x is defined in the same way as for MIPAS (Figure 2.5). A great deal of excess NO_x can be seen in 2003–2004, 2005–2006 and 2008–2009. The largest excess is seen in 2003–2004 with densities peaking around 100×10^8 cm^{-3}. Peak densities are near 20×10^8 cm^{-3} in 2005–2006 and 7×10^8 cm^{-3} in 2008–2009. Figure 2.10 shows the quantification of ACE-FTS excess NO_x densities at 2000 K as a function of time for the 2003–2004 through 2008–2009 NH winters using the CH_4 method. As expected from *Randall et al.* [2009], maximum values are largest in 2003–2004, followed by 2005–2006 and 2008–2009, the years with unusual meteorology. The total amount of EPP-NO_x crossing the 2000 K level in ACE-FTS is given in the Figure 2.10 legend. As noted earlier, no ACE-FTS data are available prior to 21 February 2004. Thus for comparison, we recalculated the total amount of EPP-NO_x from MIPAS data using only the time period from 21 February through 31 March 2004; the result was 1.4 Gmol, which is similar to the ACE-FTS result of 1.8 Gmol.

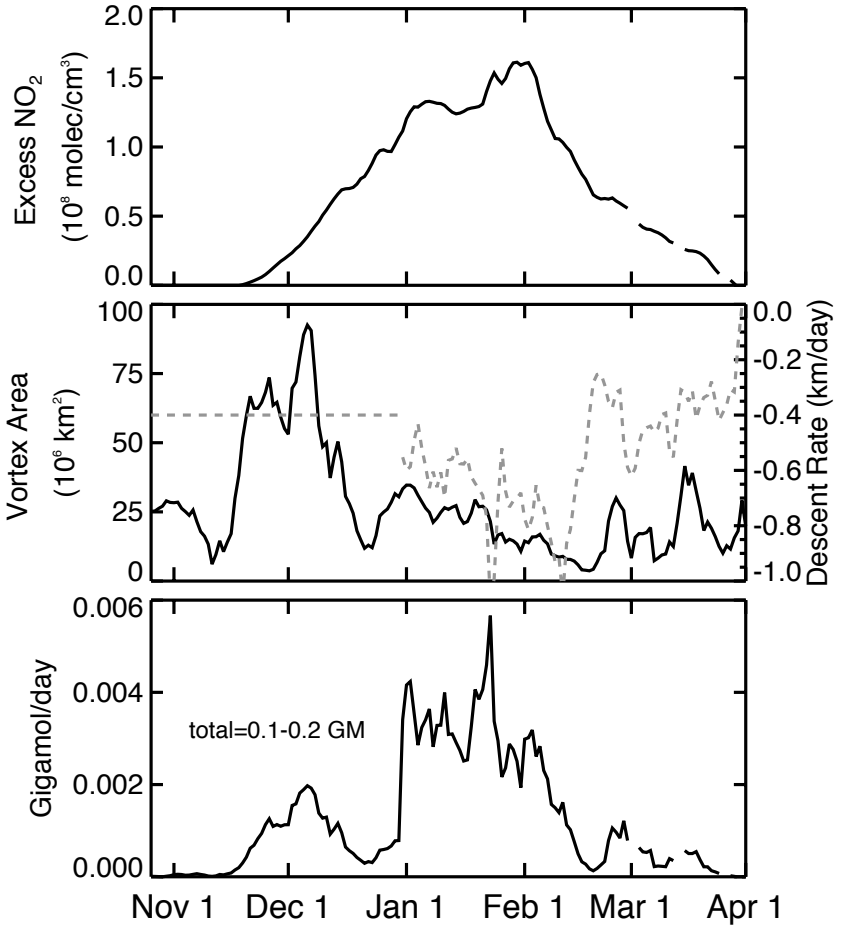

Figure 2.8: (top) Excess nighttime NO_2 densities in the vortex at 2000 K in the 1978–1979 Arctic winter as a function of time, calculated from LIMS data. (middle) The vortex area (black line, left axis) and the descent rate (gray dashed line, right axis). (bottom) The inferred number of Gmol crossing 2000 K per day as a function of time. The total amount for the entire season is also given in the bottom graph.

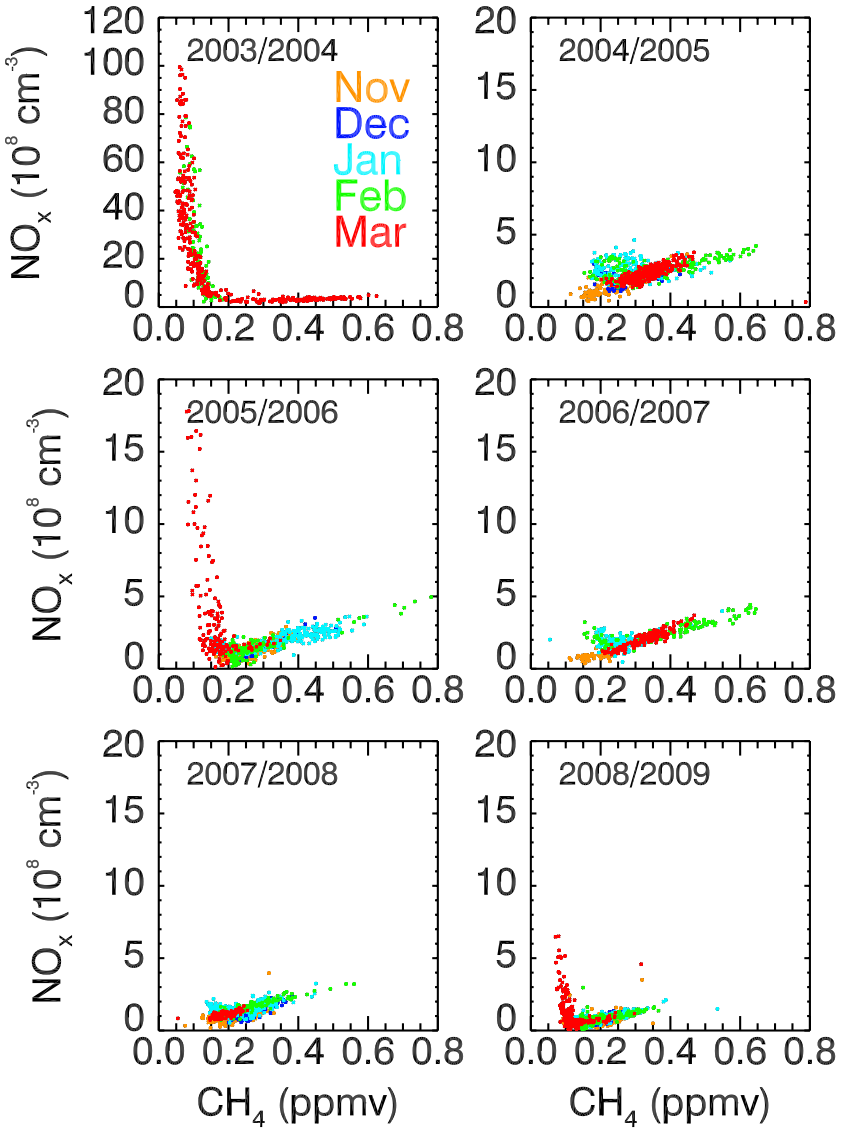

Figure 2.9: ACE-FTS NO_x versus CH_4 at 2000 K for the 2003–2004 through 2008–2009 Arctic winters. The months are colored as shown in the 2003–2004 plot. Note the different vertical scale in the 2003–2004 plot.

Contrary to the maximum values, the total amount of EPP-NO_x descending across the 2000 K level in 2005–2006 and 2008–2009 was not outstanding. Although the unusual meteorology in these winters led to extraordinary enhancements in the descent of EPP-NO_x, these effects occurred too late in the winter for substantial amounts of excess NO_x to descend past 2000 K [e.g., *Salmi et al.*, 2011]. This highlights the fact that the transient effects at 2000 K of the unusual meteorology in these years were not large enough to make up for the fact that descent of EPP-NO_x earlier in the winter was significantly less than in other years.

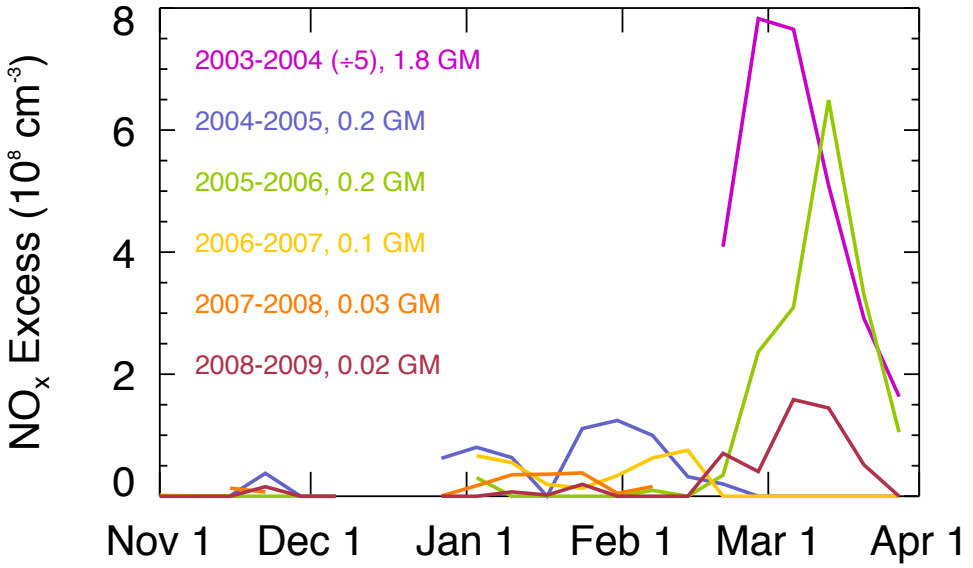

Figure 2.10: Average excess NO_x at 2000 K for ACE-FTS using the CH_4 method for the 2003–2004 through 2008–2009 NH winters. The 2003–2004 line is reduced by a factor of 5 to fit on the plot. Breaks in the line indicate no data, since ACE-FTS did not sample inside the vortex at these times. The sum over each season is shown in Gmol

2.4.3 EPP IE in the NH

Figure 2.11 quantifies the EPP IE, as measured by the amount of EPP-NO_x descending across the 1500 K, 2000 K and 3000 K potential temperature surfaces, for the Arctic winter of 1978–1979 and the Arctic winters of 2002–2003 through 2008–2009. Because ACE-FTS data did not start until February of 2004, MIPAS results are presented for the 2002–2003 and

2003–2004 winters, and ACE-FTS results are presented for the 2004–2005 through 2008–2009 winters. The calculated EPP IE for each NH winter is also summarized in Table 1, which includes results from all calculations performed, including LIMS and ACE-FTS data as well as the MIPAS data from both ESA and IMK/IAA. As shown in Figure 2.11, the largest

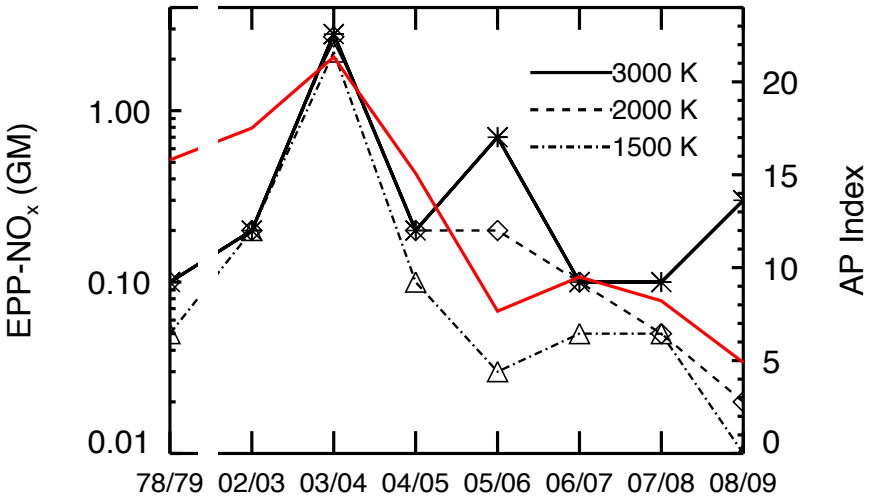

Figure 2.11: Amount of EPP-NO_x descending across the 1500, 2000, and 3000 K potential temperature surfaces deduced from LIMS data in the Arctic winter of 1978–1979, MIPAS data in the Arctic winters of 2002–2003 and 2003–2004, and ACE-FTS data in the winters of 2004–2005 through 2008–2009 (black lines, left axis). The red line shows the A_p index for each of the winters (right axis).

EPP IE observed in the NH at all levels during this time period was the 2003–2004 winter. Table 2.1 shows that the estimate for 2003–2004 from MIPAS-IMK/IAA compares well with ACE-FTS at 2000 K for the time period during which both instruments were observing: 1.9 Gmol and 1.8 Gmol for MIPAS-IMK/IAA and ACE-FTS, respectively. Both the MIPAS-IMK/IAA and ACE-FTS estimates are slightly larger than the MIPAS-ESA estimate at 2000 K, which is most likely a reflection of the difference between using nighttime NO_2 (MIPAS-ESA) and NO_x (ACE-FTS and MIPAS-IMK/IAA) for the calculation. We expect that some of the EPP-NO_x will mix out to lower latitudes as air descends, and that air that reaches 3000 K late in the winter might not reach 2000 K and below by the end of the winter. Consistent with this expectation, the amounts of EPP-NO_x descending across 3000 K for

Table 2.1: The Total Gmol of EPP-NO_x crossing 1500, 2000, and 3000 K for LIMS, MIPAS, and ACE-FTS for the relevant Arctic winters[a]

	1979	2002–2003	2003–2004	2004–2005	2005–2006	2006–2007	2007–2008	2008–2009
LIMS (1500 K)	0.05–0.1	-	-	-	-	-	-	-
MIPAS-ESA (1500 K)	-	0.2	2.2(0.8)	-	-	-	-	-
ACE-FTS (1500 K)	-	-	0.8	0.1	0.03	0.05	0.05	0.01
LIMS (2000 K)	0.1–0.2	-	-	-	-	-	-	-
MIPAS-ESA (2000 K)	-	0.2	2.3 (1.4)	-	-	-	-	-
MIPAS-IMK (2000 K)	-	-	2.7 (1.9)	-	-	-	-	-
ACE-FTS (2000 K)	-	-	1.8	0.2	0.2	0.1	0.05	0.02
LIMS (3000 K)	0.1–0.2	-	-	-	-	-	-	-
MIPAS-IMK (3000 K)	-	0.2	2.8(0.3)	-	-	-	-	-
ACE-FTS (3000 K)	-	-	0.4	0.2	0.7	0.1	0.1	0.3

[a]The amount shown in parentheses is the amount after 21 February, for comparison to the ACE-FTS data. Nighttime NO_2 is used for the first three rows of Table 1, and NO_x is used for the subsequent rows.

the 2005–2006 and 2008–2009 Arctic winters were larger than at 2000 K, by over a factor of 3 and 20, respectively. The MIPAS-IMK/IAA data show similar values at 1500 K (2.2 Gmol), 2000 K (2.7 Gmol) and 3000 K (2.8 Gmol) in 2003–2004, suggesting that very little mixing to lower latitudes occurred during the descent. In fact, 2003–2004 is the only year for which the signal of upper atmospheric NO_x is evident at or below 1000 K (the NO_x-CH_4 relationship in 2003–2004 shows evidence of EPP-NO_x down to 800 K). That the amount for the 2003–2004 winter is less at 3000 K than at 2000 K for ACE-FTS can be explained by the fact that ACE-FTS did not have observations before 21 February when the enhancements would have been present at 3000 K. Again we compared MIPAS-IMK/IAA and ACE-FTS calculations for 21 February through 31 March 2004, the time period that was observed by both instruments. The results, 0.3 Gmol using MIPAS-IMK/IAA data and 0.4 Gmol using ACE-FTS data, were very similar.

Also shown in Figure 2.11 is the A_p index corresponding to each season (average A_p index from 1 October through 31 March). The correlation between the A_p index and the amount of EPP-NO_x descending across a given potential temperature surface is not obvious, although the correlation coefficient is 0.66 for 2000 K and 0.55 for 3000 K. With only eight years of data, we cannot say with confidence if this is significant. Nevertheless, the lack of strong correlation is consistent with the fact that both geomagnetic activity and dynamics influence the amount of EPP-NO_x reaching the stratosphere. If we exclude the years with unusual dynamics, the correlation coefficient between the A_p index and the amount of EPP-NO_x crossing both 2000 and 3000 K becomes 0.8; again, we emphasize that this is based on only five years of data.

2.5 Summary and Conclusions

In this paper we have compared LIMS NO_2 data from 1978–1979 to more recent data from MIPAS and ACE-FTS from 2002–2009. The magnitude and timing of the LIMS NO_2 enhancements in the 1978–1979 Arctic winter are similar to enhancements in the Arctic

winters of 2002–2003, 2004–2005, 2006-2007 and 2007–2008 in the MIPAS and ACE-FTS data. We calculated that when integrated over the entire winter, approximately 0.1 Gmol of EPP-NO_x descended past the 1500 K, 2000 K and 3000 K surfaces in 1978–1979. This is similar to the amount of EPP-NO_x in the winters just mentioned, For reference, 0.1 Gmol is approximately 0.5% of the annual average contribution to Arctic (>50° latitude) NO_y from the oxidation of N_2O that *Vitt and Jackman* [1996] calculated using a 2-D photochemical transport model averaged over 20 years from 1974–1993.

The largest EPP IE on record was the 2003–2004 winter, when approximately 2.2 Gmol of EPP-NO_x descended across the 1500 K potential temperature surface. An extraordinary EPP IE has been reported previously for the 2005–2006 and 2008–2009 winters [e.g., *Randall et al.*, 2009]. During these winters, however, the unusually strong EPP IE occurred later in the season than in 2003–2004, and was primarily confined to altitudes above 2000 K. We report here that 0.2 and 0.1 Gmol of NO_x descended across the 2000 K and 1500 K surfaces, respectively, in 2005–2006, and 0.02 and 0.01 Gmol of NO_x descended across the 2000 K and 1500 K surfaces, respectively, in 2008–2009. These numbers are on the same order as, or in the case of 2008–2009 smaller than, the numbers for all other years analyzed. On the other hand, significantly more EPP-NO_x was observed at 3000 K in 2005–2006 and 2008–2009, so that these years ranked second and third, respectively, after 2003–2004, in the total amount of EPP-NO_x crossing the 3000 K surface. The differences between the results at 1500 K, 2000 K and 3000 K reflect the fact that the unusually strong enhanced descent in 2006 and 2009 occurred late enough in the season that the enhancements largely dissipated before reaching the 2000 K surface.

Overall, the results reported here confirm that in the NH, the total amount of EPP-NO_x transported to the stratosphere depends on both the level of EPP and the prevailing dynamics. That more total EPP-NO_x was observed to descend into the stratosphere in 2003–2004 than in any other winter is because that particular winter had a moderately high level of EPP and favorable dynamical conditions to transport NO_x-rich air from the MLT to the

stratosphere. In 2005–2006 and in 2008–2009, substantially more EPP-NO_x was observed to descend across the 3000 K surface than in any other year aside from 2003–2004, even though the level of EPP was low. But the timing of the enhanced descent was such that the total amount of EPP-NO_x crossing the 2000 K surface was not unusual. The LIMS results from 1978–1979 are similar both morphologically and quantitatively to the results from winters in which there was an average or low level of EPP and no unusual dynamics, consistent with conditions in the 1978–1979 winter itself.

The estimation of descent rates is a primary source of uncertainty in our calculations of the integrated amount of EPP-NO_x descending across different potential temperature surfaces. There is likely high variability in the descent rates at different locations inside the polar vortex, yet we use a single descent rate on any given day. Also, since the residual circulation is by definition a zonal average quantity, our method essentially assumes a pole-centered vortex. Another source of uncertainty is that there is no tracer available in the LIMS dataset, so we assumed that all of the NO_2 in the vortex was EPP-NO_x from above. This assumption will not be valid if there are intrusions of NO_x-rich air from lower latitudes during SSWs at the altitudes that the calculation is performed at. However, in the years discussed here we showed that this is a reasonable assumption by comparing both the subtraction and CH_4 methods with the MIPAS data. Yet a third source of uncertainty is that we assumed that the vortex at 3000 K was the same as the vortex at 2000 K. This is likely a conservative estimate since the vortex generally grows larger with increasing height, so the estimates at 3000 K are likely underestimates. This could especially be true following major SSWs when the vortex at higher altitudes is sometimes much larger in area than at lower altitudes [e.g., *Funke et al.*, 2005a; *Mengistu Tsidu et al.*, 2005].

The NO_x enhancements in the 1978–1979 Arctic winter, although relatively small, were very evident in the LIMS data because of its nighttime measurement capability, enabling it to measure NO_2 throughout the polar night. Between 1979 and 2002, when MIPAS was launched, the only satellite instruments capable of such measurements were the Improved

Stratospheric and Mesospheric Sounder (ISAMS), which had a limited lifetime, and the Cryogenic Limb Array Etalon Spectrometer (CLAES), both aboard UARS. Thus, the lack of reported EPP-NO_x descending to the NH stratosphere in the 1980s and 1990s was most likely due to a lack of appropriate measurements. Nighttime measurements of NO_2 are a useful proxy for total NO_x in the stratosphere and lower mesosphere [e.g., *Seppälä et al.*, 2007a]. An instrument like LIMS would not be able to capture NO_x in the mesosphere and higher, however, since above about 65–70 km NO_x is in the form of NO. To fully characterize the EPP-NO_x production and descent, observations of NO_x from the stratosphere to the lower thermosphere throughout the polar winter are required.

2.6 Extended Results

In the time since *Holt et al.* [2012] was published, MIPAS-IMK/IAA NO_x and CH_4 data has been made available for the entire MIPAS observing record from 2002–2012. In this section the methods described in *Holt et al.* [2012] are extended to estimate the EPP IE for all of the available NH winters. Figure 2.12 shows MIPAS-IMK/IAA NO_x mixing ratios averaged poleward of 60°N as a function of altitude and time for the NH winters of 2002–2003 through 2011–2012. The EPP IE can be clearly seen in several of the NH winters, most notably 2003–2004, 2008–2009, and 2011–2012. Unfortunately there are several large temporal gaps from 2004–2005 through 2006–2007. The 2003–2004 NH winter still has by far the largest NO_x mixing ratios ever observed, with polar average mixing ratios exceeding 200 ppbv in the upper stratosphere. The 2003–2004 NH mixing ratios at ∼50 km are an order of magnitude higher than any other winter.

Figure 2.13 shows the flux of EPP-NO_x in Gmol/day crossing 2000 K as a function of time for the 2002–2003 through 2011–2012 NH winters. The fluxes are vortex-average values. EPP-NO_x is calculated with the CH_4 method (see Section 2.4).

Figure 2.14 shows the EPP IE as the Gmol EPP-NO_x descending past the 2000 K surface from November through March of each season. The dashed line shows the EPP IE

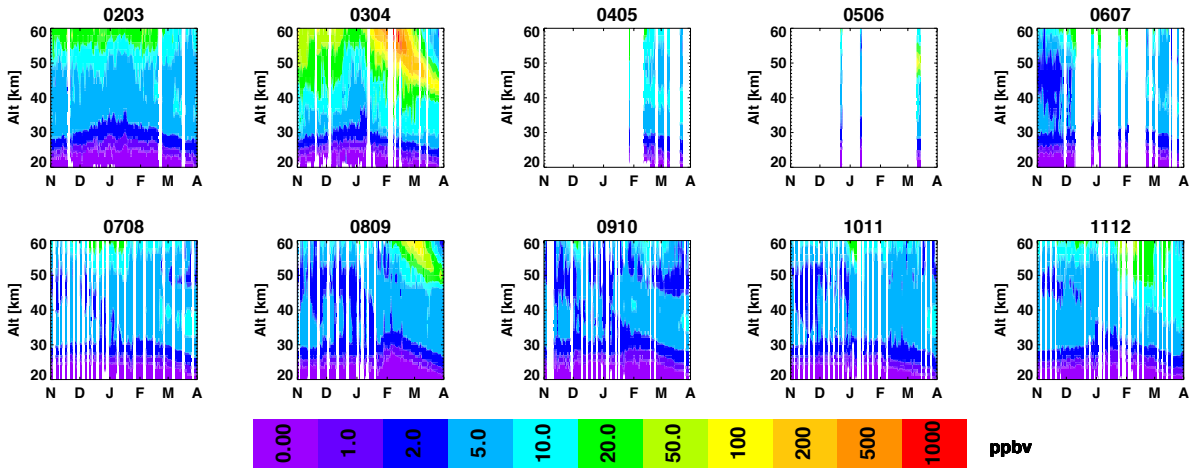

Figure 2.12: MIPAS-IMK/IAA NO_x mixing ratios averaged poleward of 60°N (area-weighted) as a function of altitude and time for the NH winters of 2002–2003 through 2011–2012. White regions indicate missing data.

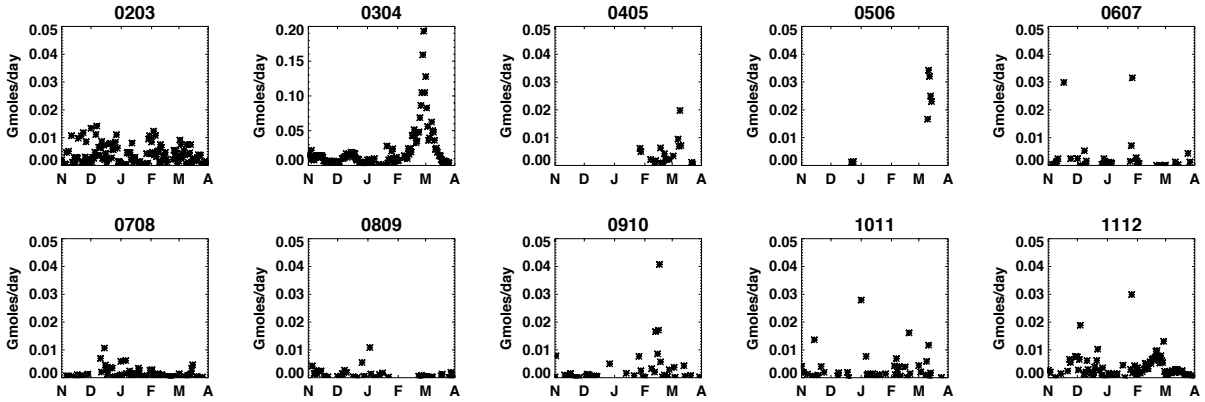

Figure 2.13: MIPAS-IMK/IAA vortex average EPP-NO_x crossing 2000 K for the NH winters of 2002–2003 through 2011–2012. Note the different scale for 2003–2004.

at 2000 K found above in *Holt et al.* [2012], which used MIPAS ESA data in the 2002–2003 and 2003–2004 NH winters and ACE-FTS data in the 2004–2005 through 2008–2009 NH winters. There is good agreement between MIPAS-IMK/IAA in 2003–2004, but the EPP IE for 2002–2003 is a factor of 2 larger with MIPAS-IMK/IAA than with MIPAS ESA. MIPAS ESA only has nighttime NO_2, whereas MIPAS-IMK/IAA has NO_x. The 2004–2005 through 2006–2007 NH winters cannot be compared since there is so little MIPAS-IMK/IAA data during those winters. The EPP IE measured by ACE-FTS for the 2007–2008 and 2008–2009 NH winters is 0.05 and 0.02 Gmol, respectively, at 2000 K, and the EPP IE measured by MIPAS-IMK/IAA here is 0.1 and 0.04 Gmol for the 2007–2008 and 2008–2009 NH winters, respectively. In both years the EPP IE is a factor of 2 larger with MIPAS-IMK/IAA. The discrepancy might be explained by the difference in the instruments, that is, that MIPAS measured in the polar night and ACE-FTS is a solar occultation instrument.

The correlation between the EPP IE and the A_p index for the extended analysis is 0.65, which is very close to the correlation of 0.66 at 2000 K found with LIMS, MIPAS ESA, and ACE-FTS above. The 2003–2004 NH winter is still by far the largest EPP IE ever observed.

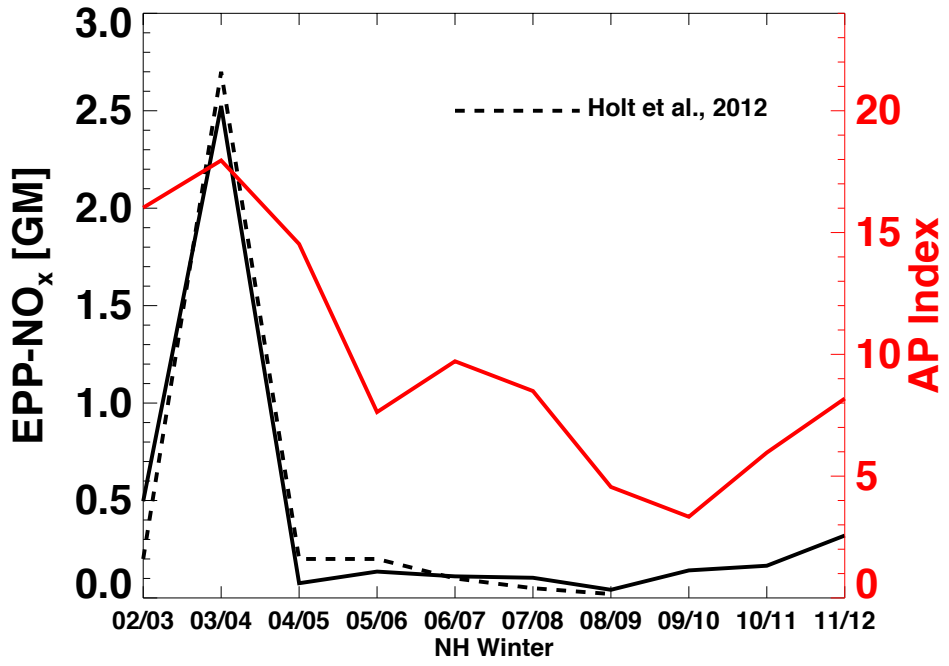

Figure 2.14: MIPAS-IMK/IAA EPP IE as Gmol EPP-NO_x descending past 2000 K for the 2002–2003 through 2011–2012 NH winters. The dashed line is from *Holt et al.* [2012].

Chapter 3

Response of the EPP IE to the Non-Orographic Gravity Wave Source in WACCM

3.1 Introduction

While observations offer abundant observational evidence for the EPP IE (see Section 1.7), no current or previous instrument has measured the polar winter descent of NO_x from its source region down through the mesosphere to the stratosphere. Therefore modeling studies are necessary to fill in the gaps not covered by observations. WACCM is one of the best models available to study the EPP IE. The top of the model is well above the altitude of EPP-NO_x production so that the whole EPP IE from the source to the stratosphere can be studied. WACCM includes a six-constituent ion chemistry model (O^+, O_2^+, N^+, N_2^+, NO^+, and electrons) [*Marsh et al.*, 2007]. In addition to extreme ultraviolet photons, soft X-rays, and photoelectrons, the ionization sources include auroral EPP, which is parameterized based on the auroral module in NCAR TIME-GCM [*Roble and Ridley*, 1987, 1994]. The parameterization inputs hemispheric power (HP) and outputs ion-pair production rates. HP is parameterized based on an empirical relationship between HP and the K_p planetary geomagnetic index [*Neale et al.*, 2010, and references therein]:

$$\mathrm{HP} = \begin{cases} 16.82 \cdot K_p \cdot \exp 0.32 - 4.86 & \text{if } K_p \leq 7 \\ 153.13 + 146.87 \left(\frac{K_p - 7}{2} \right) & \text{if } K_p > 7 \end{cases}$$

where HP is in gigawatts. WACCM reproduces several characteristics in the distribution of NO observed by SNOE [*Marsh et al.*, 2004].

GWs are one of the fundamental drivers of the TEM circulation, and successfully modeling the EPP IE critically depends on our ability to reproduce the transport by the mean circulation. Therefore the treatment of GWs in general circulation models determines how well the model reproduces the EPP IE. Recent studies with WACCM show that the EPP IE is underestimated in the model compared to observations. In this chapter several WACCM simulations are compared to evaluate the sensitivity of the EPP IE to the GW tuning in the model.

3.2 Gravity Wave Parameterization in WACCM

Since small-scale GWs are produced by sub-grid processes, it is not possible to explicitly represent them in numerical models. Thus, the effects of GWs must be represented with parameterizations. For example, parameterizations have been successfully used to demonstrate how GWs drive the zonal mean state of the mesosphere away from radiative equilibrium [*Garcia*, 1991]. However, this is not an easy task due to their multifarious and complex interactions with the flow. WACCM incorporates a non-orographic GW parameterization developed by *Lindzen* [1981], *Holton* [1982], *Garcia and Solomon* [1985], and *Sassi et al.* [2002]. The parameterization for orographically generated GWs is based on *McFarlane* [1987].

The non-orographic GW parameterization contains a tunable parameter, τ_b, with a default value set so that the height of the polar mesopause is consistent with observations [*Neale et al.*, 2010]. The source stress spectrum is a Gaussian in phase speed launched from 600 mbar and oriented in the direction of the wind on that surface:

$$\tau_s(c) = \tau_b \exp\left[-\left(\frac{c - U_s}{c_w}\right)^2\right] \tag{3.1}$$

where U_s is the magnitude of the source wind, $U_s = |\vec{U_s}|$ with width $c_w = 30$m/s and phase speeds are

$$c \in U_s + [\pm d_c, \pm 2d_c, ... \pm c_{max}] \tag{3.2}$$

with $d_c = 2.5$ m/s and $c_{max} = 80$ m/s, giving 64 phase speeds [*Garcia et al.*, 2007]. In the absence of dissipative processes, such as radiative cooling or diffusion, conservation of kinetic energy dictates that GW amplitudes grow exponentially with height until they become convectively unstable [*Brasseur and Solomon*, 2005]. By decreasing the value of τ_b, the GWs propagate higher up in the atmosphere before breaking, and the altitude of the peak GW momentum deposition moves up. Essentially τ_b controls the level at which non-orographic gravity waves break and deposit their momentum.

There have been significant improvements to the GW parameterization in progressive versions of WACCM in the last decade or so, and they have been refined again in WACCM4. Two important updates are the addition of surface stress due to unresolved orography (turbulent mountain stress) and improved parameterization of non-orographically generated GWs [*Neale et al.*, 2010]. In regards to the latter, *Richter et al.* [2010] added source-oriented trigger functions to WACCM3.5 (that have also been implemented in WACCM4) that depend on processes that promote GWs such as convection and frontogenesis; whereas previous versions used specified source functions of location and season. They found that WACCM3.5 was much closer to observations in terms of major SSW event interannual variability and frequency, which they attributed separately to two improvements to the model. The improvement in interannual variability was attributed to the improved parameterization of non-orographic GWs. The better modeling of major SSW event frequency was attributed to the added mountain stress near the surface, which affects the propagation of stationary planetary waves into the polar vortex through interaction with the mean wind and orographic GWs. They concluded that gravity waves and planetary waves must both be properly accounted for in general climate models to realistically represent stratospheric variability.

3.3 Residual Circulation in WACCM

Recent modeling studies have shown that the amount of NO_x transported from the MLT to the stratosphere in NH winter is underestimated by WACCM compared to obser-

vations. *Smith et al.* [2011] suggest that the TEM circulation is not correctly reproduced in WACCM. It is not possible to compute the TEM circulation directly with observations like it is with a model. To evaluate the TEM circulation in WACCM, *Smith et al.* [2011] compared the distribution of tracers to their observed distribution. Figure 3.1 compares climatological mixing ratios of O from SABER and WACCM for June and December. The lifetime of O above 85 km is long enough that its mixing ratio responds to transport by the mean circulation. In June the contours of constant mixing ratio slope upward from the SH

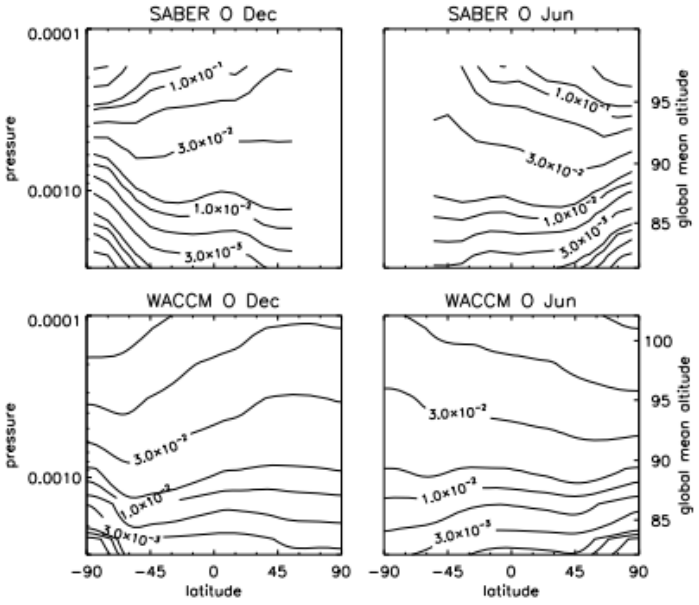

Figure 3.1: Climatological mixing ratio of atomic oxygen from (top) SABER (2002–2010) and (bottom) WACCM for December and June. Figure 6 from *Smith et al.* [2011].

to the NH at 85 km and downward at 95 km, which indicates downwelling in the winter mesosphere and upwelling above. This transition between upward sloping and downward sloping contours gives an indication of the altitude at which the circulation changes from upwelling to downwelling. SABER and WACCM agree that the SH June transition is at ∼0.0008 hPa, but the NH December transition is at ∼0.0008 in WACCM and ∼0.0005 in SABER. Therefore, while Figure 3.1 confirms the basic structure of the TEM in the MLT, it also suggests that the altitude of the transition between downwelling and upwelling in the

NH winter is too low in WACCM. *Lossow et al.* [2009] found a similar discrepancy in seasonal distributions of polar water vapor (H_2O) measured by the Odin submillimeter radiometer and WACCM.

The transition from downwelling to upwelling in the NH winter is controlled by the altitude of the maximum poleward flow ($\overline{v}^*$) through continuity. Since $\overline{v}^*$ in the MLT is determined by the vertical distribution of GW momentum deposition, the discrepancies in the mixing ratios of O and H_2O suggest that the peak momentum deposition of breaking GWs is too low in altitude in WACCM. If the altitude of the poleward component of the residual circulation is too low, then NO increases by diffusion or chemical processes will not be correctly represented in the model. The vertical distribution of GW momentum deposition depends on τ_b, and since τ_b is a tunable parameter we can perform sensitivity tests to determine how the EPP IE responds to the GW forcing in WACCM.

3.4 Specified Dynamics Whole Atmosphere Community Climate Model

WACCM is normally operated as a free-running climate model; however, to compare WACCM to observations at specific locations and times we use Specified Dynamics WACCM (SD-WACCM). SD-WACCM incorporates reanalysis observations in the troposphere and stratosphere. This is done by relaxing the horizontal winds, temperatures, and surface pressure to MERRA data with the method described by *Kunz et al.* [2011]. The output winds, temperatures, and surface pressure are a linear combination of MERRA and WACCM (0.01 × MERRA + 0.99 × WACCM). The relaxation to MERRA occurs with a timescale of ∼10 h from the surface to 40 km. Between 40 and 50 km the amount of relaxation is linearly reduced, and above 50 km the model is free-running. The model is also forced with surface wind stress, and sensible and latent surface heat flux. With SD-WACCM it is possible to simulate the effects on the mesosphere of a particular dynamical event that occurred in the stratosphere, and also to improve the mean wind climatology [*Marsh*, 2011].

The SD-WACCM simulations used here have a horizontal resolution of 1.89° × 2.5°

(latitude × longitude), and the vertical resolution varies between ∼0.5 to 4 km. SD-WACCM uses a vertical hybrid sigma-pressure coordinate with 88 levels from the surface to ∼145 km and a time step of 1800 s. Other parameters from the time period of the simulations are used to force the SD-WACCM simulations. For example, auroral input is parameterized as described above by the K_p index.

SD-WACCM can be sampled at user specified locations from, for example, satellite or aircraft measurement positions. The model does not interpolate to the satellite measurement location but uses the closest model grid profile, which translates to a maximum offset of 1.25° longitude, 0.95° latitude, and 900 s of the model profile from the satellite profile. Here SD-WACCM simulations of the 2003–2004 and 2005–2006 NH winters are compared to observations from ACE-FTS, MIPAS, and SABER to evaluate the effect of different values of τ_b on the EPP IE.

3.5 SD-WACCM NO_x Compared to MIPAS and ACE-FTS

Figure 3.2 shows NO_x mixing ratios poleward of 70°N for (top) SD-WACCM sampled at MIPAS measurement locations and (bottom) MIPAS for the 2003–2004 NH winter. The default τ_b of 1.5×10^{-3} Pa is used in the SD-WACCM simulation. With the default GW tuning, SD-WACCM underestimates the amount of NO_x transported to the stratosphere compared to MIPAS observations. For example, the MIPAS NO_x 100 ppbv contour reaches ∼40 km at the end of March, whereas the SD-WACCM NO_x 100 ppbv contour reaches slightly above ∼60 km. The timing of the NO_x descent is very well represented in SD-WACCM because of the nudging to reanalysis data below 50 km. The increase in NO_x starting around 1 November 2003 mainly attributed to the large EPP DE during the Halloween Storms.

Figure 3.3 shows NO_x mixing ratios for (top) SD-WACCM sampled at ACE-FTS measurement locations and (bottom) ACE-FTS for the NH winter of 2005–2006. As in Figure 3.2 the default GW tuning is used in the SD-WACCM simulation, and SD-WACCM underestimates the EPP IE compared to ACE-FTS observations. The EPP IE was not as large

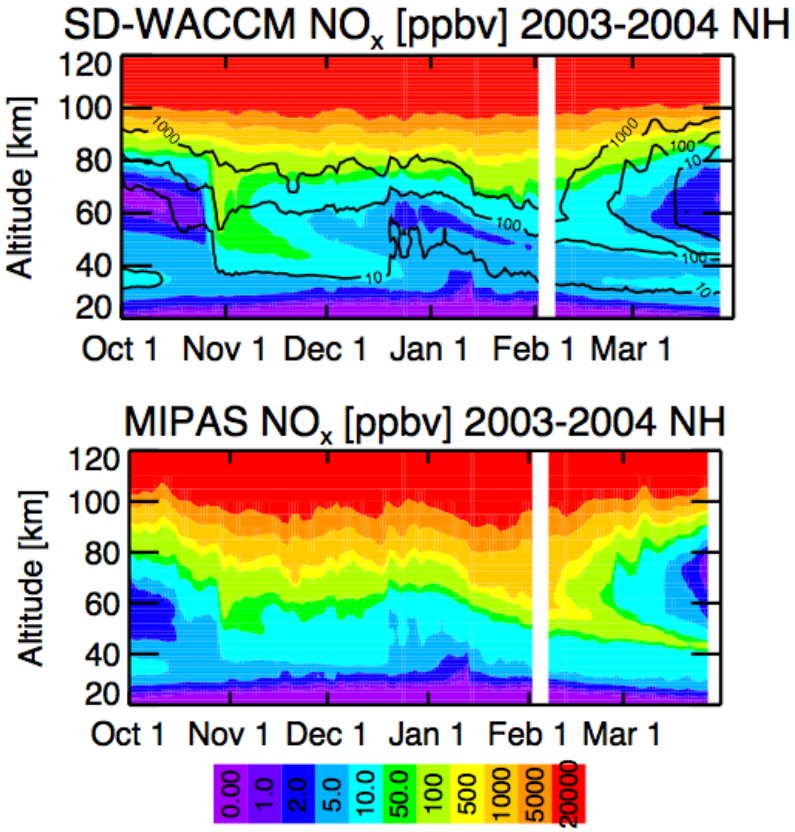

Figure 3.2: SD-WACCM NO_x poleward of 70°N at MIPAS measurement locations for the 2003–2004 NH winter compared to MIPAS NO_x. Black contour lines show MIPAS NO_x mixing ratios overplotted on SD-WACCM NO_x for comparison.

in the 2005–2006 NH winter as it was in the 2003–2004 NH winter, but the descent of NO_x is still clearly evident in ACE-FTS. The ACE-FTS NO_x 100 ppbv contour reaches ∼50 km, whereas the SD-WACCM NO_x 100 ppbv contour barely dips below 80 km. SD-WACCM and ACE-FTS agree fairly well before the middle of February, when the descent of ACE-FTS NO_x begins. However, NO_x increases exponentially above 80 km, so even small deviations of the model from observations could have a large impact on how well the model represents the EPP IE.

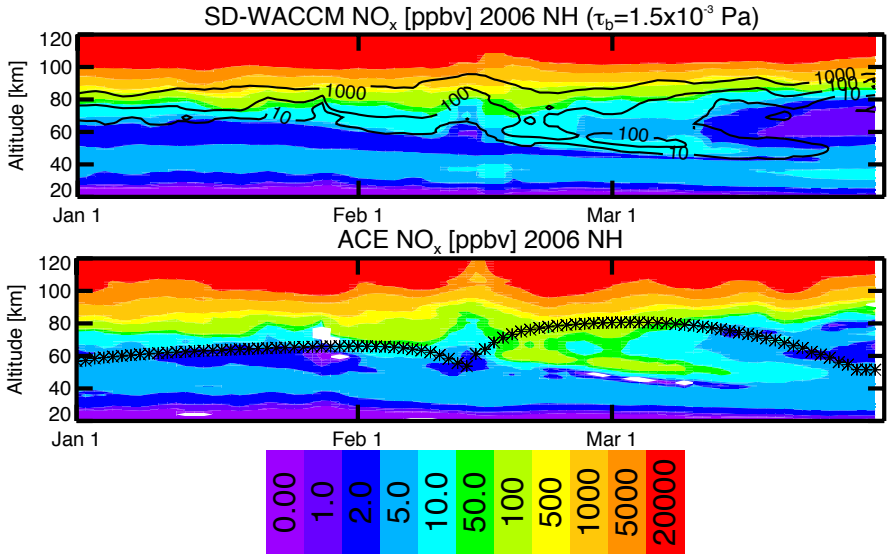

Figure 3.3: SD-WACCM NO_x at ACE-FTS measurement locations for the 2003–2004 NH winter compared to ACE-FTS NO_x. Black contour lines show ACE-FTS NO_x mixing ratios overplotted on SD-WACCM NO_x for comparison. ACE-FTS measurement locations are shown in the bottom panel

3.6 Response of Circulation and NO_x to GW Source Strength

Figure 3.4 shows the monthly mean GW momentum deposition averaged from 50 to 70°N for the 2005–2006 NH winter as a function of log-pressure (log-p) altitude. Decreasing τ_b shifts the peak momentum deposition higher in altitude. The easterly GW drag induces a poleward flow through the Coriolis force, which induces a vertical circulation at the pole

through continuity.

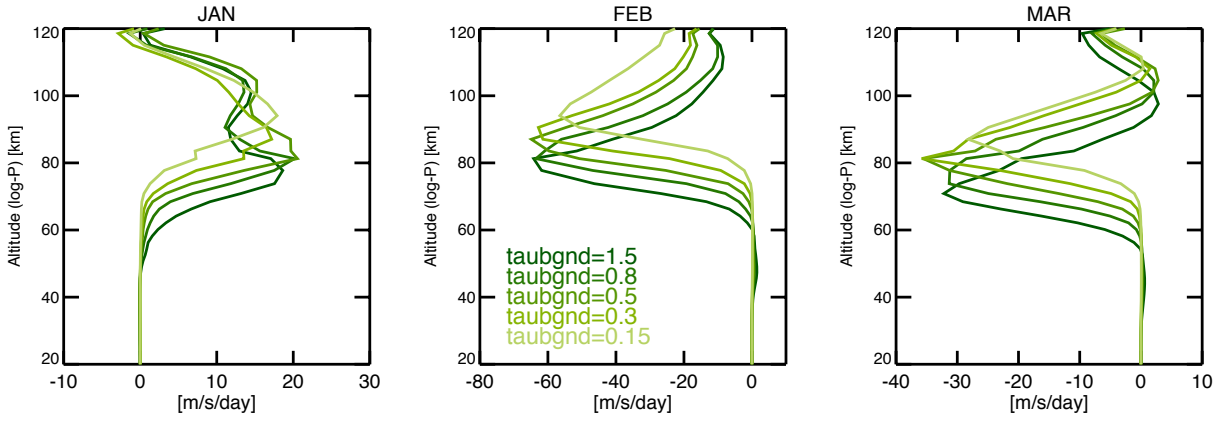

Figure 3.4: SD-WACCM monthly mean GW drag as a function of log-p altitude for 2005–2006 NH winter averaged from 50 to 70°N for different values of τ_b.

Figure 3.5 shows SD-WACCM monthly mean $\overline{w}^*$ for the 2005–2006 NH winter. Decreasing τ_b also shifts the peak $\overline{w}^*$ higher in altitude in response to the shift in peak GW drag. The disruption of the characteristic winter circulation in the January monthly mean is caused by the major SSW event that occurred in January 2006.

Figure 3.6 shows monthly mean NO_x mixing ratios for ACE-FTS and SD-WACCM sampled at ACE-FTS measurement locations. Decreasing τ_b does increase the peak mixing ratio of NO_x; however, it also moves the peak up so that when τ_b is tuned for the amount of NO_x, the altitude of the peak NO_x mixing ratios is too high in altitude. Therefore the problem of WACCM underestimating the EPP IE is caused by more than just the location of the TEM circulation cells. Furthermore, the SD-WACCM NO_x mixing ratios in January, and also above 90 km in February and March, agree fairly well with ACE-FTS mixing ratios, which suggests that the problem is not too little NO_x near the source region of the EPP IE. Another possibility that should be tested is that the molecular or eddy diffusion in WACCM is not strong enough.

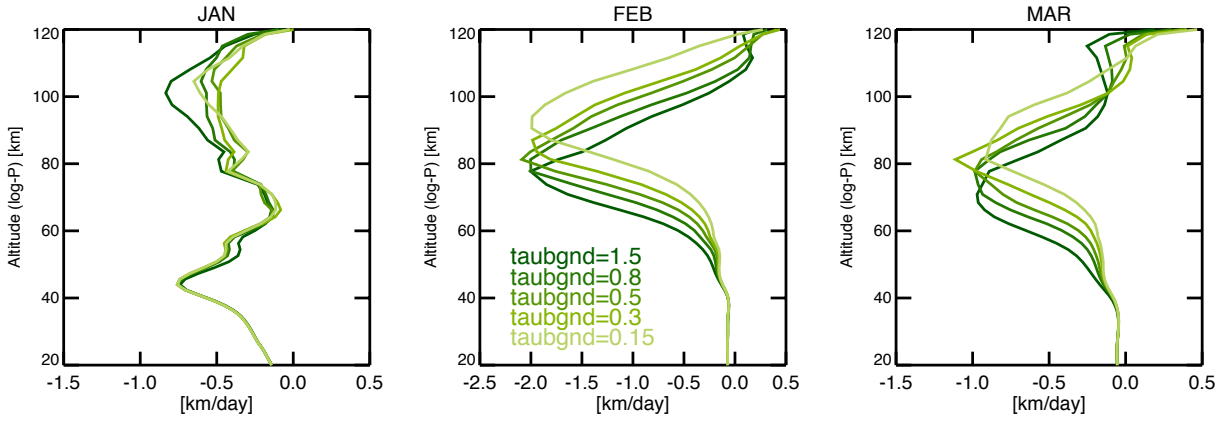

Figure 3.5: SD-WACCM monthly mean $\overline{w}^*$ for 2005–2006 NH winter averaged poleward of 70°N for different values of taubgnd.

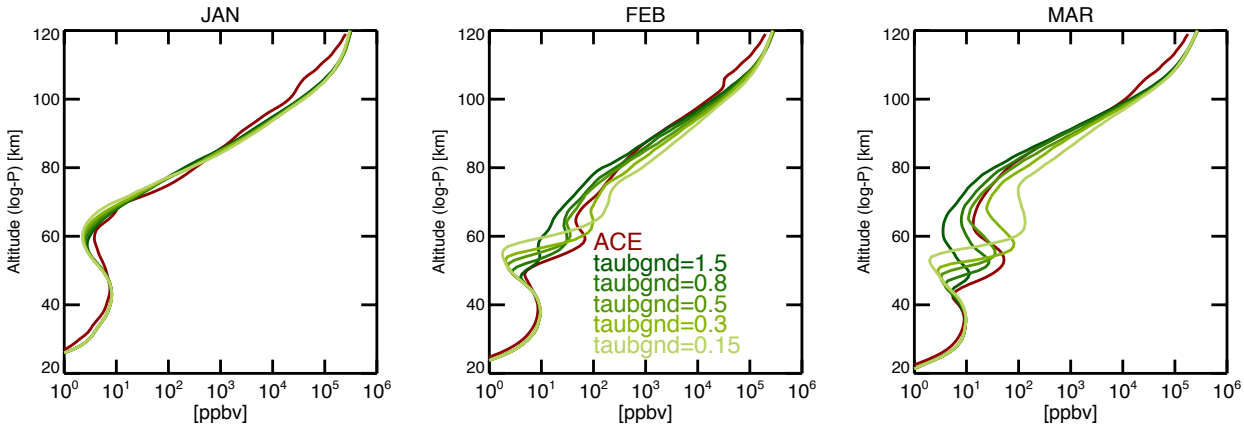

Figure 3.6: SD-WACCM NO_x at ACE measurement locations for the 2005–2006 NH winter compared to ACE NO_x.

3.7 Summary and Conclusions

WACCM underestimates the EPP IE in both free-running and specified dynamics versions of the model. Comparisons of model and observed tracer distributions suggest that the primary altitude of GW forcing is too low in WACCM. Sensitivity tests presented in this chapter show that the EPP IE responds dramatically to the value of τ_b, which controls the peak altitude of the GW momentum deposition. However, these tests also show that there are additional transport mechanisms or EPP sources that are not properly represented in the model.

In conclusion, although WACCM is clearly an appropriate model for investigating the transport of EPP-NO_x from the MLT to the stratosphere, there are issues regarding the parameterization of GWs and other transport mechanisms that must be resolved before robust predictions are achieved. In the future the transport by diffusion in WACCM should be evaluated in addition to ongoing efforts to accurately represent all EPP sources.

Chapter 4

The Influence of Major Sudden Stratospheric Warmings and Elevated Stratopause Events on the EPP IE

This chapter includes *Holt et al.* [2013, submitted][1], which investigates the influence of major SSW and ES events in the NH winter on the transport of NO_x produced by EPP from the MLT to the stratosphere using WACCM. Increases in NO_x following a major SSW and/or ES event are in excess of 100% compared to winters when no major SSW or ES event occurred. The increase in NO_x is attributed to an increase in the descending branch of the residual circulation ($\overline{w}^*$) following the major SSW and/or ES event. The timing of the major SSW and/or ES event strongly affects the amount of NO_x that descends to the stratosphere: the earlier the major SSW and/or ES event occurs, the more NO_x descends to the stratosphere. We also quantify the amount of NO_x produced by EPP descending to the stratosphere in each winter and find that the largest increases in NO_x are in years that have a major SSW followed by an ES event early in the season (December or early January). The strength of $\overline{w}^*$ following a major SSW and/or ES event shows a very strong seasonal dependence and explains why the timing of the major SSW and/or ES event affects the transport of NO_x.

[1] Text as of May 31, 2013

4.1 Introduction

Energetic particle precipitation regularly produces nitric oxide (NO) in the mesosphere and lower thermosphere [e.g., *Crutzen*, 1979; *Thorne*, 1980]. The photochemical lifetime of NO is only a few days in the sunlit mesosphere; however, in the polar night NO can persist for months and be transported to the stratosphere without being photochemically destroyed. As NO descends in the polar region, a portion is converted to nitrogen dioxide (NO_2) through reaction with increasing ozone (O_3). When NO_x (NO + NO_2) created by energetic particle precipitation (EPP-NO_x) reaches the stratosphere it participates in catalytic destruction of O_3, which, since O_3 is a radiatively active gas, can affect the thermal structure of the middle atmosphere. The process whereby EPP influences the stratosphere indirectly is called the EPP indirect effect (EPP IE) [*Randall et al.*, 2006]. This is in contrast to EPP that directly affects the stratosphere when higher energy electrons and protons deposit their energy in situ.

The amount of EPP-NO_x that descends to the stratosphere, i.e., the strength of the EPP IE, depends on both the level of EPP and atmospheric transport. This dependency results in pronounced hemispheric differences. For example, the interannual variability in dynamics in the southern hemisphere (SH) is small, and the SH winter stratosphere is characterized by a strong and steady polar vortex. *Randall et al.* [2007] showed that the amount of EPP-NO_x descending to the SH winter stratosphere is highly correlated with several measures of EPP activity, such as the A_p index and medium energy electron hemispheric power. In the northern hemisphere (NH), where higher planetary wave activity means that minor stratospheric warmings are common and a major sudden stratospheric warming (SSW) event occurs roughly every other year, the amount of EPP-NO_x descending to the stratosphere is strongly influenced by dynamics.

The stratopause lowers in altitude during a major SSW event; following this, the stratosphere becomes isothermal for a few days before the stratopause reforms. After some major

SSW events, the stratopause reforms as high as ∼80 km, an altitude normally associated with the mesosphere. This is referred to as an elevated stratopause (ES) event and has received considerable attention in the most recent decade [e.g., *Manney et al.*, 2008, 2009a,b; *Siskind et al.*, 2010]. ES events occurred in the NH winters of 2003–2004, 2005–2006 and 2008–2009 and had a pronounced impact on the descent of polar NO_x [e.g., *Hauchecorne et al.*, 2007; *López-Puertas et al.*, 2006; *Randall et al.*, 2005, 2006, 2009; *Siskind et al.*, 2007]. It is particularly interesting that the level of EPP was relatively low in 2005–2006 and 2008–2009, yet the amount of EPP-NO_x reaching the upper stratosphere was just as high or higher than that in years with a higher level of EPP [e.g., *Holt et al.*, 2012; *Randall et al.*, 2006, 2009; *Seppälä et al.*, 2007a], highlighting the importance of dynamics in the NH.

The goal of the present study is to further our understanding of the mechanisms controlling the transport of EPP-NO_x in the polar winter using the Whole Atmosphere Community Climate Model (WACCM). Specifically, we investigate the effects of major SSW and ES events on the EPP IE. Section 2 briefly describes the model and simulations used here. Section 3 describes the methods used to identify major SSW and ES events in WACCM. In section 4 we discuss differences in polar NO_x evolution with respect to month of major event occurrence. We also quantify the EPP IE and compare years with no major SSW or ES event, years with a major SSW or ES event, and years with a major SSW event followed by an ES event. Section 5 includes the summary and conclusions.

4.2 Model: Whole Atmosphere Community Climate Model

WACCM is a global, 3-D climate model developed by the National Center for Atmospheric Research (NCAR) that extends from the Earth's surface to the thermosphere [*Marsh et al.*, 2013]. WACCM is an optional superset of the Community Atmosphere Model [*Neale et al.*, 2010], which is the atmospheric component of the Community Earth System Model. WACCM has 66 pressure levels ranging from the surface to 5.1×10^{-6} hPa. The vertical resolution varies and is 3.5 km above ∼65 km, 1.75 km below ∼50 km, 1.1-1.4 km below

$\sim$30 km, 1.1 km in the troposphere, and much higher in the planetary boundary layer. The model resolution of the simulation used in this study is $1.9° \times 2.5°$ (latitude $\times$ longitude).

WACCM includes fully interactive chemistry, radiation, and dynamics. The chemistry module is based on the Model for OZone And Related chemical Tracers (MOZART) and is described in detail by *Kinnison et al.* [2007]. Processes of the mesosphere-lower thermosphere (MLT) are based on the NCAR thermosphere-ionosphere-mesosphere-electrodynamics general circulation model (TIME-GCM), which includes a parameterization for auroral EPP [*Roble and Ridley*, 1987]. The parameterization inputs hemispheric power, which itself is parameterized by the K_p index, and outputs ion-pair production rates. The reader is referred to *Marsh et al.* [2007, 2013] for an in depth description of auroral and solar forcing in WACCM. For detailed descriptions of WACCM gravity wave drag and vertical diffusion parameterizations see *Garcia et al.* [2007] and *Richter et al.* [2010].

Major SSW and ES events commonly occur during Arctic winters in WACCM simulations with a frequency that agrees well with observations. For example, *de la Torre et al.* [2012] found that the frequency of major SSW events in WACCM is very similar to that found in reanalysis data, although the major SSW events are generally prolonged in WACCM and occur disproportionately often in December. *Chandran et al.* [2013] found that the frequency of ES events in WACCM agrees well with the frequency of ES events in the Modern Era Retrospective-analysis for Research and Applications (MERRA) dataset, although they noted that in WACCM ES events are more likely to occur with a vortex splitting event while in MERRA they are more likely to occur with a vortex displacement. The EPP IE is also a self-generated feature of free-running WACCM; however, WACCM underestimates the EPP IE compared to observations [*Smith et al.*, 2011]. Since WACCM has reasonable major SSW and ES events and a self-generated EPP IE, WACCM is a useful tool to study the effects of major SSW and ES events on the EPP IE. Furthermore, with WACCM it is possible to keep the level of EPP constant in order to isolate the effects of dynamics on the EPP IE.

In this study we have used two WACCM version 4 simulations [*Marsh et al.*, 2013]. The runs include forcing for auroral electrons but not solar protons or higher energy electrons. The runs are referred to throughout the rest of the paper as R1 and R2. Each simulation is a 42-year, perpetual year 2000 AD (annually-repeating) simulation. Seasonally-varying solar spectral irradiance was specified, based on the model of *Lean et al.* [2005] as described in *Marsh et al.* [2013]. Sea surface temperatures (SSTs) were also specified, based on monthly mean SSTs constructed from the monthly mean Hadley Centre sea ice and SST dataset version 1 and version 2 of the National Oceanic and Atmospheric Administration weekly optimum interpolation SST analysis [*Hurrell et al.*, 2008]. In order to study the effects of major SSW and ES events on the EPP IE, the level of auroral EPP, which is parameterized by the geomagnetic index K_p, was held constant. For the simulations used in this study the K_p index was set to 4 (A_p=27). For reference, the average of the daily A_p index (obtained from the National Geophysical Data Center) for 2002–2012 is ∼9.7, where the 90th percentile is 21. The first two years of each simulation were discarded to remove any influence of model spin-up, so that each run contains 39 NH winters (November through March).

4.3 Analysis

4.3.1 Major Sudden Stratospheric Warming Detection

We use the algorithm of *Charlton and Polvani* [2007] to detect major SSW events in WACCM. They follow the first criterion of the World Meteorological Organization (WMO): the zonal mean zonal winds at 60°N and 10 hPa become easterly during the winter (November–March). They ignore the second WMO criterion, that the temperature gradient is positive between 60° and 90°N, because it does not significantly change the number of major SSW events identified. The first day that this definition is met is defined as the central warming date. Their algorithm also imposes two additional criteria: (1) the zonal mean zonal winds must remain westerly for 20 consecutive days after a central warming date before another

can be identified and (2) the zonal mean zonal wind must return to westerly for at least 10 days before April 30. If the second condition is not met the warming is considered to be a final warming, which initiates the transition from winter westerlies to summer easterlies.

4.3.2 Elevated Stratopause Detection

We define an ES event using the method described in *de la Torre et al.* [2012] and *Chandran et al.* [2013]. The method can be summarized as follows. An ES event is identified as an increase of 15 km or more in the stratopause height from one day to the next between November and March. The stratopause is defined as the maximum temperature between 20 and 100 km. The temperature is averaged poleward of 75°N and smoothed with a 9-day running mean to eliminate short-term excursions in stratopause height that result from transient wave forcing. The central date of the ES event is defined as the date of the displacement in the stratopause.

4.4 Results and Discussion

4.4.1 Major SSW and ES Events

Table 4.1 shows the major SSW and ES events found in each run using the above definitions of major SSW and ES event. 18 major SSW and 17 ES events occurred in R1, and 11 major SSW and 7 ES events occurred in R2. The frequency of occurrence for major SSW events is 0.46 per winter for R1 and 0.28 per winter for R2, and the frequency of occurrence for ES events is 0.44 per winter for R1 and 0.18 per winter for R2. The frequency of occurrence for both simulations together is 0.37 major SSW events per winter and 0.31 ES events per winter. Most ($\sim$ 71%) ES events occur after a major SSW event. Table 4.1 also shows the number of times that a major SSW and ES event occur together (SSW-ES). ES events that follow a major SSW event occur 8 days, on average, after the major SSW event with a range of 2 to 15 days. There are 12 SSW-ES events (0.31 per winter) in R1

Table 4.1: Number of major SSWs and ES events for the two WACCM simulations. The frequency of occurrence in number per winter is given in parentheses.

Run	R2 (39 winters)	R2 (39 winters)	Combined (78 winters)
Number of SSWs	18 (0.46)	11 (0.28)	28 (0.37)
Number of ES events	17 (0.44)	7 (0.18)	24 (0.31)
SSW and ES	12 (0.31)	5 (0.13)	17 (0.22)

and 5 SSW-ES events (0.13 per winter) in R2. Although we do not explicitly calculate the effects of minor SSW events on EPP-NO_x transport in this study, we note that there were ∼2.0 minor SSW events per winter in R1 and ∼1.8 minor SSW events per winter in R2. We define a minor warming as an increase of at least 25 K within a period of 7 days below 10 hPa. There were only 2 winters in the 78 model years (∼3%) without any minor or major SSW or ES event (i.e., dynamically calm winters).

The occurrence frequencies for major SSW events in R1 and R2 are lower than those found by *de la Torre et al.* [2012], who found an occurrence frequency of 0.57 major SSW events per winter using four 51-year WACCM simulations with specified SSTs. The individual runs in that study had 0.45–0.69 major SSW events per winter. The occurrence frequencies are also slightly lower than those reported by *Marsh et al.* [2013]. They found an occurrence frequency that ranged from 0.33–0.53 major SSW events per winter using three 45-year WACCM simulations with an active ocean. The average for all three simulations was 0.46 major SSW events per winter.

There are also fewer major SSW events per winter in R1 and R2 than *Charlton and Polvani* [2007] found using reanalysis data from the National Centers for Environmental Prediction/National Center for Atmospheric Research (NCEP/NCAR) reanalysis and the European Center for Medium range Weather Forecasting 40-year reanalysis (ERA-40) for the period of time that the datasets overlap (45 NH winter seasons from November 1957 through March 2002). Using the algorithm described in section 4.3.1, they found 0.60 major SSW events per winter in the NCEP/NCAR reanalysis and 0.64 major SSW events per

winter in the ERA-40 reanalysis. However, *de la Torre et al.* [2012] found that a subset of NCEP/NCAR from 1960 to 1989 had only 0.47 major SSW events per winter.

Using the same four WACCM simulations that *de la Torre et al.* [2012] used and the algorithm described in section 4.3.2, *Chandran et al.* [2013] constructed a climatology of ES events in WACCM. They found an occurrence frequency of 0.32 ES events per winter, and the individual simulations ranged from 0.28–0.36 ES events per winter. *Chandran et al.* [2013] also applied their algorithm to 32 NH winters from 1979–2011 from the MERRA reanalysis dataset and found an occurrence frequency of 0.31 ES events per winter. The average number of ES events per winter for R1 and R2 combined (0.31 per winter) agrees with *Chandran et al.* [2013], although either R1 or R2 alone is outside of the range they found.

Figure 4.1 shows the monthly distribution of major SSW and ES events for the two simulations. The majority of major SSW events in R1 occurs in December, whereas the majority of major SSW events in R2 occurs in February and March. On average there are ∼0.12 December, ∼0.05 January, ∼0.12 February, and ∼0.08 March major SSW events per winter. The WACCM simulations used by *Marsh et al.* [2013] had, on average, 0.08 December, 0.15 January, 0.11 February, and 0.11 March major SSW events per winter, and the WACCM simulations used by *de la Torre et al.* [2012] had ∼0.17 December, ∼0.16 January, ∼0.13 February, and ∼0.09 March major SSW events per winter. *Charlton and Polvani* [2007] found an occurrence frequency of ∼0.1 December, ∼0.2 January, ∼0.17 February, and ∼0.11 March major SSW events per winter. The largest discrepancy in the simulations here compared to *Charlton and Polvani* [2007] is the frequency of January major SSW events.

The discrepancy in both the number of major SSW events and the monthly distribution compared to reanalysis might be explained by the specified SSTs used in the simulations here. For example, *Richter et al.* [2011] showed that a 29-year WACCM simulation with fixed SSTs had 0.5 major SSW events per winter, whereas a 29-year simulation for the same time period with an active ocean had 0.7 major SSW events per winter. This suggests that the way SSTs

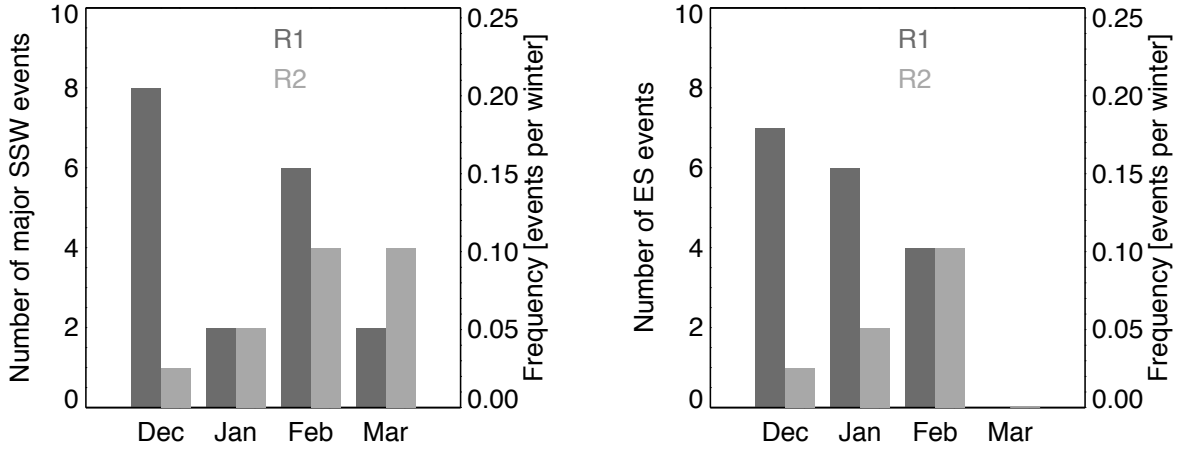

Figure 4.1: Monthly distribution of WACCM major SSW events (left) and ES events (right) for R1 and R2.

are handled might have an effect on major SSW event frequency. *Richter et al.* [2011] also found earlier major SSW event onset in the simulation with specified SSTs compared to the simulation with an active ocean. And, in fact, WACCM simulations with an active ocean described by *Marsh et al.* [2013] had a monthly distribution in better agreement with observations than the simulations here and the WACCM simulations in *de la Torre et al.* [2012]. For the purpose of this study, the exact frequency is not critical as long as the run is long enough to get enough major SSW events in each month.

In R1 ES events occur more frequently in December (∼0.18 per winter), followed by January (∼0.15 per winter) and February (∼0.1). The opposite trend is observed in R2: ∼0.03 December, ∼0.05 January, and ∼0.1 February ES events per winter. In the combined frequency of occurrence, ES events occur with equal frequency in each month. Again the exact frequency of ES events is not critical to this study.

4.4.2 Major SSW and ES Event Timing and Time Evolution of Polar NO_x

Figure 4.2 shows composite NO_x mixing ratios averaged poleward of 70°N (area-weighted) as a function of pressure and time for years with (a) no event, (b) a December event, (c) a January event, and (d) a February event. Winters from the two simulations were placed into one of the four categories. Only winters with a single event are considered here, where an event is either (1) a major SSW event without an ES event, (2) an ES event without a major SSW event, or (3) a SSW-ES event. Winters that have more than one event (e.g., a major SSW event in December and an ES event in February) are not considered. We have also discarded winters with a minor warming within 60 days of the event. There are 42 winters in (a), 8 winters in (b), 6 winters in (c), and 8 winters in (d). The day of the event is marked with a red line, where the day of the event is defined as follows. For a major SSW event occurring alone or an SSW-ES event, the day of the event is the central warming date of the major SSW event. For an ES event occurring without a major SSW event, the day of the event is the central date of the ES event minus 8 days to account for the lag of

the ES event with respect to the reversal of the zonal mean zonal wind. This has been done to make the events comparable. We chose 8 days because this is the average time between the central date of a major SSW event and the central date of an ES event for an SSW-ES event.

The tongue of descending NO_x takes on a different appearance depending on the month of occurrence of the event. A December event has the largest influence on the magnitude and extent in altitude of the NO_x tongue. The 12 ppbv contour line (shown in black) almost reaches 1.0 hPa, whereas in the other composites it remains up at ∼0.1 hPa. During the event, the black contour line is pushed up in altitude compared to that in Figure 4.2a, indicating upwelling. Following the event, the black contour line extends further down in altitude compared to Figure 4.2a, indicating enhanced downwelling.

Figure 4.3 shows the percent difference between years with (a) December, (b) January, and (c) February events and years with no event. The black contours show where the vertical component of the residual, or transformed Eulerian mean (TEM), circulation ($\overline{w}^*$) is more than ±50% (+ =solid; − =dotted) different than it is in the case without an event. Here $\overline{w}^*$ is positive for upwelling and negative for downwelling. The increases in NO_x usually correspond to the increases in descent, and the decreases in NO_x usually correspond to decreases in descent. In all cases, around the time of the event there is a decrease in NO_x above ∼0.8 hPa (upper stratosphere and mesosphere) and an increase in NO_x below ∼0.8 hPa (middle stratosphere). This is a result of the changes in the TEM circulation during the event. *Smith et al.* [2011] show that the TEM in WACCM during a SSW-ES event has a strong poleward and downward component at ∼1 hPa and an equatorward and upward component at ∼0.1 hPa. This reflects the large EP flux convergence near the level of the maximum zonal mean zonal wind deceleration during a major SSW event, which leads to cooling and induced upwelling above and warming and induced downwelling below that level [*Matsuno*, 1971; *Holton*, 1983]. Therefore, the increase in NO_x below ∼0.8 hPa during the event is largely caused by the influx of lower latitude air with higher NO_x mixing ratios,

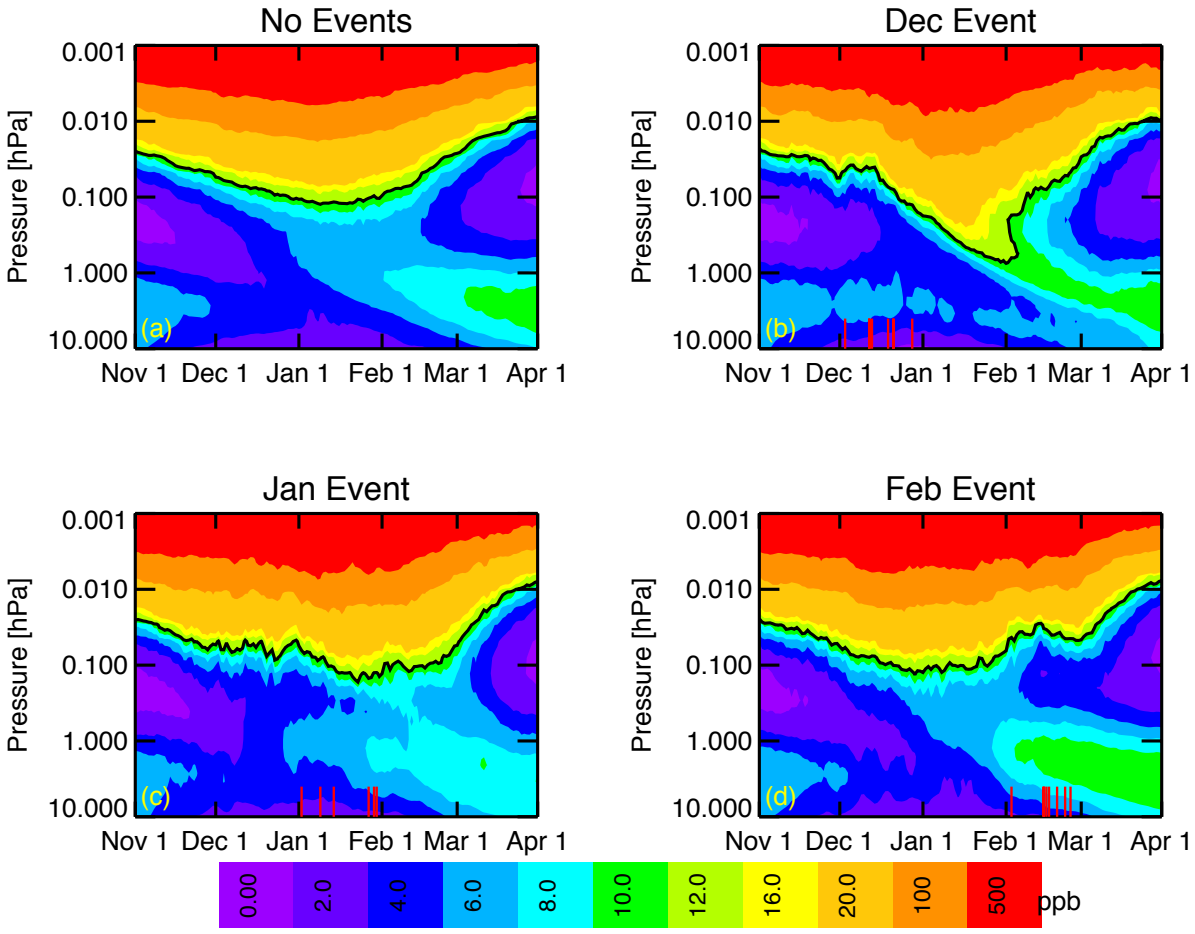

Figure 4.2: WACCM NO_x poleward of 70°N (area-weighted) as a function of pressure and time. These are composites for years with (a) no event, (b) a December event, (c) a January event, and (d) a February event. Red lines show the day of the event for the individual years in each composite.

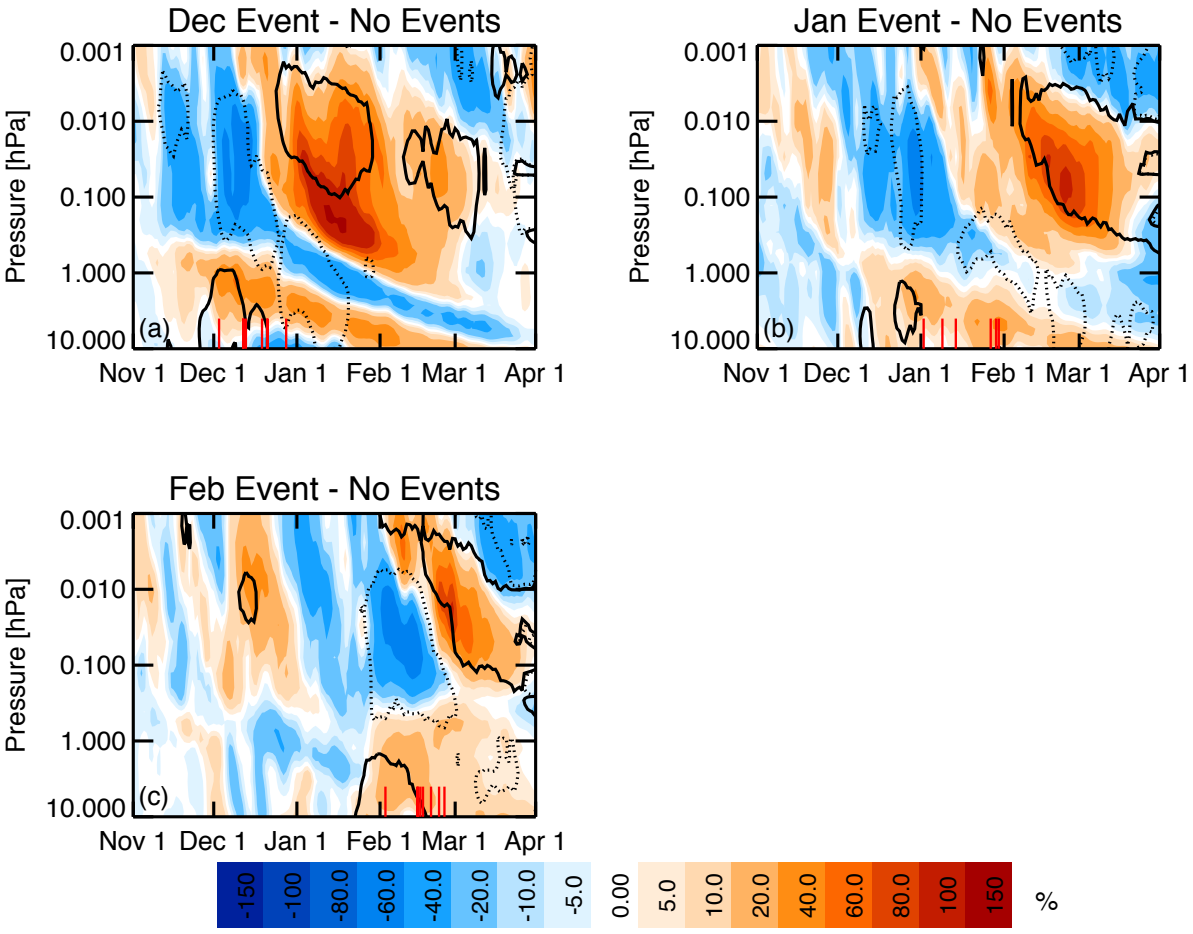

Figure 4.3: NO_x % difference between composites with (a) December, (b) January, and (c) February events and years with no event. The solid black contour is a 50% change and the dotted black contour is a -50% change in $\overline{w}^*$. Red lines show the day of the event for the individual years in each composite.

and the decrease in NO_x above ∼0.8 hPa during the event is caused by the upwelling and divergence in the mesosphere that reverses the normal winter downwelling. This is supported by the evolution of NO_x in the latitude-pressure plane during an event (not shown). The anomalies propagate downward over time following the event.

After the event, there is an increase in NO_x as the vortex reforms (not shown) and $\overline{w}^*$ strengthens. The largest NO_x increase is in the winters with a December event, the second largest is in the winters with a January event, and the smallest increase is in the winters with a February event. The NO_x increases following the later events are confined to higher altitudes; namely, the increase in NO_x following the event reaches well below 1.0 hPa in Figure 4.3a, just above 1.0 hPa in Figure 4.3b, and just below 0.1 hPa in Figure 4.3c.

The spread of the timing of the events, even when grouped by month of occurrence, is sufficient to wash out the descending tongue of NO_x in the monthly composites. Figure 4.4 shows NO_x mixing ratios averaged poleward of 70°N (area-weighted) as a function of pressure and time for individual model years with different event timings. It shows a year with (a) no major SSW or ES event, (b) a December major SSW event, (c) a January ES event, and (d) a February major SSW-ES event. We note that in Figure 4.4c conditions for a major SSW event were almost met, viz., the winds almost became easterly (they reach a minimum of ∼1.7 m/s) at 60°N and 10 hPa. The descent of NO_x is interrupted during the major event and resumes, often at a faster rate than before the event as indicated by the steeper slope of the contour lines, after the warming ends. Figure 4.4 confirms what Figures 4.2 and 4.3 show: that the timing of the major event impacts the descent of NO_x in the manner described above.

4.4.3 Quantification of Major SSW and ES Event Effects on the EPP IE

To quantify the impact of major SSW and ES events on the descent of EPP-NO_x in WACCM, we first quantify the amount of EPP-NO_x in gigamoles (Gmol) descending to the stratosphere each NH winter season using the method described in *Holt et al.* [2012]. We

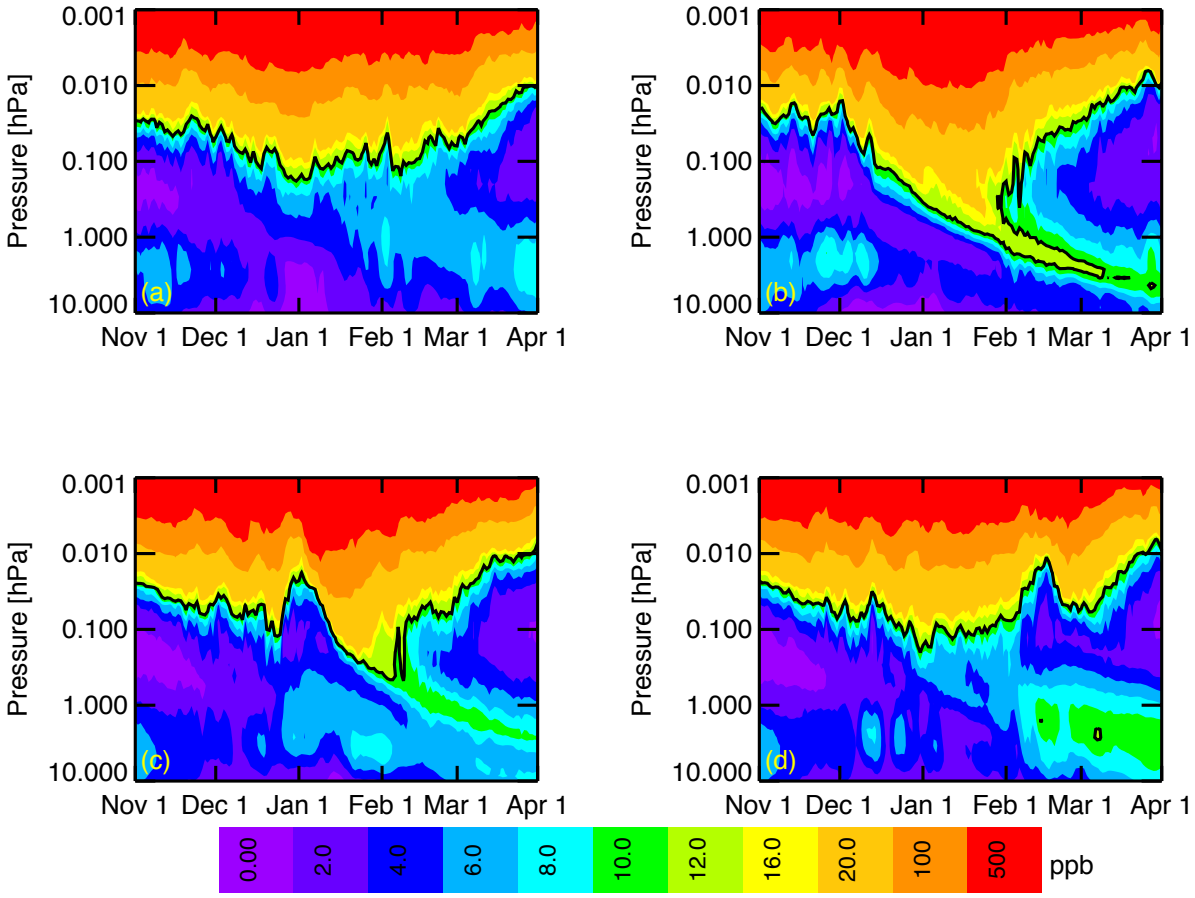

Figure 4.4: WACCM NO_x poleward of 70°N (area-weighted) for an individual winter with (a) no major SSW or ES event, (b) a December major SSW event, (c) a January ES event, and (d) a February major SSW-ES event.

briefly outline the method here. First, in order to separate the portion of NO_x that is created by EPP we use the relationship between NO_x and CH_4. In the polar winter upper stratosphere, NO_x and CH_4 are positively correlated since they are both decreasing with increasing altitude. This relationship remains true unless there is a source of NO_x, and the only source of NO_x in the polar winter upper stratosphere is EPP. Therefore, EPP-NO_x can be identified as an anti-correlation between NO_x and CH_4. This method of identifying stratospheric EPP-NO_x transported from the upper atmosphere was first described by *Siskind and Russell* [1996]. Once we identify the EPP-NO_x density at a particular level (in Gmol per m^3), we determine the daily flux of EPP-NO_x (in Gmol per day) through that level by multiplying by the area occupied by the EPP-NO_x and $\overline{w}^*$ at that level. We then sum the daily flux over November 1 to March 31 to get the total number of Gmol per NH winter across the chosen level.

Figure 4.5 shows the flux of EPP-NO_x in Gmol per day across three levels in WACCM for years with (a) no event, (b) a December event, (c) a January event, and (d) a February event. The three levels shown here are 0.41 hPa ($\sim$ 52 km, black line), 0.73 hPa ($\sim$ 47 km, dark grey line), and 1.24 hPa ($\sim$ 43 km, light grey line). The largest flux of EPP-NO_x into the stratosphere at all levels by far happens in winters with a December event. Winters with a January event also have a larger EPP IE than winters with no event. The EPP-NO_x flux for winters with a February event is similar to the winters with no event, except that the flux in February is interrupted by the event. The winters with a December or January event are also the only winters for which any significant amount of EPP-NO_x is transported to the lower levels (light grey). The EPP IE at 1.24 hPa is nonzero for a small number of dynamically calm winters (not shown) but the magnitude is much smaller (a factor of $\sim$ 58).

Table 4.2 compares the EPP IE at 0.41 hPa, 0.73 hPa, and 1.24 hPa, as defined by the average amount of EPP-NO_x descending across each level, for winters with no major SSW or ES event, winters with an event, and winters with a SSW-ES event only. The breakdown month of event and SSW-ES event is also shown. The largest EPP IE at 0.41 hPa for a

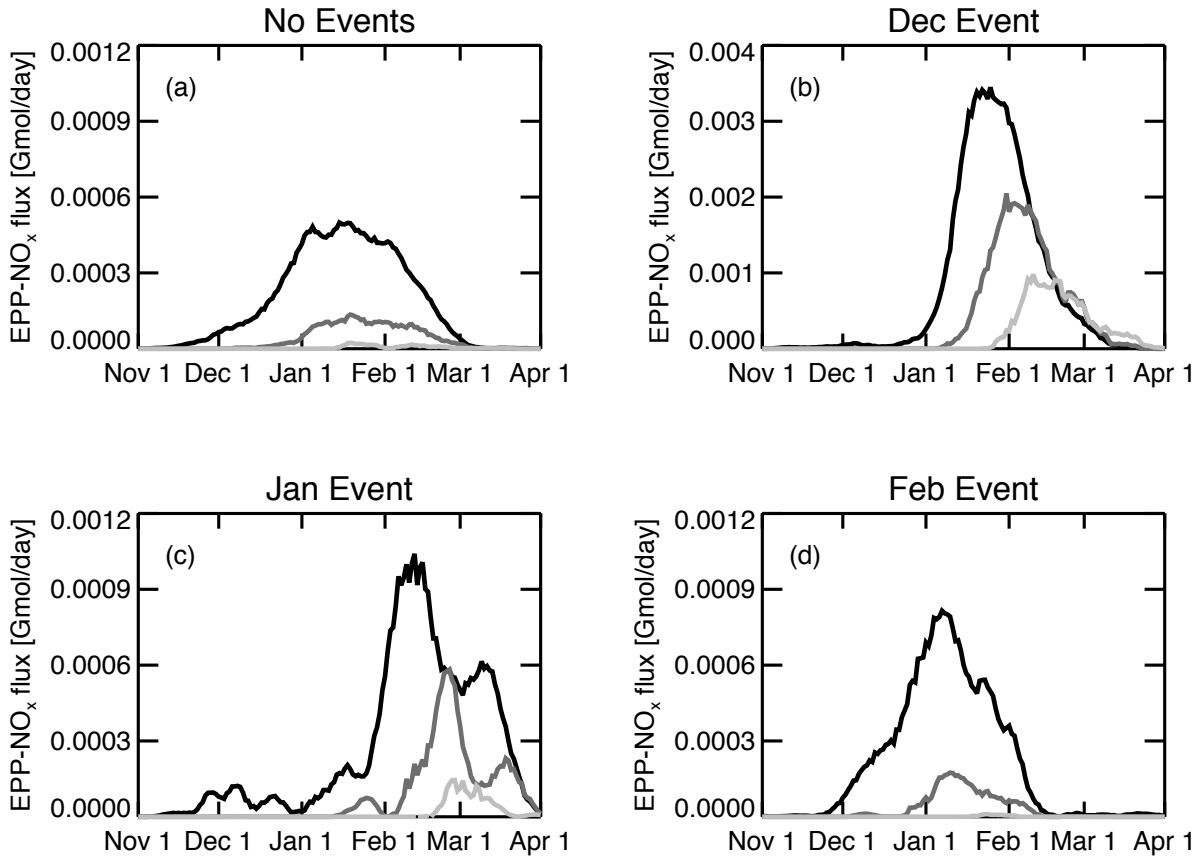

Figure 4.5: WACCM flux of EPP-NO_x in Gmol per day across 0.41 hPa (black line), 0.73 hPa (dark grey line), and 1.24 hPa (light grey line). These are composites for years with (a) no event, (b) a December event, (c) a January event, and (d) a February event. Note the different scale in (b).

Table 4.2: Average Gmol EPP-NO_x across three levels for winters with no major SSW or ES event, winters with a major SSW and/or ES event, and winters with a SSW-ES event only. The number of winters in each category is shown in brackets. Maximum values shown in parentheses.

	0.41 hPa	0.73 hPa	1.24 hPa
No event [44]	**0.027 (0.073)**	**0.0054 (0.030)**	**0.00053 (0.0081)**
All events [27]	**0.056 (0.16)**	**0.022 (0.13)**	**0.0084 (0.062)**
Dec [8]	0.11 (0.16)	0.058 (0.13)	0.026 (0.062)
Jan [6]	0.041 (0.072)	0.013 (0.027)	0.0023 (0.0088)
Feb [8]	0.031 (0.063)	0.0045 (0.014)	0.00011 (0.00064)
Mar [5]	0.022 (0.046)	0.0035 (0.014)	0.00016 (0.0008)
SSW-ES events only [13]	**0.074 (0.16)**	**0.032 (0.13)**	**0.014 (0.062)**
Dec [6]	0.11 (0.16)	0.062 (0.13)	0.031 (0.062)
Jan [3]	0.042 (0.072)	0.012 (0.027)	0.0014 (0.0041)
Feb [4]	0.034 (0.063)	0.0026 (0.0085)	0.0000029 (0.000012)

winter without an event is 0.073 Gmol compared to 0.16 Gmol for a winter with a SSW-ES event. On average, the largest EPP IE occurs in winters with a SSW-ES event. The average EPP IE at 0.41 hPa for winters with a SSW-ES event is ∼3 times larger than the EPP IE for winters with no event. At the lower level (1.24 hPa), the average EPP IE for winters with a SSW-ES event is ∼26 times larger than the average EPP IE for winters with no event. In winters with an event, the largest EPP IE at all levels occurs when the event happens in December, followed by January, February, and March; i.e., in general, the earlier the event, the larger the EPP IE. In fact, the maximum EPP IE for winters with no event is larger than the maximum EPP IE for winters with an event when the event occurs after December, and the average EPP IE for winters with no event is similar to the average EPP IE for February and March events. The maximum EPP IE for winters with no event occurs for a dynamically calm winter with only one minor SSW event at the end of February.

The relationship between the timing of the major event and the EPP IE (the total amount of EPP-NO_x descending across each level over the entire winter) is shown in Figure 4.6. The left panels (a-c) show the EPP IE for all events; i.e., the EPP IE from winters that formed the composites in Figure 4.2 (b-d). The right panels (d-f) show the EPP IE for

winters with a SSW-ES only. There is a strong anti-correlation between the amount of EPP-NO_x and the central warming date, especially for SSW-ES events. Similar relationships exist between central warming date and maximum NO_x mixing ratios at each level (not shown). The years that have the largest EPP IE are years in which a major SSW event took place in December and, in all but one year, was followed by an ES event. The relationship between the timing of a SSW-ES event and the amount of EPP-NO_x crossing each level is slightly stronger than the relationship between the timing of all events and the amount of EPP-NO_x crossing each level. SSW-ES events are more likely to occur earlier in the season. This figure also shows that to get significant EPP-NO_x across the 1.24 hPa level requires an early (December or early January) SSW-ES event. EPP-NO_x descending past this level increases the likelihood that O_3 will be destroyed through the NO_x catalytic cycle, which becomes important below ∼45 km.

4.4.4 Major SSW and ES Event Timing and Dynamics

Figure 4.7 shows the zonal mean pole to equator temperature difference (ΔT) as a function of pressure and time for years with (a) no event, (b) a December, (c) a January, and (d) a February event. Here we define ΔT as the difference between T averaged poleward of 70°N and T averaged between 0° and 30°N: $T(\phi > 70°\text{N})$–$T(0°\text{N} < \phi < 30°\text{N})$, where ϕ is latitude. There is a large decrease in ΔT following the event around 1 hPa, which corresponds to a larger equator-to-pole temperature gradient. The largest response is in years with a December event, followed by years with a January event.

Figure 4.8 shows the zonal mean zonal wind (U), the momentum tendency due to gravity waves (dU/dt_{GW}), $\overline{w}^*$ (i-l), and T as a function of pressure and time for the different cases shown in Figures 4.2, 4.3, and 4.7. The middle atmosphere response to the event depends on the month of occurrence of the event. Following the event, in response to the change in ΔT, the winds between ∼1.0 and 0.1 hPa (upper stratosphere-lower mesosphere) become westerly again and are stronger than before the event. The strongest winds occur in

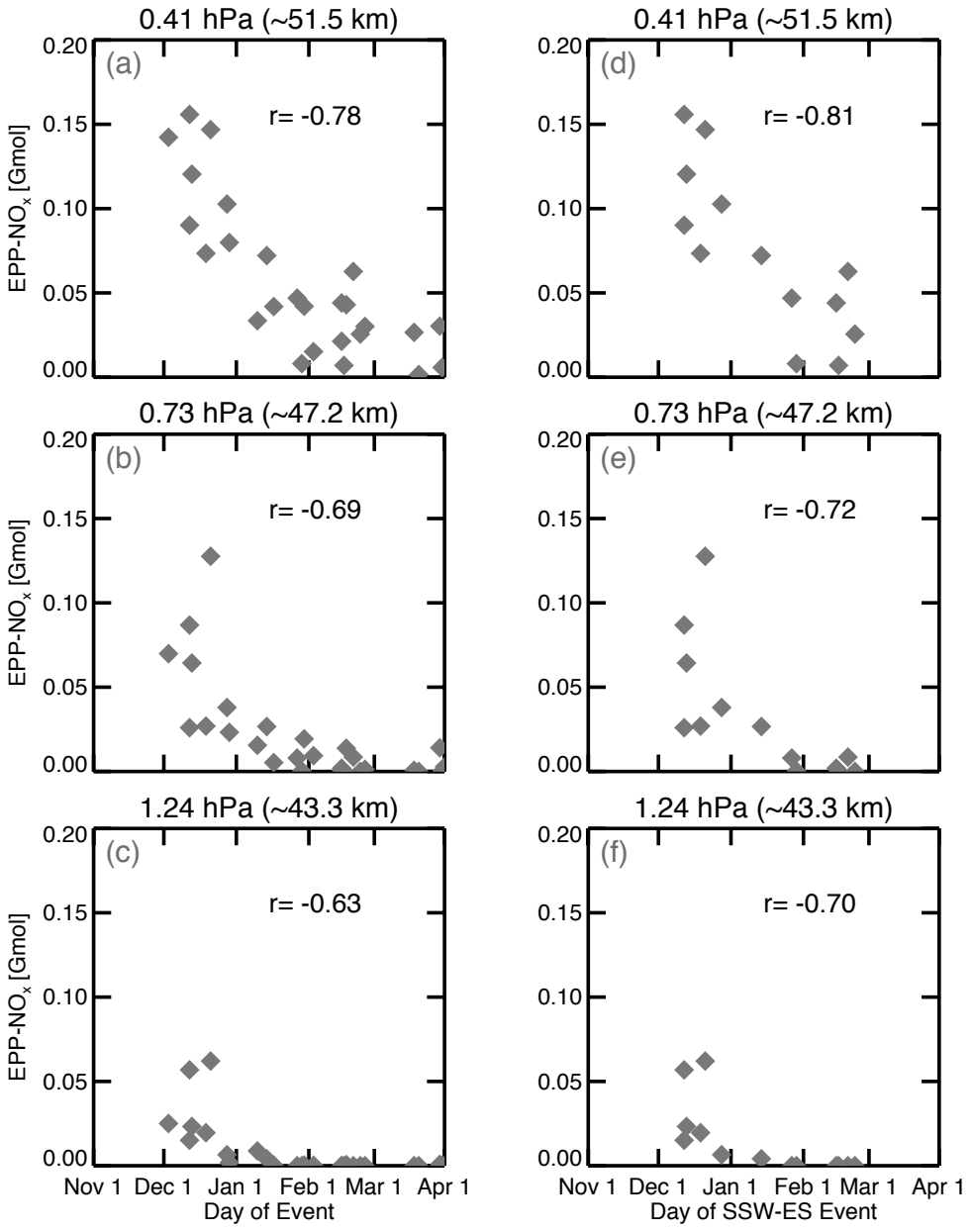

Figure 4.6: WACCM EPP IE (total Gmol EPP-NO_x crossing each level for entire season) versus the central date of the event (a-c) and central date of the SSW-ES event (d-f) for three levels.

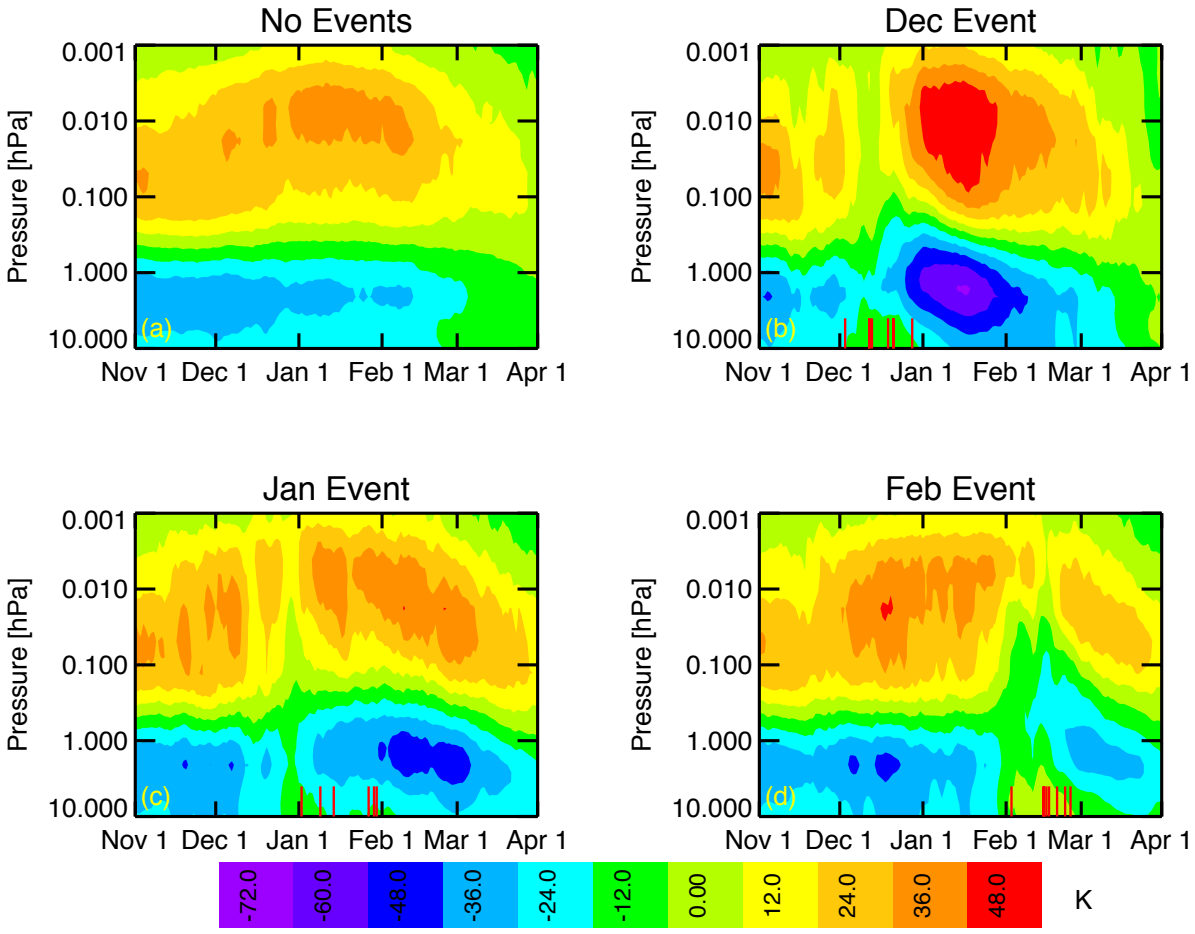

Figure 4.7: Zonal mean ΔT ($T(\phi > 70°\text{N})$–$T(0°\text{N} < \phi < 30°\text{N})$) as a function of pressure and time for years with (a) no event, (b) a December event, (c) a January event, and (d) a February event. Red lines show the day of the event for the individual years in each composite.

the December composite (b), followed by January and February; i.e., the earlier the event occurs, the more westerly the winds are afterward. The relationship between timing of the event and the strength of the response is mirrored in the other variables: following the major event, dU/dt_{GW} is more negative (easterly), $\overline{\mathrm{w}}^*$ is more negative (descent), and the stratopause is elevated.

In the stratosphere, planetary waves drive the stratosphere away from radiative equilibrium. Following a major SSW event, the stratosphere above the zero-wind line (critical layer) is relaxed to radiative equilibrium in the absence of planetary waves [e.g., *Hauchecorne et al.*, 2007; *Liu et al.*, 2009; *Manney et al.*, 2005; *Siskind et al.*, 2010]. What Figure 4.8 shows is that the closer to solstice the event happens, the faster the upper stratospheric winds are (largest ΔT from equator to pole) during the recovery. This in turn affects GW filtering and $\overline{\mathrm{w}}^*$ in such a way that the earlier the event, the stronger $\overline{\mathrm{w}}^*$ is. Additionally, since the perturbations due to the event are stronger the earlier the event occurs, earlier major SSW events are more likely to produce an ES event.

Figure 4.9 shows the maximum U at $\sim$0.6 hPa (left), the maximum westward (most negative) dU/dt_{GW} at $\sim$0.03 hPa (center), and the maximum descent (most negative $\overline{\mathrm{w}}^*$) at $\sim$0.08 hPa (right) following the event as a function of the day of the event (as defined in Section 3.6). The earlier in the season the event, the larger the maximum westerly U, the larger the westward dU/dt_{GW} and, ultimately, the stronger the descent following the event. Therefore, the EPP IE is larger for earlier central warming dates for two main reasons: (1) the earlier in the winter season, the larger (more negative) $\overline{\mathrm{w}}^*$ is following the event, and (2) the earlier an event occurs in the season, the longer the EPP-NO_x descends before the final warming and the less chance that EPP-NO_x is photochemically destroyed during transport.

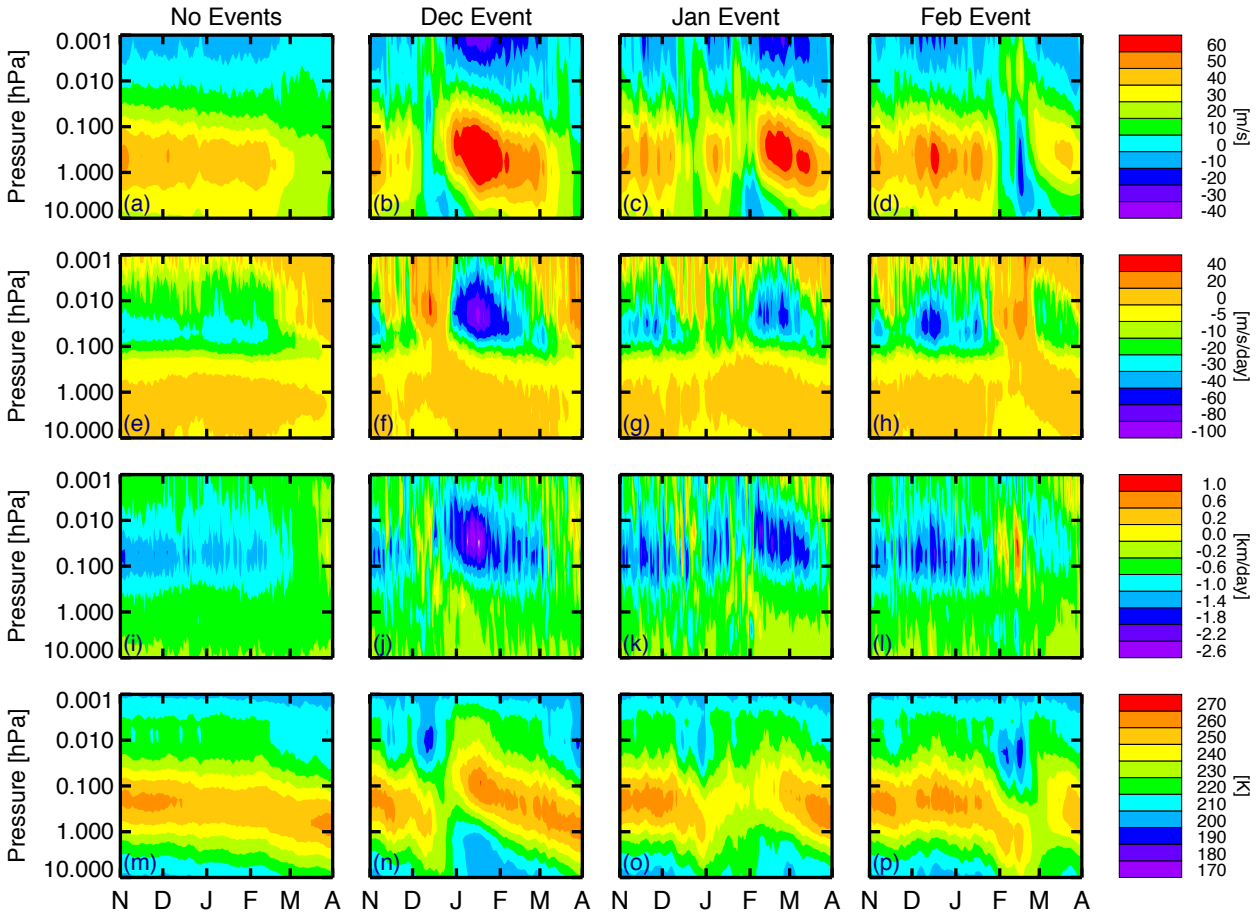

Figure 4.8: WACCM U (a-d), dU/dt_{GW} (e-h), $\overline{w}^*$ (i-l) and T (m-p) as a function of pressure and time for years with no event (first column), a December event (second column), a January event (third column), and a February event (fourth column). U and dU/dt_{GW} are averaged from 50-70°N (area-weighted) and $\overline{w}^*$ and T are averaged poleward of 70°N (area-weighted).

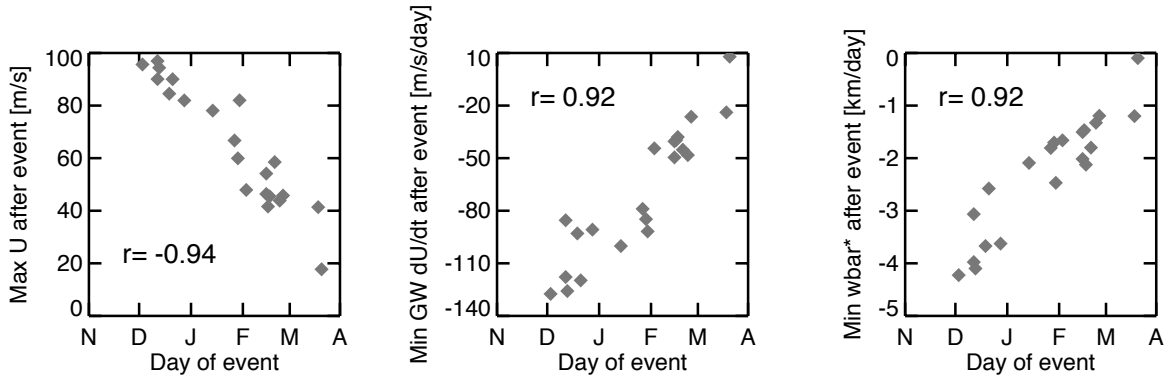

Figure 4.9: Maximum U at ∼0.6 hPa (left), the maximum westward (most negative) dU/dt_{GW} at ∼0.03 hPa (center), and the maximum descent (most negative $\overline{w}^*$) at ∼0.08 hPa (right) following the event as a function of the day of the event.

4.5 Summary and Conclusions

We have used WACCM to study the effects of major SSW and ES events on the EPP IE in the NH polar winter. The EPP IE refers to NO_x that is produced by EPP in the mesosphere and/or thermosphere and is transported to the stratosphere during polar winter. WACCM is a useful tool with which to study the EPP IE because it is possible to keep the level of EPP constant in order to isolate the effects of major SSW and ES events on the EPP IE.

We quantified the EPP IE as the amount of EPP-NO_x descending across three WACCM levels in the upper stratosphere. The results here suggest that the seasonal timing of an event is an extremely important factor controlling the EPP IE: the earlier in the season the event occurs, the more EPP-NO_x is brought down and the lower in altitude the EPP IE extends. We found that the winters with the largest EPP IE are the ones with a December major SSW followed by an ES event. Similar relationships were shown between the timing of the event and the dynamical response of the middle atmosphere. We concluded that the EPP IE is larger for earlier central warming dates for two main reasons: (1) the earlier in the winter season, the larger (more negative) $\overline{w}^*$ is following the major event, and (2) the earlier an event occurs in the season, the longer the EPP-NO_x descends before the final warming and the less chance that EPP-NO_x is photochemically destroyed during transport.

On average, the EPP IE in winters with an event is larger than the EPP IE in winters with no event; however, in dynamically calm winters the EPP IE can exceed the EPP IE in years with a January, February, or March event. This is because the steady descent of EPP-NO_x is not interrupted in dynamically calm winters, whereas in winters with a major event later in the season the normal descent is interrupted and the increase in descent after the event is too small and too late in the season to make up for it. We also found that the EPP IE at the 1.24 hPa level ($\sim$43 km) for winters with a SSW-ES event is $\sim$26 times higher than it is for winters with no event and $\sim$58 times higher when the SSW-ES happens

in December. This is relevant because the NO_x catalytic cycle becomes important below ∼45 km.

Overall, our results fit well with the picture of the EPP IE that we have from observations. For instance, the NH 2003–2004 EPP IE was by far the largest EPP-NO_x enhancement ever observed, and a SSW-ES event took place on 2 January 2004 [*Manney et al.*, 2005]; however, the level of EPP was relatively high before and during the SSW-ES. The A_p index was ∼10.8 for the second half of December 2003 and ∼19.7 for the first half of January 2004. The SSW-ES events in the 2005–2006 and 2008–2009 NH winters had central warming dates on 21 and 24 January, respectively [*Manney et al.*, 2009a]. The EPP IE in 2005–2006 and 2008–2009 was not nearly as large as in 2003–2004, although the comparison is complicated by the fact that the level of EPP was also lower (∼8.5 in January 2006 and ∼4.3 in January 2009). Additionally, the descending tongue of EPP-NO_x reached lowest in altitude in 2004, followed by 2006 [*Randall et al.*, 2009], which is consistent with what WACCM shows: the earlier the warming, the lower in altitude the EPP-NO_x extends.

A major discrepancy between the WACCM runs used here and observations is that WACCM underestimates the magnitude of the EPP IE compared to observations. *Holt et al.* [2012] estimated the EPP IE in the 2003–2004 NH winter to be 2.3–2.7 Gmol across 2000 K, which is ∼20 times larger than the largest EPP IE at 0.73 hPa (∼2000 K) in the WACCM runs here. The average A_p index for December 2003–January 2004 was ∼16.6, so the discrepancy cannot be attributed to the level of auroral EPP. This corroborates the results of *Smith et al.* [2011], who found that NO_x mixing ratios in the winter with largest EPP IE out of four 53-year free-running WACCM simulations were still lower than observed NO_x mixing ratios in the 2008–2009 NH winter. They suggest possible mechanisms for the discrepancy: (1) the poleward branch of the residual circulation in WACCM is too low in altitude, and/or (2) the eddy or molecular diffusion is not strong enough in WACCM. The latter is a topic of current research. Additionally, some of the discrepancy might be explained by the lack of higher energy particle populations (e.g., solar protons, relativistic electrons,

and medium energy electrons) in WACCM.

Chapter 5

Closing Remarks

This thesis contributes to our understanding of the effects of EPP on the atmosphere by advancing our knowledge of the EPP IE in the following ways:

- ⋆ The EPP IE observed by LIMS in 1978–1979 is similar to the EPP IE observed by MIPAS and ACE-FTS in the Arctic winters of 2002–2003, 2004–2005, 2006–2007, and 2007–2008 [*Holt et al.*, 2012]. This suggests that the lack of reported EPP-NO_x descending to the NH stratosphere in the 1980s and 1990s was most likely due to a lack of appropriate measurements.

- ⋆ *Holt et al.* [2012] presents a method for quantifying the EPP IE that can be utilized when no tracer measurements are available.

- ⋆ Observations of NH winters with major SSW events (2003–2004, 2005–2006, and 2008–2009) show large increases in EPP-NO_x, but in 2005–2006 and 2008–2009 the EPP IE was confined to the upper stratosphere. The major SSW events occurred later in the season in 2005–2006 and 2008–2009 than in 2003–2004 [*Holt et al.*, 2012]. This suggests that the timing of the descent is highly significant for the EPP IE. This hypothesis was investigated with WACCM in *Holt et al.* [2013].

- ⋆ The EPP IE is very sensitive to the GW tuning in WACCM. The current GW tuning is not optimal and the work here underlines the need for an improved treatment of GWs in models.

- ⋆ WACCM simulations suggest that the timing of major SSW and/or ES events is a major factor controlling the NH EPP IE [*Holt et al.*, 2013]. The earlier the event occurs, the larger the EPP IE.

This thesis highlights the need for future measurements of NO_x, O_3, and tracers throughout the MLT in the polar winter. Particularly, NO and tracer observations in the MLT are desirable to address the vertical distribution of EPP-NO_x sources and transport mechanisms. Global MLT wind observations would also be very helpful for understanding the transport mechanisms. At the time of this writing, ACE-FTS is the only satellite instrument measuring NO_x in the polar middle atmosphere. ACE-FTS is a solar occultation instrument and has serious limitations for studying the EPP IE: it only makes measurements during the day and it has limited geographical coverage.

Going forward, the relationship between the timing of major SSW and/or ES events and the EPP IE should be explored further in observations and additional modeling studies. The importance of other transport parameters, such as diffusion, should also be explored with modeling studies. Additional questions inspired by the results presented in this thesis are:

- ⋆ Does the type of major SSW event (vortex displacement versus splitting) influence the effect of event timing on the EPP IE?
- ⋆ To what extent does the size and strength of the polar vortex influence the descent after a major SSW event?
- ⋆ Why do ES events happen after some major SSW events and not others?
- ⋆ Will the timing and/or frequency of major SSW events change with climate?
- ⋆ Can we define major SSW and ES events in a more meaningful way based on underlying mechanisms?

In addition to these, several open questions pertaining to the EPP IE in general remain. Some of the most pressing are:

- ⋆ What is the temporal and spatial distribution of EPP-NO_x sources?
- ⋆ What are the populations of energetic particles that contribute most to the production of EPP-NO_x?
- ⋆ How is EPP-NO_x transported from the MLT to the stratosphere?
- ⋆ How is EPP-NO_x redistributed in the atmosphere?
- ⋆ Does source or dynamics play a larger role in determining the inter-hemispheric differences?
- ⋆ What are the important coupling mechanisms?
- ⋆ How will the EPP IE change with a changing climate?
- ⋆ Does the EPP IE affect surface temperatures and, if so, how?

Bibliography

Andrews, D. G., and M. E. McIntyre (1976), Planetary waves in horizontal and vertical shear–Asymptotic theory for equatorial waves in weak shear, *Journal of the Atmospheric Sciences*, *33*, 2049–2053.

Axford, W. I., and C. O. Hines (1961), A unifying theory of high-latitude geophysical phenomena and geomagnetic storms, *Canadian Journal of Physics*, *39*(10), 1433–1464, doi: 10.1139/p61-172.

Baker, D. N. (2002), How to cope with space weather, *Science*, *297*, 1486–1487, doi: 10.1126/science.1074956.

Baldwin, M. P., T. Hirooka, A. O'Neill, and S. Yoden (2003), Major stratospheric warming in the Southern Hemisphere in 2002: Dynamical aspects of the ozone hole split, *SPARC Newsletter*, *20*, 24–26.

Baldwin, M. P., M. Dameris, and T. G. Shepherd (2007), How will the stratosphere affect climate change?, *Science*, *316*, 1576–1577, doi:10.1126/science.1144303.

Balogh, A., J. T. Gosling, J. R. Jokipii, R. Kallenbach, and H. Kunow (1999), *Corotating Interaction Regions*, Space Sciences Series of ISSI, Springer.

Banks, P. M., and G. Kockarts (1973), *Aeronomy*, 355 pp., Academic Press.

Barth, C. A., K. D. Mankoff, S. M. Bailey, and S. C. Solomon (2003), Global observations of nitric oxide in the thermosphere, *Journal of Geophysical Research*, *108*(A1), 1027, doi: 10.1029/2002JA009458.

Bates, D. R., and P. B. Hays (1967), Atmospheric nitrous oxide, *Planetary and Space Science*, *15*, 189–197.

Bauer, E. (1979), A catalog of perturbing influences on stratospheric ozone, 1955–1975, *Journal of Geophysical Research*, *84*(C11), 6929, doi:10.1029/JC084iC11p06929.

Baumgaertner, A. J. G., P. Jöckel, and C. Brühl (2009), Energetic particle precipitation in ECHAM5/MESSy1–Part 1: Downward transport of upper atmospheric NO_x produced by low energy electrons, *Atmospheric Chemistry and Physics*, *9*, 2729–2740.

Baumgaertner, A. J. G., A. Seppälä, P. Jöckel, and M. A. Clilverd (2011), Geomagnetic activity related NO_x enhancements and polar surface air temperature variability in a chemistry climate model: modulation of the NAM index, *Atmospheric Chemistry and Physics*, *11*(9), 4521–4531, doi:10.5194/acp-11-4521-2011.

Bernath, P. F., et al. (2005), Atmospheric Chemistry Experiment (ACE): Mission overview, *Geophysical Research Letters*, *32*, L15S01, doi:10.1029/2005GL022386.

Boone, C. D., R. Nassar, K. A. Walker, Y. Rochon, S. D. McLeod, C. P. Rinsland, and P. F. Bernath (2005), Retrievals for the atmospheric chemistry experiment Fourier-transform spectrometer, *Applied Optics*, *44*(33), 7218–7231.

Brasseur, G. P., and S. Solomon (2005), *Aeronomy of the Middle Atmosphere*, 3rd rev. ed., 646 pp., Springer, Dordrecht.

Callis, L. B. (1997), Odd nitrogen formed by energetic electron precipitation as calculated from TIROS data, *Geophysical Research Letters*, *24*(24), 3237–3240.

Callis, L. B., and J. D. Lambeth (1998), NO_y formed by precipitating electron events in 1991 and 1992: Descent into the stratosphere as observed by ISAMS, *Geophysical Research Letters*, *25*(11), 1875–1878.

Callis, L. B., D. N. Baker, J. B. Blake, J. D. Lambeth, R. E. Boughner, M. Natarajan, R. W. Klebesadel, and D. J. Gorney (1991), Precipitating relativistic electrons: Their long-term effect on stratospheric odd nitrogen levels, *Journal of Geophysical Research*, *96*(D2), 2939–2976.

Callis, L. B., et al. (1996), Precipitating electrons: Evidence for effects on mesospheric odd nitrogen, *Geophysical Research Letters*, *23*(15), 1901–1904.

Callis, L. B., M. Natarajan, D. S. Evans, and J. D. Lambeth (1998a), Solar atmospheric coupling by electrons (SOLACE) 1. Effects of the May 12, 1997 solar event on the middle atmosphere, *Journal of Geophysical Research*, *103*(D21), 28,405–28,419.

Callis, L. B., M. Natarajan, J. D. Lambeth, and D. N. Baker (1998b), Solar atmospheric coupling by electrons (SOLACE) 2. Calculated stratospheric effects of precipitating electrons, 1979–1988, *Journal of Geophysical Research*, *103*(D21), 28,421–28,438.

Chandran, A., R. L. Collins, R. R. Garcia, D. R. Marsh, V. L. Harvey, J. Yue, and L. de la Torre (2013), A climatology of elevated stratopause events in the whole atmosphere community climate model, *Journal of Geophysical Research Atmospheres*, *118*, doi:10.1002/jgrd.50123.

Chapman, S. (1930), A theory of upper atmosphere ozone, *Quart. J. Roy. Meteorol. Soc.*, *3*, 103.

Charlton, A. J., and L. M. Polvani (2007), A new look at stratospheric sudden warmings. Part I: Climatology and modeling benchmarks, *Journal of Climate*, *20*, 449–469.

Charney, J. G., and P. G. Drazin (1961), Propagation of planetary-scale disturbances from the lower into the upper atmosphere, *Journal of Geophysical Research*, *66*(1), 83–109.

Cleary, D. D. (1985), Analysis of nitric oxide fluorescence bands from high latitude observations of the thermospheric dayglow, Ph.D. thesis, Univsersity of Colorado.

Clilverd, M. A., A. Seppälä, C. J. Rodger, P. T. Verronen, and N. R. Thomson (2006), Ionospheric evidence of thermosphere-to-stratosphere descent of polar NO_x, *Geophysical Research Letters*, *33*, L19811, doi:10.1029/2006GL026727.

Codrescu, M. V., T. J. Fuller-Rowell, R. G. Roble, and D. S. Evans (1997), Medium energy particle precipitation influences on the mesosphere and lower thermosphere, *Journal of Geophysical Research*, *102*(A9), 19,977–19,987.

Cohen, R. C., and J. G. Murphy (2003), Photochemistry of NO_2 in Earth's stratosphere: Constraints from observations, *Chemical Reviews*, *103*, 4985–4998.

Crutzen, P. J. (1969), Determination of parameters appearing in the "dry" and the "wet" photochemical theories for ozone in the stratosphere, *Tellus*, *21*(3), 368–388, doi: 10.1111/j.2153-3490.1969.tb00450.x.

Crutzen, P. J. (1970), The influence of nitrogen oxides on the atmospheric ozone content, *Quarterly Journal of the Royal Meteorological Society*, *96*, 320–325.

Crutzen, P. J. (1971), Ozone production rates in an oxygen-hydrogen-nitrogen oxide atmosphere, *Journal of Geophysical Research*, *76*(30), 7311–7327.

Crutzen, P. J. (1972), SST's–A Threat the Earth's ozone shield, *Ambio*, *1*(2), 41–51.

Crutzen, P. J. (1974), A review of upper atmospheric photochemistry, *Canadian Journal of Chemistry*, *52*, 1569–1581.

Crutzen, P. J. (1979), The role of NO and NO_2 in the chemistry of the troposphere and stratosphere, *Annual Review of Earth and Planetary Sciences*, *7*, 443–472.

Crutzen, P. J., I. S. A. Isaksen, and G. C. Reid (1975), Solar proton events: Stratospheric sources of nitric oxide, *Science*, *189*(4201), 457–459.

de la Torre, L., R. R. Garcia, D. Barriopedro, and A. Chandran (2012), Climatology and characteristics of stratospheric sudden warmings in the Whole Atmosphere Community Climate Model, *Journal of Geophysical Research*, *117*, D04110, doi:10.1029/2011JD016840.

de Mazière, M., et al. (2008), Validation of ACE-FTS v2.2 methane profiles from the upper troposphere to the lower mesosphere, *Atmospheric Chemistry and Physics*, *8*, 2421–2435.

Degenstein, D. A., N. D. Lloyd, A. E. Bourassa, R. L. Gattinger, and E. J. Llewellyn (2005), Observations of mesospheric ozone depletion during the October 28, 2003 solar proton event by OSIRIS, *Geophysical Research Letters*, *32*, L03S11, doi:10.1029/2004GL021521.

Dungey, J. W. (1961), Interplanetary magnetic field and the auroral zones, *Physical Review Letters*, *6*(2), 6–7.

Dunkerton, T. (1978), On the mean meridional mass motions of the stratosphere and mesosphere, *Journal of the Atmospheric Sciences*, *35*, 2325.

Dunkerton, T. J. (1991), LIMS (Limb Infrared Monitor of the Stratosphere) observation of traveling planetary waves and potential vorticity advection in the stratosphere and mesosphere, *Journal of Geophysical Research*, *96*(D2), 2813–2834, doi:10.1029/90JD02340.

Eather, R. H., and S. B. Mende (1971), Airborne observations of auroral precipitation patterns, *Journal of Geophysical Research*, *76*(7), 1746–1755.

Fischer, H., et al. (2008), MIPAS: An instrument for atmospheric and climate research, *Atmospheric Chemistry and Physics*, *8*, 2151–2188.

Forbush, S. E., T. B. Stinchcomb, and M. Schein (1950), The extraordinary increase of cosmic-ray intensity on November 19, 1949, *Physical Review*, *79*(3), 501–505.

Frederick, J. E. (1976), Solar corpuscular emission and neutral chemistry in the Earth's middle atmosphere, *Journal of Geophysical Research*, *81*, 3179–3186, doi: 10.1029/JA081i019p03179.

Frederick, J. E., and N. Orsini (1982), The distribution and variability of mesospheric odd nitrogen: A theoretical investigation, *Journal of Atmospheric and Terrestrial Physics*, *44*(6), 479–488.

Frederick, J. E., R. B. Abrams, and P. J. Crutzen (1983), The delta band dissociation of nitric oxide: A potential mechanism for coupling thermospheric variations to the mesosphere and stratosphere, *Journal of Geophysical Research*, *88*(C6), 3829–3835.

Funke, B., M. López-Puertas, S. Gil-López, T. von Clarmann, G. P. Stiller, H. Fischer, and S. Kellmann (2005a), Downward transport of upper atmospheric NO_x into the polar stratosphere and lower mesosphere during the Antarctic 2003 and Arctic 2002/2003 winters, *Journal of Geophysical Research*, *110*, D24308, doi:10.1029/2005JD006463.

Funke, B., et al. (2005b), Retrieval of stratospheric NO_x from 5.3 and 6.2 μm nonlocal thermodynamic equilibrium emissions measured by Michelson Interferometer for Passive Atmospheric Sounding (MIPAS) on Envisat, *Journal of Geophysical Research*, *110*, D09302, doi:10.1029/2004JD005225.

Gabriel, A., D. Peters, I. Kirchner, and H.-F. Graf (2007), Effect of zonally asymmetric ozone on stratospheric temperature and planetary wave propagation, *Geophysical Research Letters*, *34*, L06807, doi:10.1029/2006GL028998.

Garcia, R. R. (1991), Parameterization of planetary wave breaking in the middle atmosphere, *Journal of the Atmospheric Sciences*, *48*(11), 1405–1419.

Garcia, R. R. (1992), Transport of thermospheric NO_x to the stratosphere and mesosphere, *Advances in Space Research*, *12*(10), 57–66.

Garcia, R. R., and S. Solomon (1983), A numerical model of the zonally averaged dynamical and chemical structure of the middle atmosphere, *Journal of Geophysical Research*, *88*(C2), 1379–1400.

Garcia, R. R., and S. Solomon (1985), The effect of breaking gravity waves on the dynamics and chemical composition of the mesosphere and lower thermosphere, *Journal of Geophysical Research*, *90*(D2), 3850–3868.

Garcia, R. R., and S. Solomon (1994), A new numerical model of the middle atmosphere 2. Ozone and related species, *Journal of Geophysical Research*, *99*(D6), 12,937–12,951.

Garcia, R. R., D. R. Marsh, D. E. Kinnison, B. A. Boville, and F. Sassi (2007), Simulation of secular trends in the middle atmosphere, 1950–2003, *Journal of Geophysical Research*, *112*, D09301, doi:10.1029/2006JD007485.

Gérard, J. C., and C. A. Barth (1977), High-latitude nitric oxide in the lower thermosphere, *Journal of Geophysical Research*, *82*(4), 674–680.

Gille, J. C., and J. M. Russell, III (1984), The Limb Infrared Monitor of the Stratosphere: Experiment description, performance, and results, *Journal of Geophysical Research*, *89*(D4), 5125–5140.

Gopalswamy, N., L. Barbieri, G. Lu, S. P. Plunkett, and R. M. Skoug (2005), Introduction to the special section: Violent Sun-Earth connection events of October–November 2003, *Geophysical Research Letters*, *32*, L03S01, doi:10.1029/2005GL022348.

Greenblatt, J. B., et al. (2002), Tracer-based determination of vortex descent in the 1999/2000 Arctic winter, *Journal of Geophysical Research*, *107*(D20), 5843–5853, doi: 10.1029/2001JD000937.

Gylvan Meira, L., Jr. (1971), Rocket measurements of upper atmospheric nitric oxide and their consequences to the lower ionosphere, *Journal of Geophysical Research*, *76*(1), 202–212.

Hampson, J. (1965), *Chemiluminescent Emissions Observed in the Stratosphere and Mesosphere*, CARDE technical note, 75 pp., Canadian Armament Research and Development Establishment.

Harvey, V. L., R. B. Pierce, T. D. Fairlie, and M. H. Hitchman (2002), A climatology of stratospheric polar vortices and anticyclones, *Journal of Geophysical Research*, *107*(D20), 4442, doi:10.1029/2001JD001471.

Hauchecorne, A., J.-L. Bertaux, F. Dalaudier, J. M. Russell, III, M. G. Mlynczak, E. Kyrölä, and D. Fussen (2007), Large increase of NO_2 in the north polar

mesosphere in January–February 2004: Evidence of a dynamical origin from GOMOS/ENVISAT and SABER/TIMED data, *Geophysical Research Letters*, *34*, L03810, doi:10.1029/2006GL027628.

Haynes, P. H. (2005), Stratospheric dynamics, *Annual Review of Fluid Mechanics*, *37*, 263–293, doi:10.1146/annurev.fluid.37.061903.175710.

Heath, D. F., A. J. Krueger, and P. J. Crutzen (1977), Solar proton event: Influence on stratospheric ozone., *Science*, *197*, 886–889, doi:10.1126/science.197.4306.886.

Holt, L. A., C. E. Randall, V. L. Harvey, E. E. Remsberg, G. P. Stiller, B. Funke, P. F. Bernath, and K. A. Walker (2012), Atmospheric effects of energetic particle precipitation in the Arctic winter 1978–1979 revisited, *Journal of Geophysical Research*, *117*, D05315, doi:10.1029/2011JD016663.

Holt, L. A., C. E. Randall, E. D. Peck, D. R. Marsh, A. K. Smith, and V. L. Harvey (2013), The influence of major sudden stratospheric warmings and elevated stratopause events on the epp ie, *Journal of Geophysical Research*, submitted.

Holton, J. R. (1982), The role of gravity wave induced drag and diffusion in the momentum budget of the mesosphere, *Journal of the Atmospheric Sciences*, *39*, 791–799.

Holton, J. R. (1983), The influence of gravity wave breaking on the general circulation of the middle atmosphere, *Journal of the Atmospheric Sciences*, *40*, 2497–2507.

Holton, J. R. (2004), *Introduction to Dynamic Meteorology*, 4 ed., 535 pp., Elsevier, San Diego.

Horne, R. B., M. M. Lam, and J. C. Green (2009), Energetic electron precipitation from the outer radiation belt during geomagnetic storms, *Geophysical Research Letters*, *36*, L19104, doi:10.1029/2009GL040236.

Hunt, B. G. (1966), The need for a modified photochemical theory of the ozonesphere, *Journal of the Atmospheric Sciences*, *23*, 88–95.

Hurrell, J. W., J. J. Hack, D. Shea, J. M. Caron, and J. Rosinski (2008), A new sea surface temperature and sea ice boundary dataset for the Community Atmosphere Model, *Journal of Climate*, *21*, 5145–5153, doi:10.1175/2008JCLI2292.1.

Jackman, C. H., and E. L. Fleming (2008), Stratospheric ozone variations caused by solar proton events between 1963 and 2005, in *Climate Variability and Extremes during the Past 100 Years*, edited by S. Brönnimann, pp. 333–345, Springer.

Jackman, C. H., and P. E. Meade (1988), Effect of solar proton events in 1978 and 1979 on the odd nitrogen abundance in the middle atmosphere, *Journal of Geophysical Research*, *93*(D6), 7084–7090.

Jackman, C. H., A. R. Douglass, R. B. Rood, R. D. Mcpeters, and P. E. Meade (1990), Effect of solar proton events on the middle atmosphere during the past two solar cycles as computed using a two-dimensional model, *Journal of Geophysical Research*, *95*(D6), 7417–7428.

Jackman, C. H., M. T. DeLand, G. J. Labow, E. L. Fleming, D. K. Weisenstein, M. K. W. Ko, M. Sinnhuber, and J. M. Russell, III (2005), Neutral atmospheric influences of the solar proton events in October–November 2003, *Journal of Geophysical Research*, *110*, A09S27, doi:10.1029/2004JA010888.

Jin, J. J., et al. (2005), Co-located ACE-FTS and Odin/SMR stratospheric-mesospheric CO 2004 measurements and comparison with a GCM, *Geophysical Research Letters*, *32*, L15S03, doi:10.1029/2005GL022433.

Johnston, H. (1971), Reduction of stratospheric ozone by nitrogen oxide catalysts from supersonic transport exhaust, *Science*, *173*, 518–522.

Johnston, H. (1972), Newly recognized vital nitrogen cycle, *Proceedings of the National Academy of Sciences of the United States of America*, *69*(9), 2369–72.

Johnston, H. S., G. Written, and J. Birks (1973), Effect of nuclear explosions on stratospheric nitric oxide and ozone, *Journal of Geophysical Research*, *78*(27), 6107–6135.

Kar, J., et al. (2007), Initial comparison of ozone and NO_2 profiles from ACE-MAESTRO with balloon and satellite data, *Journal of Geophysical Research*, *112*, D16301, doi: 10.1029/2006JD008242.

Kerzenmacher, T., et al. (2008), Validation of NO_2 and NO from the Atmospheric Chemistry Experiment (ACE), *Atmospheric Chemistry and Physics*, *8*, 5801–5841.

Kinnison, D. E., et al. (2007), Sensitivity of chemical tracers to meteorological parameters in the MOZART-3 chemical transport model, *Journal of Geophysical Research*, *112*, D20302, doi:10.1029/2006JD007879.

Krüger, K., B. Naujokat, and K. G. Labitzke (2005), The unusual midwinter warming in the Southern Hemisphere stratosphere 2002 : A comparison to Northern Hemisphere phenomena, *Journal of the Atmospheric Sciences*, *62*, 603–614.

Kunz, A., L. L. Pan, P. Konopka, D. E. Kinnison, and S. Tilmes (2011), Chemical and dynamical discontinuity at the extratropical tropopause based on START08 and WACCM analyses, *Journal of Geophysical Research*, *116*, doi:10.1029/2011JD016686.

Labitzke, K. G. (1981), The amplification of height wave 1 in January 1979: A characteristic precondition for the major warming in February, *Monthly Weather Review*, *109*, 983–989.

Labitzke, K. G., and B. Naujokat (2000), The lower arctic stratosphere in winter since 1952, *SPARC Newsletter*, *15*, 11–14.

Labitzke, K. G., and H. van Loon (1999), *The Stratosphere: Phenomena, History and Relevance*, 179 pp., Springer.

Langematz, U., J. L. Grenfell, K. Matthes, P. Mieth, M. Kunze, B. Steil, and C. Brühl (2005), Chemical effects in 11-year solar cycle simulations with the Freie Universität Berlin Climate Middle Atmosphere Model with online chemistry (FUB-CMAM-CHEM), *Geophysical Research Letters*, *32*, L13803, doi:10.1029/2005GL022686.

Lean, J., G. Rottman, J. Harder, and G. Kopp (2005), SORCE contributions to new understanding of global change and solar variability, *Solar Physics*, *230*, 27–53.

Lindzen, R. S. (1981), Turbulence and stress owing to gravity wave and tidal breakdown, *Journal of Geophysical Research*, *86*(C10), 9707–9714.

Liu, Y., C. X. Liu, H. P. Wang, X. X. Tie, S. T. Gao, D. E. Kinnison, and G. P. Brasseur (2009), Atmospheric tracers during the 2003–2004 stratospheric warming event and impact of ozone intrusions in the troposphere, *Atmospheric Chemistry and Physics*, *9*, 2157–2170, doi:10.5194/acp-9-2157-2009.

López-Puertas, M., B. Funke, S. Gil-López, T. von Clarmann, G. P. Stiller, M. Höpfner, S. Kellmann, H. Fischer, and C. H. Jackman (2005a), Observation of NO_x enhancement and ozone depletion in the Northern and Southern Hemispheres after the October–November 2003 solar proton events, *Journal of Geophysical Research*, *110*, A09S43, doi:10.1029/2005JA011050.

López-Puertas, M., et al. (2005b), HNO_3, N_2O_5, and $ClONO_2$ enhancements after the October–November 2003 solar proton events, *Journal of Geophysical Research*, *110*, A09S44, doi:10.1029/2005JA011051.

López-Puertas, M., B. Funke, T. von Clarmann, H. Fischer, and G. P. Stiller (2006), The stratospheric and mesospheric NO_y in the 2002–2004 polar winters as measured by MIPAS/ENVISAT, *Space Science Reviews*, *125*, 403–416, doi:10.1007/s11214-006-9073-2.

Lossow, S., J. Urban, H. Schmidt, D. R. Marsh, J. Gumbel, P. Eriksson, and D. P. Murtagh (2009), Wintertime water vapor in the polar upper mesosphere and lower thermosphere: First satellite observations by Odin submillimeter radiometer, *Journal of Geophysical Research*, *114*, doi:10.1029/2008JD011462.

Lu, H., M. A. Clilverd, A. Seppälä, and L. L. Hood (2008), Geomagnetic perturbations on stratospheric circulation in late winter and spring, *Journal of Geophysical Research*, *113*, D16106, doi:10.1029/2007JD008915.

Manney, G. L., R. W. Zurek, A. O'Neill, and R. Swinbank (1994), On the motion of air through the stratospheric polar vortex, *Journal of the Atmospheric Sciences*, *51*(20), 2973–2994.

Manney, G. L., K. Krüger, J. L. Sabutis, S. A. Sena, and S. Pawson (2005), The remarkable 2003–2004 winter and other recent warm winters in the Arctic stratosphere since the late 1990s, *Journal of Geophysical Research*, *110*, D04107, doi:10.1029/2004JD005367.

Manney, G. L., et al. (2008), The evolution of the stratopause during the 2006 major warming: Satellite data and assimilated meteorological analyses, *Journal of Geophysical Research*, *113*, D11115, doi:10.1029/2007JD009097.

Manney, G. L., M. J. Schwartz, K. Krüger, M. L. Santee, S. Pawson, J. N. Lee, W. H. Daffer, R. A. Fuller, and N. J. Livesey (2009a), Aura Microwave Limb Sounder observations of dynamics and transport during the record-breaking 2009 Arctic stratospheric major warming, *Geophysical Research Letters*, *36*, L12815, doi:10.1029/2009GL038586.

Manney, G. L., et al. (2009b), Satellite observations and modeling of transport in the upper troposphere through the lower mesosphere during the 2006 major stratospheric sudden warming, *Atmospheric Chemistry and Physics*, *9*, 4775–4795.

Marsh, D. R. (2011), Chemical-dynamical coupling in the mesosphere and lower thermosphere, in *Aeronomy of the Earth's Atmosphere and Ionosphere*, edited by M. A. Abdu and D. Pancheva, chap. 1, pp. 3–17, Springer Science + Business Media B. V. 2011, Dordrecht, doi:10.1007/978-94-007-0326-1.

Marsh, D. R., and R. G. Roble (2002), TIME-GCM simulations of lower-thermospheric nitric oxide seen by the halogen occultation experiment, *Journal of Atmospheric and Solar-Terrestrial Physics*, *64*, 889–895.

Marsh, D. R., S. C. Solomon, and A. E. Reynolds (2004), Empirical model of nitric oxide in the lower thermosphere, *Journal of Geophysical Research*, *109*, doi:10.1029/2003JA010199.

Marsh, D. R., R. R. Garcia, D. E. Kinnison, B. A. Boville, F. Sassi, S. C. Solomon, and K. Matthes (2007), Modeling the whole atmosphere response to solar cycle changes in radiative and geomagnetic forcing, *Journal of Geophysical Research*, *112*, D23306, doi:10.1029/2006JD008306.

Marsh, D. R., M. J. Mills, D. E. Kinnison, J.-f. Lamarque, N. Calvo, and L. M. Polvani (2013), Climate change from 1850 to 2005 simulated in CESM1(WACCM), *Journal of Climate*, in press.

Matsuno, T. (1971), A dynamical model of the stratospheric sudden warming, *Journal of the Atmospheric Sciences*, *28*, 1479–1494, doi:10.1175/1520-0469(1971)028¡1479:ADMOTS¿2.0.CO;2.

McElroy, M. B., and J. C. McConnell (1971), Nitrous oxide: A natural source of stratospheric NO, *Journal of Atmospheric Sciences*, *28*(6), 1095–1098.

McElroy, M. B., S. C. Wofsy, J. E. Penner, and J. C. McConnell (1974), Atmospheric ozone: Possible impact of stratospheric aviation, *Journal of the Atmospheric Sciences*, *31*, 287–303.

McElroy, M. B., J. W. Elkins, S. C. Wofsy, and Y. L. Yung (1976), Sources and sinks for atmospheric N_2O, *Reviews of Geophysics and Space Physics*, *14*(2), 143–150.

McFarlane, N. A. (1987), The effect of orographically excited gravity wave drag on the general circulation of the lower stratosphere and troposphere, *Journal of the Atmospheric Sciences*, *44*(14), 1775–1800.

McHugh, M., B. Magill, K. A. Walker, C. D. Boone, P. F. Bernath, and J. M. Russell, III (2005), Comparison of atmospheric retrievals from ACE and HALOE, *Geophysical Research Letters*, *32*, L15S10, doi:10.1029/2005GL022403.

Mengistu Tsidu, G., et al. (2005), NO_y from Michelson Interferometer for Passive Atmospheric Sounding on Environmental Satellite during the Southern Hemisphere polar vortex split in September/October 2002, *Journal of Geophysical Research*, *110*, D11301, doi: 10.1029/2004JD005322.

Mewaldt, R. A., et al. (2005), Proton, helium, and electron spectra during the large solar particle events of October–November 2003, *Journal of Geophysical Research*, *110*, A09S18, doi:10.1029/2005JA011038.

Narcisi, R. S., C. R. Philbrick, J. C. Ulwick, and M. E. Gardner (1972), Mesospheric nitric-oxide concentrations during a PCA, *Journal of Geophysical Research*, *77*(7), 1332–1336.

Natarajan, M., E. E. Remsberg, L. E. Deaver, and J. M. Russell, III (2004), Anomalously high levels of NO_x in the polar upper stratosphere during April, 2004: Photochemical consistency of HALOE observations, *Geophysical Research Letters*, *31*, L15113, doi: 10.1029/2004GL020566.

Neale, R. B., et al. (2010), Description of the NCAR Community Atmosphere Model (CAM 5.0), *Tech. rep.*, National Center for Atmospheric Research, Boulder, CO.

Newell, P. T., T. Sotirelis, and S. Wing (2009), Diffuse, monoenergetic, and broadband aurora: The global precipitation budget, *Journal of Geophysical Research*, *114*, doi: 10.1029/2009JA014326.

Nicolet, M. (1970), The origin of nitric oxide in the terrestrial atmosphere, *Planetary and Space Science*, *18*, 1111–1118.

Nicolet, M. (1971), Aeronomic reactions of hydrogen and ozone, in *Mesospheric Models and Related Experiments*, vol. 25, edited by G. Fiocco, pp. 1–51, Springer Netherlands.

Nicolet, M. (1972), Aeronomic chemistry of the stratosphere, *Planetary and Space Science*, *20*, 1671–1702.

Nicolet, M. (1975), Stratospheric ozone: An Introduction to its study, *Reviews of Geophysics and Space Physics*, *13*(5), 593–636.

Norton, W., and E. Shuckburgh (2000), The stratospheric circulation: a personal history, by Alan Brewer, in *Report on the Brewer-Dobson Workshop, Dec. 13–15, 1999*, SPARC Newsletter, 15.

Orsolini, Y. J., G. L. Manney, M. L. Santee, and C. E. Randall (2005), An upper stratospheric layer of enhanced HNO_3 following exceptional solar storms, *Geophysical Research Letters*, *32*, L12S01, doi:10.1029/2004GL021588.

Pulkkinen, T. (2007), Space weather: Terrestrial perspective, *Living Reviews in Solar Physics*, *4*, 1–60.

Randall, C. E., D. W. Rusch, R. M. Bevilacqua, K. W. Hoppel, and J. D. Lumpe (1998), Polar Ozone and Aerosol Measurement (POAM) II stratospheric NO_2, *Journal of Geophysical Research*, *103*(D21), 28,361–28,371.

Randall, C. E., D. E. Siskind, and R. M. Bevilacqua (2001), Stratospheric NO_x enhancements in the southern hemisphere vortex in winter/spring of 2000, *Geophysical Research Letters*, *28*(12), 2385–2388.

Randall, C. E., et al. (2005), Stratospheric effects of energetic particle precipitation in 2003–2004, *Geophysical Research Letters*, *32*(5), L05802, doi:10.1029/2004GL022003.

Randall, C. E., V. L. Harvey, C. S. Singleton, P. F. Bernath, C. D. Boone, and J. U. Kozyra (2006), Enhanced NO_x in 2006 linked to strong upper stratospheric Arctic vortex, *Geophysical Research Letters*, *33*, L18811, doi:10.1029/2006GL027160.

Randall, C. E., V. L. Harvey, C. S. Singleton, S. M. Bailey, P. F. Bernath, M. V. Codrescu, H. Nakajima, and J. M. Russell, III (2007), Energetic particle precipitation effects on the Southern Hemisphere stratosphere in 1992–2005, *Journal of Geophysical Research*, *112*, D08308, doi:10.1029/2006JD007696.

Randall, C. E., V. L. Harvey, D. E. Siskind, J. France, P. F. Bernath, C. D. Boone, and K. A. Walker (2009), NO_x descent in the Arctic middle atmosphere in early 2009, *Geophysical Research Letters*, *36*(18), L18811, doi:10.1029/2009GL039706.

Randall, C. E., E. D. Peck, V. L. Harvey, L. A. Holt, X. Fang, M. J. Mills, D. R. Marsh, C. H. Jackman, and B. Funke (2013), Auroral energetic particle precipitation: An atmospheric coupling agent?, *Journal of Geophysical Research*, submitted.

Raspollini, P., et al. (2006), MIPAS level 2 operational analysis, *Atmospheric Chemistry and Physics*, *6*, 5605–5630.

Reagan, J. B., R. E. Meyerott, R. W. Nightingale, R. C. Gunton, R. G. Johnson, J. E. Evans, W. L. Imhof, D. F. Heath, and A. J. Krueger (1981), Effects of the August 1972 solar particle events on stratospheric ozone, *Journal of Geophysical Research*, *86*(A3), 1473–1494.

Reames, D. V. (1999), Particle acceleration at the sun and in the heliosphere, *Space Science Reviews*, *90*, 413–491.

Reddmann, T., R. Ruhnke, S. Versick, and W. Kouker (2010), Modeling disturbed stratospheric chemistry during solar-induced NO_x enhancements observed with MIPAS/ENVISAT, *Journal of Geophysical Research*, *115*, D00I11, doi: 10.1029/2009JD012569.

Remsberg, E. E., L. L. Gordley, B. T. Marshall, R. E. Thompson, J. Burton, P. Bhatt, V. L. Harvey, G. Lingenfelser, and M. Natarajan (2004), The Nimbus 7 LIMS version 6 radiance conditioning and temperature retrieval methods and results, *Journal of Quantitative Spectroscopy and Radiative Transfer*, *86*, 395–424, doi:10.1016/j.jqsrt.2003.12.007.

Remsberg, E. E., M. Natarajan, B. T. Marshall, L. L. Gordley, R. E. Thompson, and G. Lingenfelser (2010), Improvements in the profiles and distributions of nitric acid and nitrogen dioxide with the LIMS version 6 dataset, *Atmospheric Chemistry and Physics*, *10*, 4741–4756, doi:10.5194/acp-10-4741-2010.

Richards, P. G. (2004), On the increases in nitric oxide density at midlatitudes during ionospheric storms, *Journal of Geophysical Research*, *109*, doi:10.1029/2003JA010110.

Richardson, I. G., E. W. Cliver, and H. V. Cane (2000), Sources of geomagnetic activity over the solar cycle: Relative importance of coronal mass ejections, high-speed streams, and slow solar wind, *Journal of Geophysical Research*, *105*, 18,203–18,213, doi: 10.1029/1999JA000400.

Richter, J. H., F. Sassi, and R. R. Garcia (2010), Toward a physically based gravity wave source parameterization in a general circulation model, *Journal of the Atmospheric Sciences*, *67*, 136–156, doi:10.1175/2009JAS3112.1.

Richter, J. H., K. Matthes, N. Calvo, and L. J. Gray (2011), Influence of the quasi-biennial oscillation and El Niño–Southern Oscillation on the frequency of sudden stratospheric warmings, *Journal of Geophysical Research*, *116*, D20111, doi:10.1029/2011JD015757.

Rienecker, M. M., et al. (2011), MERRA: NASA's Modern-Era Retrospective Analysis for Research and Applications, *Journal of Climate*, *24*, 3624–3648, doi:10.1175/JCLI-D-11-00015.1.

Rinsland, C. P., et al. (1996), ATMOS measurements of H_2O+2CH_4 and total reactive nitrogen in the November 1994 Antarctic stratosphere: Dehydration and denitrification in the vortex, *Geophysical Research Letters*, *23*(17), 2397–2400.

Rinsland, C. P., et al. (1999), Polar stratospheric descent of NO_y and CO and Arctic denitrification during winter 1992–1993, *Journal of Geophysical Research*, *104*(D1), 1847–1861.

Rinsland, C. P., C. D. Boone, R. Nassar, K. A. Walker, P. F. Bernath, J. C. McConnell, and L. Chiou (2005), Atmospheric Chemistry Experiment (ACE) Arctic stratospheric measurements of NO_x during February and March 2004: Impact of intense solar flares, *Geophysical Research Letters*, *32*, L16S05, doi:10.1029/2005GL022425.

Roble, R. G. (1995), Energetics of the mesosphere and thermosphere, in *The Upper Mesosphere and Lower Thermosphere: A Review of Experiment and Theory*, *Geophys. Monogr. Ser.*, vol. 87, edited by R. M. Johnson and T. L. Killeen, pp. 1–21, AGU, Washington, DC, doi:10.1029/GM087p0001.

Roble, R. G., and E. C. Ridley (1987), An auroral model for the NCAR thermospheric general circulation model (TGCM), *Annales Geophysicae*, *5A*(6), 369–382.

Roble, R. G., and E. C. Ridley (1994), A thermosphere-ionosphere-mesosphere-electrodynamics general circulation model (TIME-GCM): Equinox solar cycle minimum simulations (30-500 km), *Geophysical Research Letters*, *21*(6), 417–420.

Rohen, G., et al. (2005), Ozone depletion during the solar proton events of October/November 2003 as seen by SCIAMACHY, *Journal of Geophysical Research*, *110*, A09S39, doi:10.1029/2004JA010984.

Rozanov, E., L. B. Callis, M. Schlesinger, F. Yang, N. G. Andronova, and V. Zubov (2005), Atmospheric response to NO_y source due to energetic electron precipitation, *Geophysical Research Letters*, *32*, L14811, doi:10.1029/2005GL023041.

Rozanov, E., M. Calisto, T. Egorova, T. Peter, and W. Schmutz (2012), Influence of the precipitating energetic particles on atmospheric chemistry and climate, *Surveys in Geophysics*, *33*, 483–501, doi:10.1007/s10712-012-9192-0.

Rusch, D. W., J. C. Gérard, S. Solomon, P. J. Crutzen, and G. C. Reid (1981), The effect of particle precipitation events on the neutral and ion chemistry of the middle atmosphere–I. Odd nitrogen, *Planetary and Space Science*, *29*(7), 767–774.

Russell, J. M., III, L. L. Gordley, E. E. Remsberg, and L. B. Callis (1984), The variability of stratospheric and mesospheric NO_2 in the polar winter night observed by LIMS, *Journal of Geophysical Research*, *89*(D5), 7267–7275.

Ryan, J. M., J. A. Lockwood, and H. Debrunner (2000), Solar energetic particles, *Space Science Reviews*, *93*, 35–53.

Salmi, S. M., P. T. Verronen, L. Thölix, E. Kyrölä, L. Backman, A. Y. Karpechko, and A. Seppälä (2011), Mesosphere-to-stratosphere descent of odd nitrogen in February–March 2009 after sudden stratospheric warming, *Atmospheric Chemistry and Physics*, *11*, 4645–4655, doi:10.5194/acp-11-4645-2011.

Sassi, F., R. R. Garcia, B. A. Boville, and H.-L. Liu (2002), On temperature inversions and the mesospheric surf zone, *Journal of Geophysical Research*, *107*(D19), 4380, doi:10.1029/2001JD001525.

Scherhag, R. (1952), Die esplosionsartigen stratosphärenerwärmungen des spätwinters 1951/52, *Berichte des Deutschen Wetterdienstes in der US–Zone*, *6*(38), 51–63.

Semeniuk, K., V. I. Fomichev, J. C. McConnell, C. Fu, S. M. L. Melo, and I. G. Usoskin (2011), Middle atmosphere response to the solar cycle in irradiance and ionizing particle precipitation, *Atmospheric Chemistry and Physics*, *11*, 5045–5077, doi:10.5194/acp-11-5045-2011.

Seppälä, A., P. T. Verronen, E. Kyrölä, S. Hassinen, L. Backman, A. Hauchecorne, J.-L. Bertaux, and D. Fussen (2004), Solar proton events of October–November 2003: Ozone depletion in the Northern Hemisphere polar winter as seen by GOMOS/Envisat, *Geophysical Research Letters*, *31*, L19107, doi:10.1029/2004GL021042.

Seppälä, A., P. T. Verronen, M. A. Clilverd, C. E. Randall, J. Tamminen, V. F. Sofieva, L. Backman, and E. Kyrölä (2007a), Arctic and Antarctic polar winter NO_x and energetic particle precipitation in 2002–2006, *Geophysical Research Letters*, *34*, L12810, doi:10.1029/2007GL029733.

Seppälä, A., M. A. Clilverd, and C. J. Rodger (2007b), NO_x enhancements in the middle atmosphere during 2003–2004 polar winter: Relative significance of solar proton events and the aurora as a source, *Journal of Geophysical Research*, *112*, D23303, doi:10.1029/2006JD008326.

Seppälä, A., C. E. Randall, M. A. Clilverd, E. Rozanov, and C. J. Rodger (2009), Geomagnetic activity and polar surface air temperature variability, *Journal of Geophysical Research*, *114*, A10312, doi:10.1029/2008JA014029.

Sinnhuber, M., H. Nieder, and N. Wieters (2012), Energetic particle precipitation and the chemistry of the mesosphere/lower thermosphere, *Surveys in Geophysics*, *33*, 1281–1334, doi:10.1007/s10712-012-9201-3.

Siskind, D. E. (1994), On the radiative coupling between mesospheric and thermospheric nitric oxide, *Journal of Geophysical Research*, *99*(D11), 22,757–22,766.

Siskind, D. E., and J. M. Russell, III (1996), Coupling between middle and upper atmospheric NO: Constraints from HALOE observations, *Geophysical Research Letters*, *23*(2), 137–140.

Siskind, D. E., C. A. Barth, D. S. Evans, and R. G. Roble (1989), The response of thermospheric nitric oxide to an auroral storm 2. Auroral latitudes, *Journal of Geophysical Research*, *94*(A12), 899–911.

Siskind, D. E., J. T. Bacmeister, M. E. Summers, and J. M. Russell, III (1997), Two-dimensional model calculations of nitric oxide transport in the middle atmosphere and comparison with Halogen Occultation Experiment data, *Journal of Geophysical Research*, *102*(D3), 3527–3545.

Siskind, D. E., G. E. Nedoluha, C. E. Randall, and M. Fromm (2000), An assessment of Southern Hemisphere stratospheric NO_x enhancements due to transport from the upper atmosphere, *Geophysical Research Letters*, *27*(3), 329–332.

Siskind, D. E., S. D. Eckermann, L. Coy, J. P. McCormack, and C. E. Randall (2007), On recent interannual variability of the Arctic winter mesosphere: Implications for tracer descent, *Geophysical Research Letters*, *34*, L09806, doi:10.1029/2007GL029293.

Siskind, D. E., S. D. Eckermann, J. P. McCormack, L. Coy, K. W. Hoppel, and N. L. Baker (2010), Case studies of the mesospheric response to recent minor, major, and extended stratospheric warmings, *Journal of Geophysical Research*, *115*, D00N03, doi: 10.1029/2010JD014114.

Smith, A. K., R. R. Garcia, D. R. Marsh, and J. H. Richter (2011), WACCM simulations of the mean circulation and trace species transport in the winter mesosphere, *Journal of Geophysical Research*, *116*, D20115, doi:10.1029/2011JD016083.

Solomon, S., and P. J. Crutzen (1981), Analysis of the August 1972 solar proton event including chlorine chemistry, *Journal of Geophysical Research*, *86*(C2), 1140–1146.

Solomon, S., and R. R. Garcia (1983), On the distribution of nitrogen dioxide in the high-latitude stratosphere, *Journal of Geophysical Research*, *88*(C9), 5229–5239.

Solomon, S., and R. R. Garcia (1984), Transport of thermospheric NO to the upper stratosphere?, *Planetary and Space Science*, *32*(4), 399–409.

Solomon, S., P. J. Crutzen, and R. G. Roble (1982), Photochemical coupling between the thermosphere and the lower atmosphere 1. Odd nitrogen from 50 to 120 km, *Journal of Geophysical Research*, *87*(C9), 7206–7220.

Solomon, S., J. T. Kiehl, R. R. Garcia, and W. L. Grose (1986), Tracer transport by the diabatic circulation deduced from satellite observations, *Journal of the Atmospheric Sciences*, *43*(15), 1603–1617.

Solomon, S. C., C. A. Barth, and S. M. Bailey (1999), Auroral production of nitric oxide measured by the SNOE satellite, *Geophysical Research Letters*, *26*(9), 1259–1262, doi: 10.1029/1999GL900235.

Stiller, G. P., G. Mengistu Tsidu, T. von Clarmann, N. Glatthor, M. Höpfner, S. Kellmann, A. Linden, R. Ruhnke, and H. Fischer (2005), An enhanced HNO_3 second maximum in the Antarctic midwinter upper stratosphere 2003, *Journal of Geophysical Research*, *110*, D20303, doi:10.1029/2005JD006011.

Strobel, D. F. (1971), Diurnal variation of nitric oxide in the upper atmosphere, *Journal of Geophysical Research*, *76*(10), 2441–2452.

Strobel, D. F., D. M. Hunten, and M. B. McElroy (1970), Production and diffusion of nitric oxide, *Journal of Geophysical Research, Space Physics*, *75*(22), 4307–4321.

Swinbank, R., and A. O'Neill (1994), A stratosphere-troposphere data assimilation system, *Monthly Weather Review*, *122*, 686–702.

Thorne, R. M. (1980), The importance of energetic particle precipitation on the chemical composition of the middle atmosphere, *Pure and Applied Geophysics*, *118*, 128–151.

Thorne, R. M., B. Ni, X. Tao, R. B. Horne, and N. P. Meredith (2010), Scattering by chorus waves as the dominant cause of diffuse auroral precipitation, *Nature*, *467*, 943–6, doi:10.1038/nature09467.

Tsurutani, B. T., and W. D. Gonzalez (1987), The cause of high-intensity long-duration continuous *AE* activity (HILDCAAS): interplanetary Alfvén wave trains, *Planetary and Space Science*, *35*(4), 405–412.

Tsurutani, B. T., et al. (2006), Corotating interaction regions, *Journal of Geophysical Research*, *111*, doi:10.1029/2005JA011273.

Turunen, E., P. T. Verronen, A. Seppälä, C. J. Rodger, M. A. Clilverd, J. Tamminen, C.-F. Enell, and T. Ulich (2009), Impact of different energies of precipitating particles on NO_x generation in the middle and upper atmosphere during geomagnetic storms, *Journal of Atmospheric and Solar-Terrestrial Physics*, *71*, 1176–1189, doi:10.1016/j.jastp.2008.07.005.

Uppala, S. M., et al. (2005), The ERA-40 re-analysis, *Quarterly Journal of the Royal Meteorological Society*, *131*(612), 2961–3012, doi:10.1256/qj.04.176.

Varotsos, C. (2002), The Southern Hemisphere ozone hole split in 2002, *Environmental Science and Pollution Research*, *9*(6), 375–376.

Verronen, P. T., A. Seppälä, M. A. Clilverd, C. J. Rodger, E. Kyrölä, C.-F. Enell, T. Ulich, and E. Turunen (2005), Diurnal variation of ozone depletion during the October–November 2003 solar proton events, *Journal of Geophysical Research*, *110*, A09S32, doi:10.1029/2004JA010932.

Vitt, F. M., and C. H. Jackman (1996), A comparison of sources of odd nitrogen production from 1974 through 1993 in the Earth's middle atmosphere as calculated using a two-dimensional model, *Journal of Geophysical Research*, *101*(D3), 6729–6739.

Vogel, B., et al. (2008), Model simulations of stratospheric ozone loss caused by enhanced mesospheric NO_x during Arctic Winter 2003/2004, *Atmospheric Chemistry and Physics Discussions*, *8*, 5279–5293, doi:10.5194/acpd-8-4911-2008.

von Clarmann, T., et al. (2003), Retrieval of temperature and tangent altitude pointing from limb emission spectra recorded from space by the Michelson Interferometer for Passive Atmospheric Sounding (MIPAS), *Journal of Geophysical Research*, *108*(D23), 4736, doi:10.1029/2003JD003602.

von Clarmann, T., N. Glatthor, M. Höpfner, S. Kellmann, R. Ruhnke, G. P. Stiller, and H. Fischer (2005), Experimental evidence of perturbed odd hydrogen and chlorine chemistry after the October 2003 solar proton events, *Journal of Geophysical Research*, *110*, A09S45, doi:10.1029/2005JA011053.

Warneck, P. (1972), Cosmic radiation as a source of odd nitrogen in the stratosphere, *Journal of Geophysical Research*, *77*(33), 6589–6591.

Watson, R. T., M. A. Geller, R. S. Stolarski, and R. F. Hampson (1986), Present state of knowledge of the upper atmosphere: An assessment report, *NASA Ref. Publ*, *1162*.

Weeks, L. H., R. S. CuiKay, and J. R. Corbin (1972), Ozone measurements in the mesosphere during the solar proton event of 2 November 1969, *Journal of the Atmospheric Sciences*, *29*, 1138–1142.

Wetzel, G., et al. (2007), Validation of MIPAS-ENVISAT NO_2 operational data, *Atmospheric Chemistry and Physics*, *7*, 3261–3284.

Wofsy, S. C., and M. B. McElroy (1974), HO_x, NO_x, and ClO_x: Their role in atmospheric photochemistry, *Canadian Journal of Chemistry*, *52*, 1582–1591.

Yonker, J. D., and S. M. Bailey (2008), Transport properties of NO and N(^{4}S) in the thermosphere, *AGU Spring Meeting Abstracts*, p. B4.

Appendix A

List of Acronyms and Abbreviations

1-D	one-dimensional
2-D	two-dimensional
3-D	three-dimensional
ACE-FTS	Atmospheric Chemistry Experiment Fourier Transform Spectrometer
A_p	A_p planetary geomagnetic index
ATMOS	Atmospheric Trace Molecule Spectroscopy
CAM	Community Atmosphere Model
CESM	Community Earth System Model
CH_4	methane
CIR	corotating interaction region
CLaMS	Chemical Lagrangian Model of the Stratosphere
CLAES	Cryogenic Limb Array Etalon Spectrometer
CMAM	Canadian Middle Atmosphere Model
CME	coronal mass ejection

e*	energetic electrons or protons
ECHAM	European Centre Hamburg general circulation model
ECMWF	European Center for Medium range Weather Forecasting
EEP	energetic electron precipitation
ENVISAT	Environmental Satellite
EPP IE	Indirect Effect of energetic particle precipitation
EPP DE	Direct Effect of energetic particle precipitation
EPP-NO_x	NO_x created by energetic particle precipitation
ERA-40	ECMWF 40-year reanalysis
ES	elevated stratopause
ESA	European Space Agency
f10.7	10.7 cm solar radio flux
GCR	galactic cosmic ray
Gmol	gigamoles
GOMOS	Global Ozone Monitoring by Occultation of the Stars
GW	gravity wave
h	hours
HALOE	Halogen Occultation Experiment
HNO_3	nitric acid

HO_2	hydroperoxyl radical
HO_x	reactive odd hydrogen
HP	hemispheric power
hPa	hectopascals
IAA	Instituto de Astrofísica de Andalucía
IMK	Institute for Meteorology and Climate Research
ISAMS	Improved Stratospheric and Mesospheric Sounder
K	Kelvin
KASIMA	KArlsruhe SImulation Model of the middle Atmosphere
keV	kiloelectron-volts
km	kilometers
K_p	K_p planetary geomagnetic index
LIMS	Limb Infrared Monitor of the Stratosphere
log-p	log-pressure
MERRA	Modern Era Retrospective-analysis for Research and Applications
MESSy	Modular Earth Submodel System
MetO	Met Office
MeV	megaelectron-volts
MIPAS	Michelson Interferometer for Passive Atmospheric Sounding

MLT mesosphere-lower thermosphere

MLS Microwave Limb Sounder

MOZART Model for OZone And Related chemical Tracers

N_2 molecular nitrogen

N_2O nitrous oxide

N_2O_5 dinitrogen pentaoxide

NAM Northern Annular Mode

NCAR National Center for Atmospheric Research

NCEP National Centers for Environmental Prediction

NH northern hemisphere

nm nanometers

NO nitric oxide

NO_2 nitrogen dioxide

NO_3 nitrate radical

NOAA National Oceanic and Atmospheric Administration

NO_x reactive odd nitrogen (nitric oxide plus nitrogen dioxide, or NO + NO_2)

NO_y total odd nitrogen

O atomic oxygen

$O(^1D)$ excited state atomic oxygen

O_2	molecular oxygen
O_3	ozone
$O(^3P)$	ground state atomic oxygen
OH	hydroxyl radical
OSIRIS	Optical Spectrograph and InfraRed Imaging System
POAM	Polar Ozone and Aerosol Measurement
ppbv	parts per billion by volume
ppmv	parts per million by volume
REP	relativistic electron precipitation
s	seconds
SABER	Sounding of the Atmosphere using Broadband Emission Radiometry
SAGE	Stratospheric Aerosol and Gas Experiment
SEP	solar energetic particle
SH	southern hemisphere
SNOE	Student Nitric Oxide Explorer
SOCOL	SOlar Climate Ozone Links
SPE	solar proton event
SSW	sudden stratospheric warming
TEM	transformed Eulerian mean

TIME-GCM	thermosphere-ionosphere-mesosphere-electrodynamics general circulation model
TIROS	Television and Infrared Observation Satellite
UARS	Upper Atmosphere Research Satellite
$\overline{\mathbf{v}}^*$	meridional component of residual circulation
$\overline{\mathbf{w}}^*$	vertical component of residual circulation
WACCM	Whole Atmosphere Community Climate Model
WMO	World Meteorological Organization